The Physics and Chemistry of Transport in CdSe Quantum Dot Solids

by

Mirna Jarosz

B.S. Chemistry
University of Washington, Seattle, 1999

Submitted to the Department of Chemistry
in Partial Fulfillment of the Requirements for the Degree of

DOCTOR OF PHILOSOPHY

at the

MASSACHUSETTS INSTITUTE OF TECHNOLOGY

June 2004

Signature of Author⎯⎯⎯⎯⎯⎯⎯⎯⎯⎯⎯⎯⎯⎯⎯⎯⎯⎯⎯⎯⎯⎯⎯

Department of Chemistry
April 29, 2004

Certified by⎯⎯⎯⎯⎯⎯⎯⎯⎯⎯⎯⎯⎯⎯⎯⎯⎯⎯⎯⎯⎯⎯⎯⎯

Moungi G. Bawendi
Professor of Chemistry
Thesis Supervisor

Accepted by⎯⎯⎯⎯⎯⎯⎯⎯⎯⎯⎯⎯⎯⎯⎯⎯⎯⎯⎯⎯⎯⎯⎯⎯

Robert W. Field
Chairman, Department Committee on Graduate Students

This doctoral thesis has been examined by a committee of the Department of Chemistry as follows:

Professor Andrei Tokmakoff   ———————————————————

Chairman

Professor Moungi G. Bawendi   ———————————————————

Thesis Supervisor

Professor Marc Kastner   ———————————————————

The Physics and Chemistry of Transport in CdSe Quantum Dot Solids

by

Mirna Jarosz

ABSTRACT

Semiconductor quantum dots (QDs) have tunable opto-electronic properties and can be chemically synthesized and manipulated with ease, making them a promising novel material for many diverse applications. An understanding of the physics of charge transport in QDs is not only important for realizing QD based electronic devices, but it also provides crucial insight into the chemical and optical properties of QDs. This thesis highlights how photoconductivity measurements are valuable to advancing our understanding of QD physics because they are exquisitely sensitive to the optical, chemical, and electronic properties of QDs.

The work presented in this thesis emphasizes how the chemistry and physics of QD films are deeply entwined. Chapter 2 demonstrates that the photoconductivity and dark conductivity of CdSe QD films are enhanced following annealing at high temperatures. Chapter 3 illustrates that the purity of the QD capping reagent (tri-*n*-octylphosphine) and the methods used for film preparation can each affect the observed photocurrent by two to three orders of magnitude. In Chapter 4, the methods for CdSe film preparation developed in Chapter 3 are used to make films that exhibit photoconductivity properties consistent with having a low density of trapped charges, in contrast to previous studies. Chapter 5 also uses chemistry to bring CdSe QD films into a new regime of photoconductivity physics. Post-deposition chemical treatments that increase photocurrent by up to three to four orders of magnitude are presented. The voltage dependence of the photocurrent after treatment is consistent with having achieved unity exciton separation efficiency. Furthermore, by bringing CdSe QD films into this new regime of higher photoconductivity physics it is found that energetics prevent the facile injection of charges from gold electrodes into CdSe QDs, but there is no barrier to charge extraction.

Thesis Supervisor: Moungi G. Bawendi, Ph.D.
Title: Professor of Chemistry

For my husband and best friend Daniel

Table of Contents

List of Figures

14

Chapter 1

Introduction

1.1 "Every dot has its day"

Semiconductor quantum dots are a fascinating novel material of great scientific interest to a wide variety of disciplines. From the perspective of a physicist, a quantum dot (QD) is a semiconductor nanocrystal exhibiting quantum confinement in all three dimensions. That is, a nanocrystal with a diameter that is smaller than the bulk exciton Bohr radius. This thesis will focus exclusively on chemically synthesized colloidal quantum dots, rather than lithographically patterned[1] or self-assembled (Stranski-Krastanow)[2, 3] QDs. As will be discussed in more detail in Section 1.2, quantum confinement in QDs leads to the existence of discrete energy states for the confined electron and hole, as opposed to the energy bands present in the bulk semiconductor material. This fact has led to the description of QDs as "artificial atoms."[1] Furthermore, the spacing between the discrete energy states in a QD is a function of the QD's size. In addition to the electronic properties of a single QD being tunable, the coupling between QDs can also be tuned. Thus, QDs are technologically interesting as the building blocks for designer solids. They are also interesting to physicists as a model system to study the physics of confined charges, which is becoming increasingly vital to understand as transistors shrink to length scales below 100 nm.

Of course, confinement in QDs leads to interesting and size-tunable optical properties as well. Perhaps the most exploited optical property of QDs is their size-dependent band-edge fluorescence. One material alone, CdSe, can emit fluorescence that spans the entire visible range, from blue to red. Furthermore, this fluorescence is very narrow (FWHM ≤ 40nm) and very bright (30-50% quantum yield after overcoating with ZnS).[4] There has also been significant interest in the optical properties of single QDs, which has led to the discovery that QDs have intermittent fluorescence (i.e., they "blink").[5] This blinking behavior is thought to be due to QDs becoming charged, which turns off the fluorescence due to a three-body Auger recombination process. Single QD studies have also uncovered that the quantum yield and fluorescence lifetime of a single QD fluctuate over time (in correlation with each other).[6]

Perhaps on the other end of the scientific spectrum from physicists and spectroscopists, biologists are interested in QDs as fluorescent tags due to their high quantum yield, tunable and narrow fluorescence, customizable functionality, and a high resistance to photobleaching and photochemical degredation.[7] The fluorescence of QDs can last orders of magnitude longer than that of conventional organic dyes used as fluorescent labels. Some applications of QDs to biological problems include sentinel lymph node mapping[8,9] and in vivo imaging.[10-12]

QDs, or more generally nanocrystals, are also interesting to chemists as an intriguing system in which to study crystal nucleation and growth. It has proven to be possible to not only control nanocrystal size, but also shape and crystal structure.[13-18] QDs can be overcoated with another semiconductor either to further confine the exciton[4] or to create a type-II material with a new band gap.[9] There has also been significant work

on the organic shell capping the inorganic QD, customizing it for desired solubility and/or functionality.[11, 19, 20]

In addition to being of scientific interest, QDs offer promise as a novel material for many practical applications. Colloidal QDs are particularly appealing for such applications as they are inexpensive and easy to synthesize, manipulate, and incorporate into device structures. Many of these applications take advantage of the tunable fluorescence emission of QD materials. For example, room temperature, optically-pumped CdSe QD lasing has been demonstrated in a variety of visible colors.[21, 22] There have also been numerous successful attempts at making light emitting diodes (LEDs) from QDs[23-26] with external quantum efficiencies as high as 1.1% reported.[23] Other applications take advantage of the charge-transport properties of QDs, in conjunction with their absorption abilities. For example, it should be possible to extend the photoconductive properties[27-31] of QDs to the development of a color-sensitive photodetector. In addition, it has been demonstrated that CdSe QDs can be successfully incorporated into photovoltaic devices (solar cells).[32, 33] This has the potential to have an enormous impact if photovoltaic efficiencies are increased, as the production of a QD-based device is far less expensive than the production of a devices using high quality traditional semiconducting materials.

And last, but not least, one cannot forget what QDs mean to a physical chemist that has fallen in love with her undergraduate quantum mechanics classes, and is searching for a way to actually apply this love to something useful. I was fascinated with QDs since first learning about them as an undergraduate. To me, QDs are quantum mechanics in action: a visible example of a particle-in-a-box.

1.2 Quantum Confinement

1.2.1 The case of CdSe

The electronic and excitonic structure of a QD can be understood from the perspective of what happens when a cluster of atoms grows, or by considering what happens when a bulk semiconductor shrinks. Quantum confinement will be discussed briefly and qualitatively here; more thorough and quantitative treatments can be found in the literature.[34-36] It is instructive to begin with a brief description of the physical character of bulk semiconductors. To facilitate the following discussions, the case of CdSe will be addressed, as this is the prototype QD material and the type of QD studied in this thesis.

CdSe falls into a subcategory of semiconductors referred to as the II-VIs, due to the positions of Cd and Se in the periodic table. The usual crystal structure of bulk CdSe is hexagonal, and it is a direct band gap semiconductor.[37] Bulk CdSe has a broad and generally featureless absorption spectrum starting at ~716 nm, with an exciton Bohr radius of ~6 nm (meaning that a photo-generated electron-hole pair delocalizes over ~12 nm).[38]

The origin of the valence band is the 4p states of selenium, and the origin of the conduction band is the 5s states of cadmium. The conduction band has quantum number $J_z = 1/2$. The valence band has three sub-bands, one of which has quantum number $J_z = 3/2$ (this is the highest energy band), and two of which have quantum number $J_z = 1/2$.
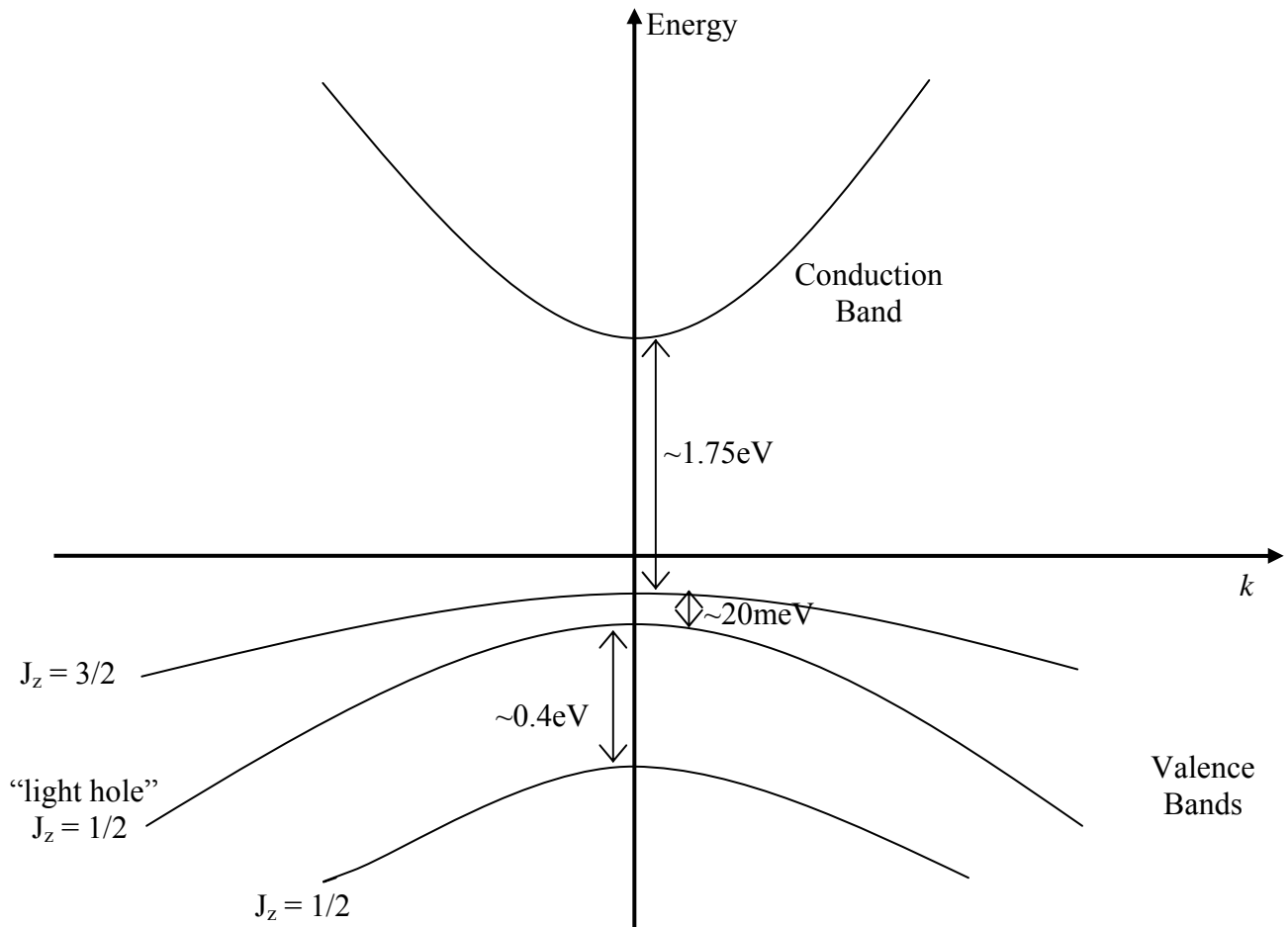
Figure 1.1: Schematic of the band structure of bulk CdSe.

The band gap (between the highest energy valence sub-band and the conduction band) is ~1.75 eV at room temperature (~ 700 nm). The effective mass of the conduction band is only ~ 0.1, while the highest energy valence band has an effective mass of nearly 1 (thus it is said that CdSe has a "heavy hole"). Below the energy of this valence band, a light hole band also exists.[37] Figure 1.1 summarizes the band structure of bulk CdSe, including relevant energies.

An exciton generated in CdSe will begin to be affected by quantum confinement as the material's dimensions shrink below the bulk exciton Bohr radius (~ 6 nm). Thus, CdSe nanocrystals with a radius of less than ~ 6 nm have optical and electronic properties that differ quite dramatically from those of bulk CdSe. The most obvious effect of this quantum confinement is the blue-shift of the first (reddest) absorption feature with decreasing QD size. This effect is illustrated in Figure 1.2 for the case of CdSe.

The blue-shift of the CdSe QD "band gap" energy with decreasing size can be related (very approximately) to the system of a particle in a spherical box. In this case, the energy of the particle, E, is proportional to $1/a^2$, where a is the radius of the box. Clearly, as the box shrinks the energy of the particle increases ("blue-shifts"). The model of a particle in a spherical box has additional similarities to a QD. The energy states of the particle are quantized due to the particle's confinement; this is also true for the electronic states of a QD. Unlike the bulk material, CdSe QDs do not actually have energy bands, but rather they have quantized electron and hole states. In this respect, they are very much like "artificial atoms."[1] This means that not only are the absorption spectra of QDs blue-shifted from the bulk, but they also are no longer featureless. Both effects, blue-shifting as well as energy quantization, can be seen in Figure 1.3. The
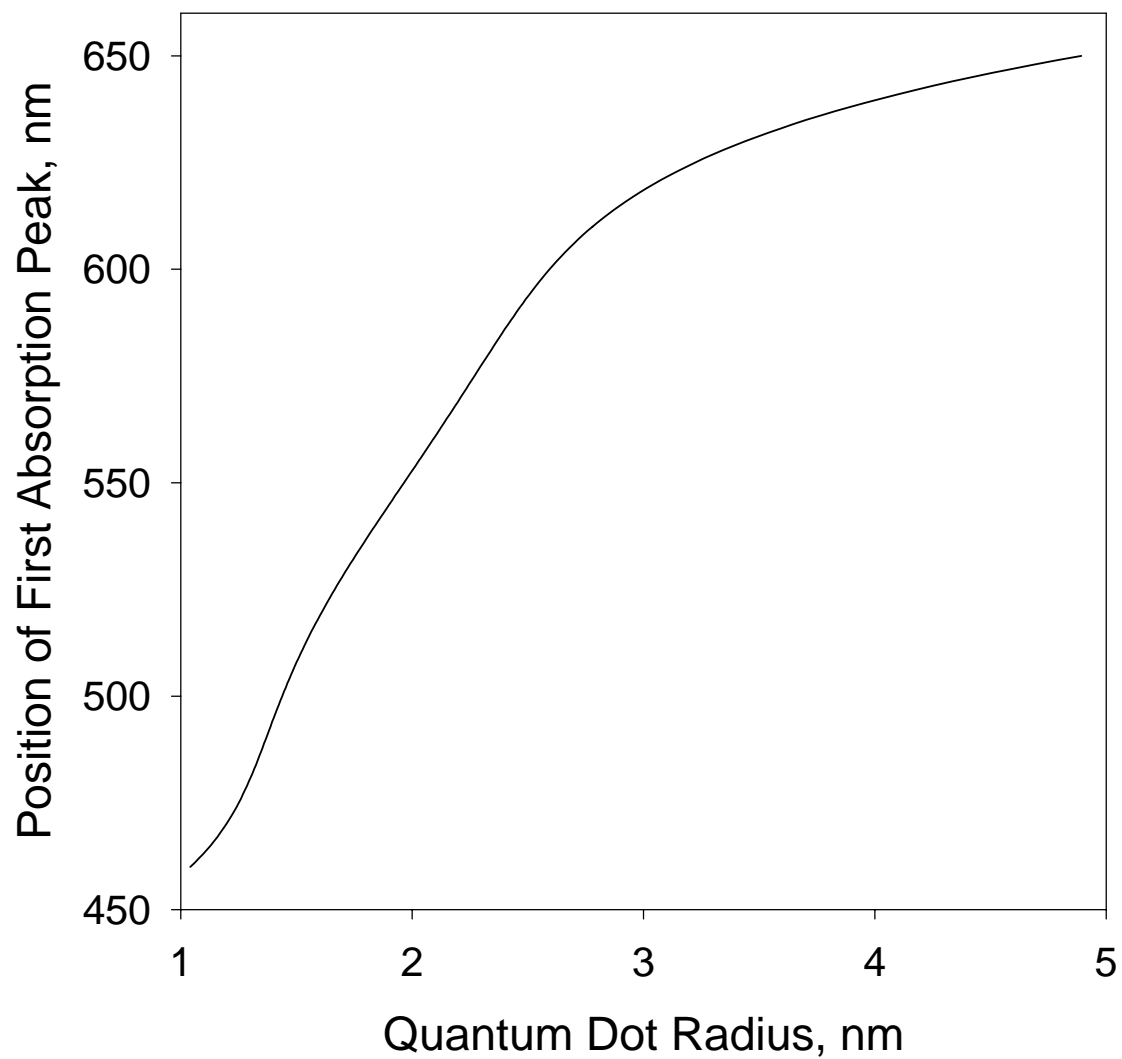
Figure 1.2: The effect of size on the position of the first absorption peak of CdSe quantum dots. The curve is a fifth order polynomial fit to sizing data, the coefficients of which can be found in M. K. Kuno, "Band Edge Spectroscopy of CdSe Quantum Dots," (Massachusetts Institute of Technology, Cambridge, 1998).
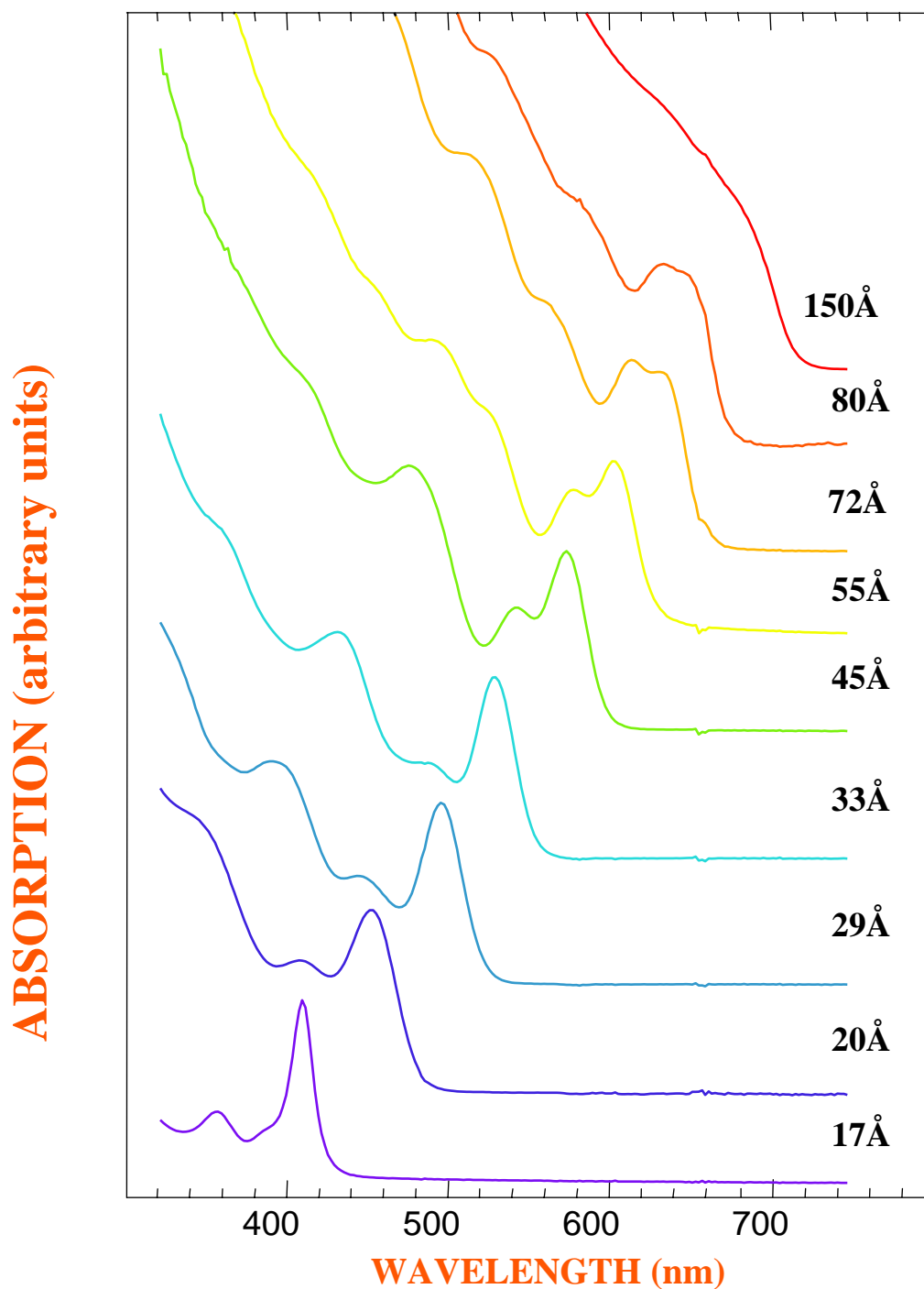
Figure 1.3: Size dependence of the absorption spectrum of CdSe quantum dots. The numbers on the right of each spectrum represent the quantum dot diameter. Figure from C. B. Murray, "Synthesis and Characterization of II-VI Quantum Dots and Their Assembly into 3D Quantum Dot Superlattices," (Massachusetts Institute of Technology, Cambridge, 1995).

absorption spectrum of the quantum dots with a 15 nm diameter in Figure 1.3 appears quite similar to bulk CdSe, being quite broad and featureless, as it experiences very little additional confinement from the bulk. Sharp transitions as well as a significant blue-shift are quite evident in the absorption spectra for the QDs with diameters of less than 12 nm (the bulk exciton Bohr diameter).

While of course energy bands no longer exist in the electronic structure of QDs, some trends from the band structure of the bulk material (Figure 1.1) are preserved. The conduction states still originate from the cadmium 5s orbitals, and the valence states still originate from the selenium 4p states. Figure 1.4(a) shows the general electronic structure of a CdSe quantum dot, ignoring the effects that lead to the excitonic and electronic fine structure (as was done in Figure 1.1). Figure 1.4(b) shows the absorption spectrum of a sample of quantum dots, and indicates which transitions in Figure 1.4(a) give rise to the absorption features.

There are additional aspects of the electronic structure of CdSe QDs that are relevant to the work discussed in this thesis. As much as one can refer to effective mass when energy bands are no longer present, the highest energy valence states are still said to have a large effective mass, whereas the lowest energy conduction states are still said to have a small effective mass. The manifestation of this is that when an exciton is created, the hole states have a much higher density than the electron states. In fact, the $1S_e$ and $1P_e$ states of a CdSe QD (the two lowest energy electron states) are separated by $\sim 0.3 - 0.5$ eV (with the separation being larger for smaller dots), making this intraband transition observable in the infrared.[39-51] This property is very material dependent; for
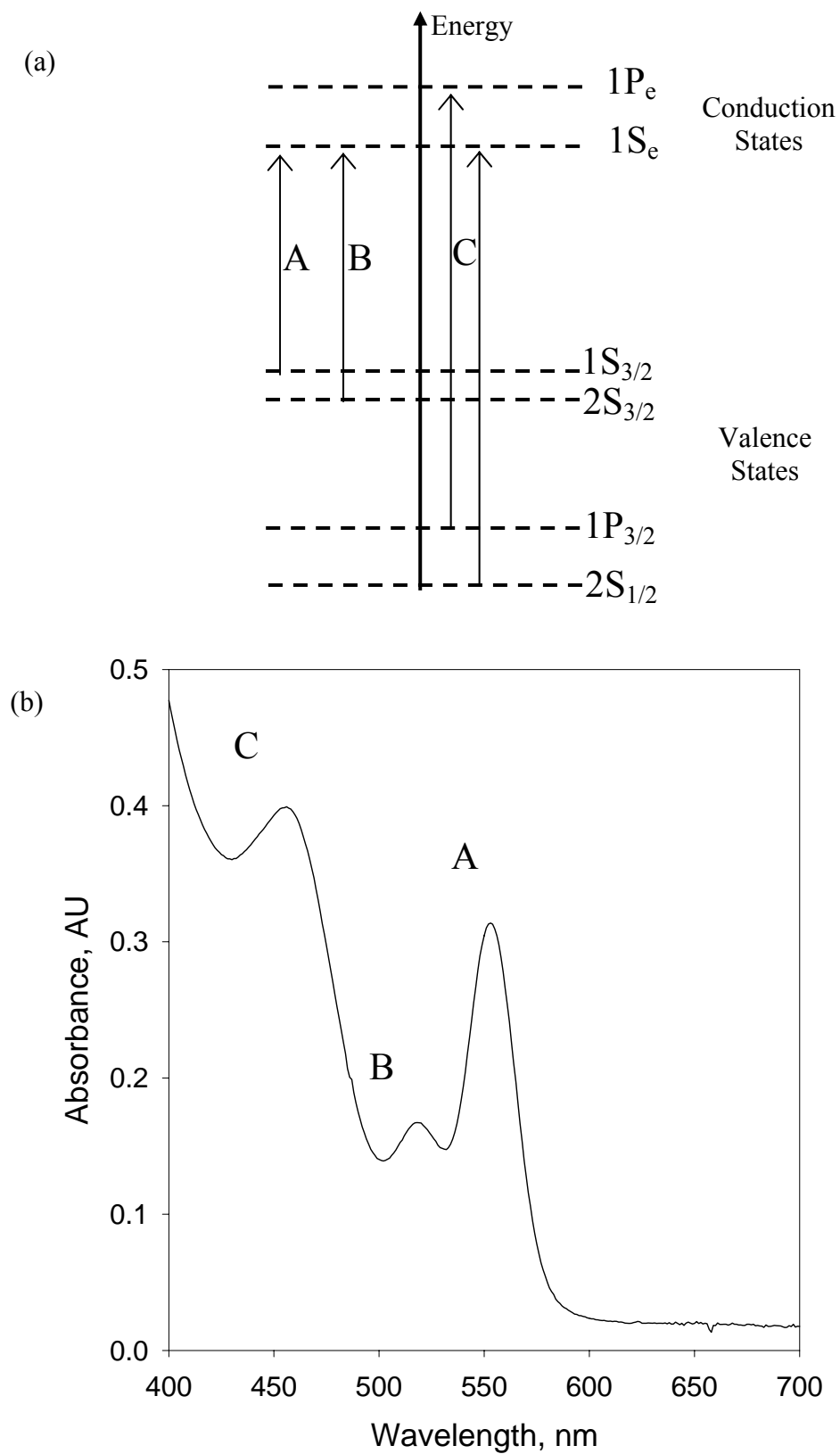
Figure 1.4: (a) Schematic approximating the energy levels in a CdSe quantum dot. The fine structure is not taken into account. Not drawn to scale. (b) Absorption spectrum of CdSe quantum dots; A, B, and C correspond to the transitions indicated in (a).

instance, PbSe has conduction states and valence states with approximately the same

effective mass and density of states. Therefore, intraband transitions for both an electron

in the lowest conduction state as well a hole in the highest valence state are observable at

very similar energies in the infrared.[52, 53]

1.2.2 Electronic consequences of quantum confinement

In addition to affecting the electronic energy states of a QD, quantum

confinement has additional consequences with regard to QD charging and charge

transport. Some relevant electronic properties that are dependent of QD size are self-

charging energy,[36] Coulomb charging energy, and exciton ionization energy. The self-

charging energy is the energy required to add a single charge to a neutral QD, whereas

the Coulomb charging energy is the energy required to add a single charge to a QD that is

already charged (with a charge of the same sign).

The self- and Coulomb charging energies increase with decreasing QD size for

the same reason that the QD absorption spectrum blue-shifts: confining a charge

increases its energy (just as is seen for the particle in a spherical box model). The

Coulomb charging energy for CdSe QDs smaller than ~10 nm in diameter is > 100meV.[54]

Since this is significantly higher than the available thermal energy at room temperature, a

sufficiently high applied electric field is necessary before charges can be added to a QD.

Similarly, exciton ionization also requires a sufficiently high applied electric field, as the

energy cost of ionizing an exciton, estimated to be ~100 – 600 meV,[28] is significantly

higher than the available thermal energy as well. This will be further discussed in

Section 1.6, in the context of a background on photoconductivity in CdSe QD solids.

1.3 Synthesis of Quantum Dots

1.3.1 Synthesis using dimethyl cadmium

Until recently, the synthesis of CdSe QDs was usually based on the methods developed by Murray *et al*[55] (sometimes with the modifications made by Bowen Katari *et al*[56]). The Murray *et al*[55] synthesis is used for the earlier work in this thesis. According to this method, tri-*n*-octylphosphine oxide (TOPO) is prepared by degassing under vacuum, followed by heating to 350 ^{o}C under an inert atmosphere. A precursor solution of dimethyl cadmium, tri-*n*-octylphosphine (TOP) and TOP selenide (TOPSe) is rapidly injected into the hot TOPO. The injection results in the nucleation of very small (2 - 3 nm in diameter) CdSe QDs. These can be isolated by immediately cooling the reaction to room temperature. Larger sizes are achieved by continuing to grow the initially created small QDs by heating the reaction mixture at ~ 280 – 295 ^{o}C.

This synthesis results in highly crystalline inorganic CdSe nanocrystals capped with TOP and TOPO. It now seems clear that there are additional chemical species that are necessary to control the QD growth, as this synthesis will not work if 100% pure TOPO is used. When this synthesis has been used for the work in this thesis, 90% TOPO was necessary (although, not all bottles of 90% TOPO are alike, obviously; the batches must be tested first). Figure 1.5(a) shows the reaction setup, and Figure 1.5(b) shows a high resolution transmission electron microscopy (TEM) image of a single CdSe nanocrystal.
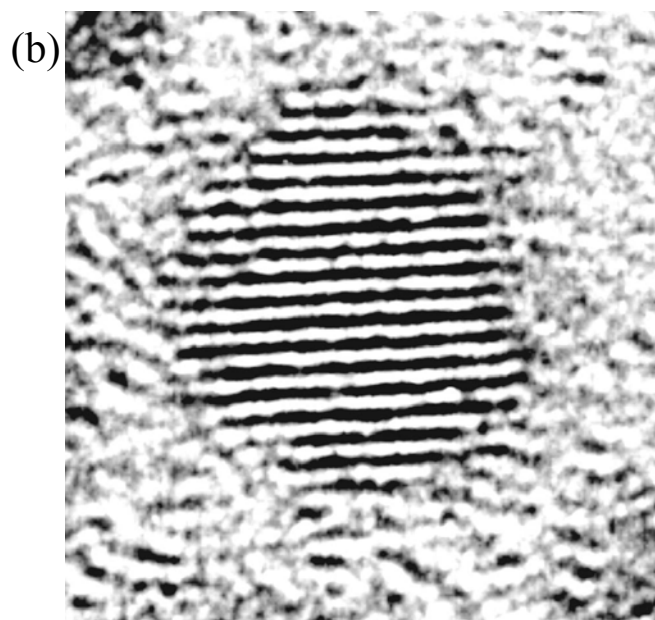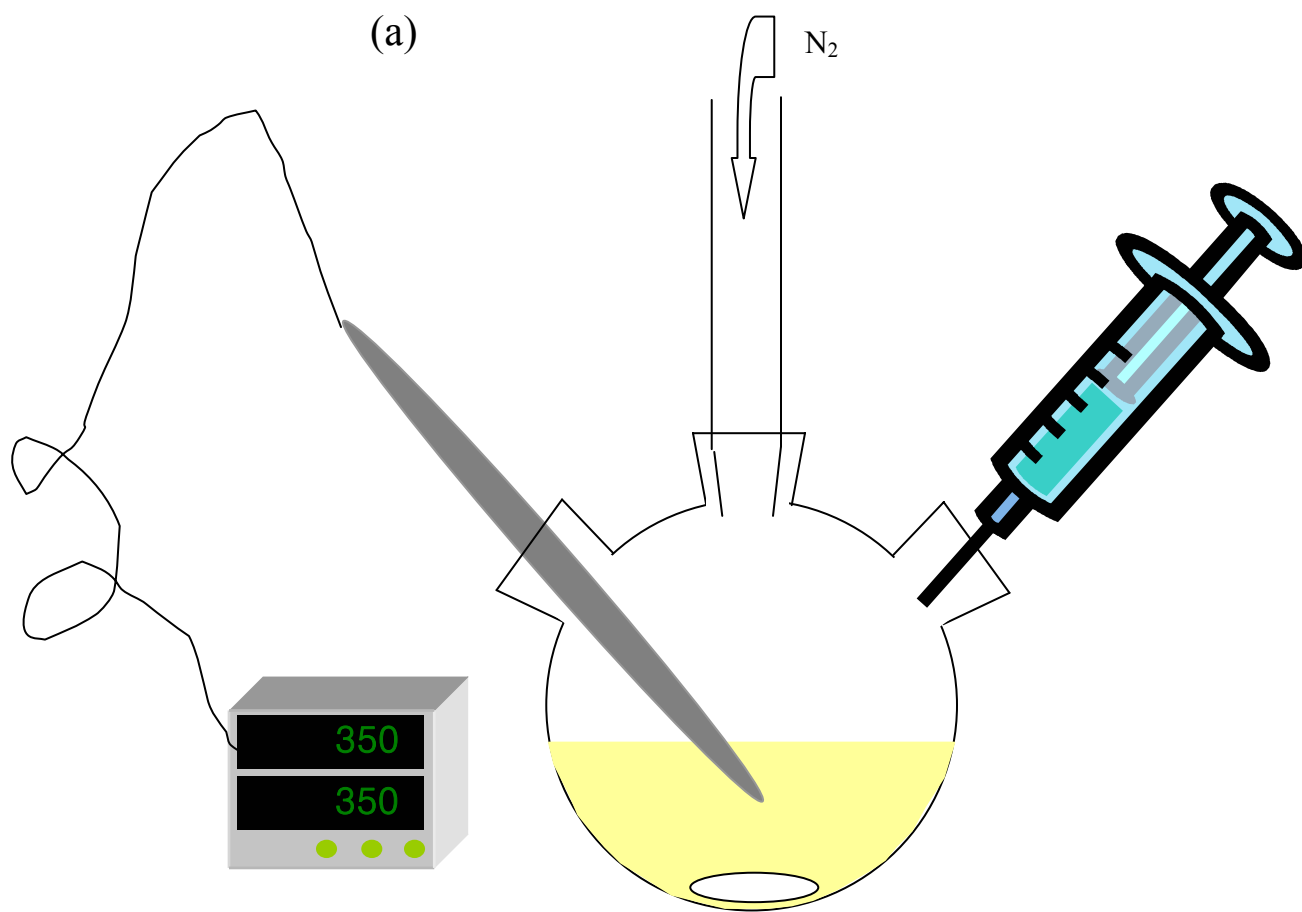
Figure 1.5: (a) Setup for quantum dot synthesis. (b) High resolution TEM of a single CdSe quantum dot. The lattice fringes are indicative of the highly crystalline nature of the quantum dot. Microscopy by F. Mikulec.

1.3.2 Synthesis using cadmium salts

Due to the pyrophoric and highly toxic nature of dimethylcadmium, many

researchers studying cadmium-based QDs welcomed the new synthetic methods that

replace dimethylcadmium with cadmium salts.[57-63] These new methods also allow the

use of higher purity starting materials, as additional materials are added to take the place

of the unknown impurities that made the original dimethylcadmium-based prep work.

The first cadmium salt based method used for the work in this thesis is based on

cadmium 2,4-pentanedionate (also known as cadmium acetylacetonate, or $Cd(acac)_2$).[57]

According to this method, a precursor mixture is prepared by degassing 1,2-

hexadecanediol (HDDO), TOP, and $Cd(acac)_2$ under vacuum at 100 ^{o}C for one hour.

After this mixture has cooled to room temperature under an inert atmosphere, 1.5 M

TOPSe is added. Meanwhile, a solvent mixture of TOP, TOPO (99%, for the work in

this thesis), and 1-hexadecylamine (HDA) is degassed under vacuum at 140 ^{o}C for two

hours, and then heated under an inert atmosphere to 360 ^{o}C. At this point, the heating

mantle and glass wool are removed, and the precursor mixture is rapidly injected. The

reaction mixture is allowed to cool to ~ 80 ^{o}C, at which point hexane is added to prevent

the sample from solidifying once it cools to room temperature. Figure 1.6 shows a high

resolution TEM image of a single CdSe QD prepared according to these methods, which

confirms that these QDs are still highly crystalline.

Unlike the dimethylcadmium-based method, the desired size of QDs is

immediately achieved, so there is no need for continued growth of the sample via heating

of the reaction mixture. The size can be tuned by using more (for larger QDs) or less (for

smaller QDs) $Cd(acac)_2$, and by adjusting the remaining ingredients accordingly. The
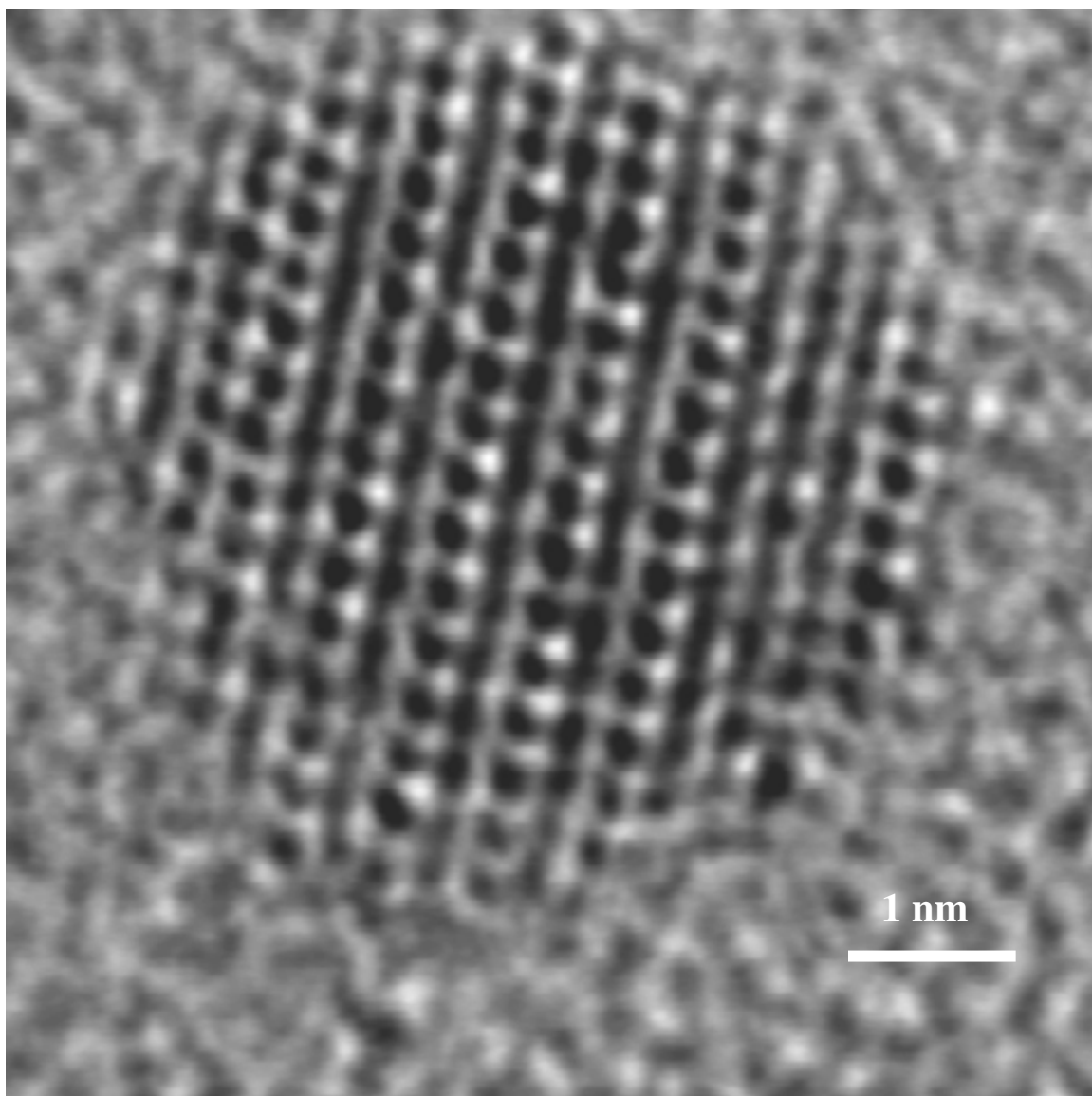
Figure 1.6: High resolution TEM image of a single CdSe quantum dot prepared using Cd(acac)$_2$. Microscopy by M. Jarosz, with the assistance of M. Frongillo.

molar ratios for Cd(acac)$_2$: HDDO : Se are 1 : 2.2 : 3. Generally, a range of 0.25 – 3 mmol of Cd(acac)$_2$ is used to cover the visible spectrum. The solvent remains the same regardless of the amount of Cd(acac)$_2$ used, and the TOP in the precursor mixture is adjusted so that the total injection volume is 10 mL. While 90% TOPO can still be used for these methods, the purity of the TOPO can have a drastic effect on the resulting size of the QDs. Generally, purer TOPO results in larger QDs.

The "second generation" cadmium salt based method used for this work is based on cadmium hydroxide, Cd(OH)$_2$.[57, 58] Unlike the previous two methods discussed, this method uses TOP but no TOPO. An advantage of this modification is that the growth solution is liquid at room temperature; this has proven to be extremely important for the automation of QD synthesis using a microcapillary reactor.[58] It is also faster (as it does not require degassing TOPO for two hours) and consistently produces samples of QDs that are very bright and that have very narrow size distributions.

For the Cd(OH)$_2$ based synthesis, a precursor solution of Cd(OH)$_2$, TOP, and cis-9-octadecanoic acid (oleic acid) is prepared by degassing under vacuum at 100 $^{\circ}$C for one hour. It is suspected that this process creates cadmium oleate, resulting in water being removed during the degassing. After degassing, this solution is put under an inert atmosphere and cooled to room temperature, at which point 1.5 M TOPSe is added. The solvent mixture consists of TOP, dioctyl ether, and oleylamine (all stored in a nitrogen glovebox so that no degassing is necessary). After the solvent is heated under an inert atmosphere to 330 $^{\circ}$C, the heating mantle and glass wool are removed and the precursor solution is rapidly injected. As for the Cd(acac)$_2$-based method, the reaction mixture is cooled to room temperature after the injection since the desired size of QDs is achieved

without further heating. In addition to controlling the final QD size with the amount of

Cd(OH)$_2$ that is used, it is also possible to control the size via the injection temperature

and/or the Se : Cd ratio. In general, a higher Se : Cd ratio or a lower temperature results

in smaller QDs.[58] Injection temperatures above 330 ^{o}C can be used if squalane is

substituted for dioctyl ether in the solvent mixture.

1.3.3 Post-synthetic modifications

QDs synthesized according to the above methods can be modified to increase

quantum yield or to optimize the organic caps. It may be desirable to have QDs capped

with something other than TOP/TOPO in order to change the length of the cap, to have

water-soluble QDs, or to have QDs that can be attached to another material (biological

molecules or magnetic particles, for example) through the organic caps.

The quantum yield of QDs synthesized via the dimethylcadmium-based method

can be increased by treating the QDs with amines.[64, 65] It has been pointed out[65] that

amines increase QD quantum yield for two reasons: the first reason is that, due to the

steric hindrance resulting from having three alkyl groups, TOP/TOPO caps leave many

surface sites unpassivated. Thus, less sterically hindered primary amines are able to

increase the level of passivation of QD surface sites. The second reason is that amines

have a mild etching effect, so that fresh surface sites are exposed and more easily

passivated. It might also be possible that defect-sites, having a higher energy, are etched

faster than non-defect sites.

The most common method to increase the quantum yield of CdSe QDs (no matter

the method of synthesis) is to overcoat the QDs with a higher band gap semiconductor

such as ZnS.[4, 66] The higher band gap shell further confines the exciton, and the probability of finding the exciton on the surface (considered to be the likely location for nonradiative recombination processes) is reduced. Because introducing an additional tunnel barrier is not particularly desirable for photoconductivity processes, no measurements of overcoated samples are presented in this thesis.

1.4 Quantum Dot Films

The basic methods of preparation for the QD films used in this thesis are based on previous work.[27, 55, 67-70] The first and arguably most critical step towards making good QD films is to isolate the QDs from all other chemicals that are found in the growth solution. For the dimethylcadmium-based synthesis, this can be achieved through three size-selective precipitations based on a solvent and non-solvent procedure.[55] Methanol is used as the non-solvent and hexane and butanol are used as the solvents. In addition to narrowing the size distribution of the QD sample (because the larger QDs will precipitate more readily), this procedure also separates the QDs from excess TOP and TOPO. This occurs because TOP and TOPO are more soluble in methanol when not attached to QDs than the QDs capped with TOP and TOPO (because essentially only the octane groups are exposed to the solution, making the QDs look very "fatty"). This procedure must be modified for use with QDs synthesized using $Cd(acac)_2$ or $Cd(OH)_2$, as will be described in Chapter 3 of this thesis.

Once a powder of clean QDs is obtained, close-packed films are made by depositing from a concentrated solution of QDs in 9:1 hexane:octane. The solvent mixture is chosen in order to optimize the drying time and degree of ordering of the film.

(a)
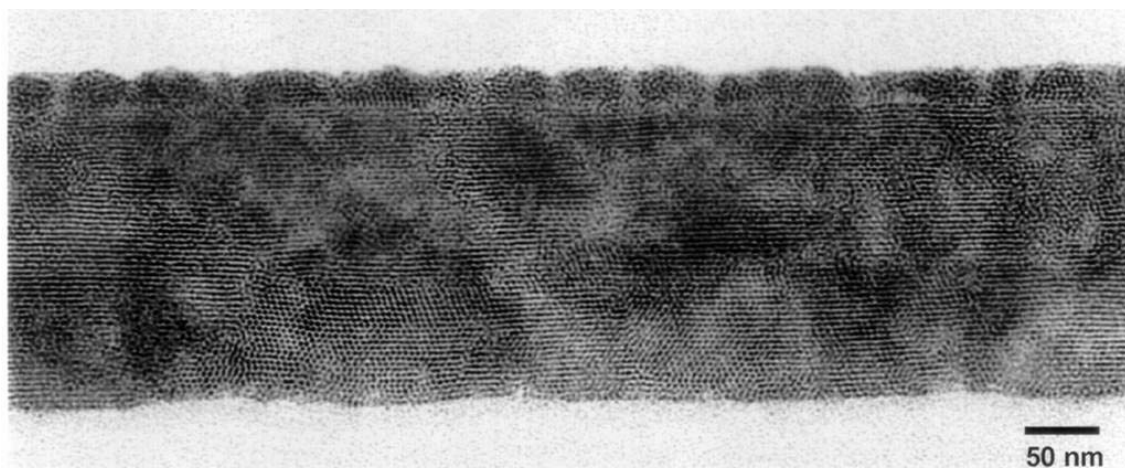
(b)
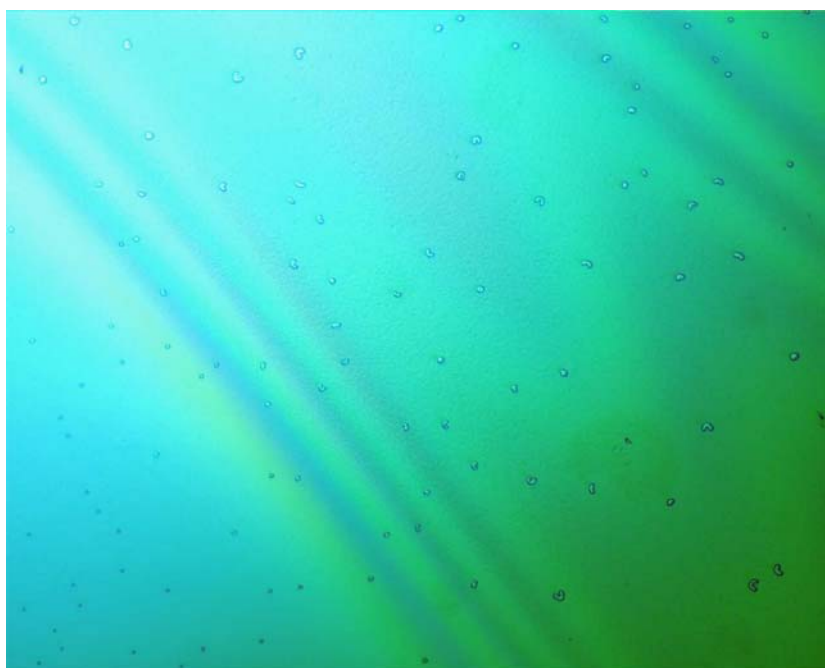
Figure 1.7: (a) Cross-sectional TEM image of a film of close-packed CdSe QDs. Sample made by C. A. Leatherdale, and microscopy by L. Radilowski. (b) Optical microscope image of a film of close-packed CdSe QDs, indicating that the films are quite smooth and optically clear.

(a)

10 nm

(b)

10 nm
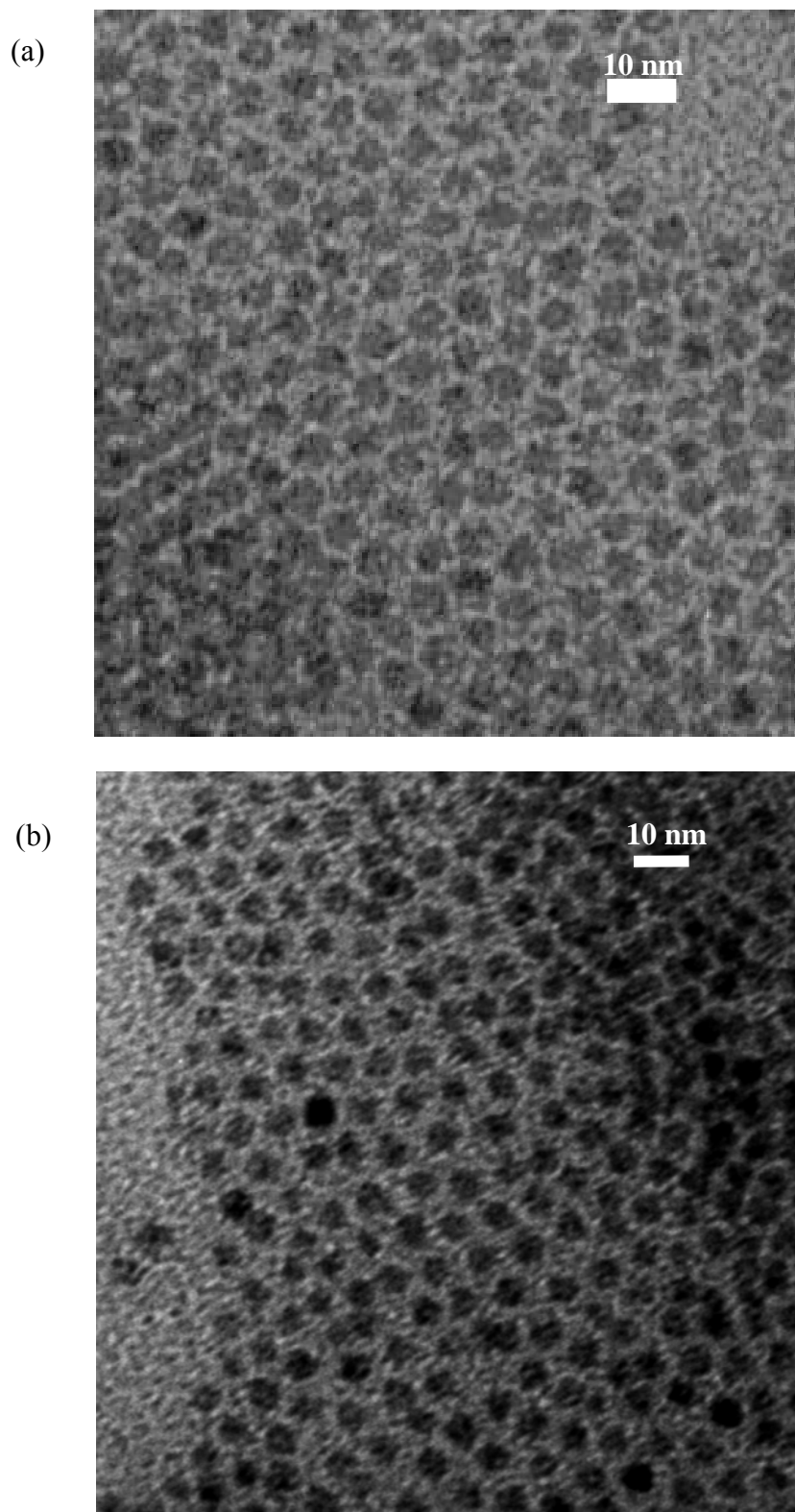
Figure 1.8: TEM images of close-packed films of CdSe QDs made via the dimethylcadmium synthesis (a) and the Cd(acac)$_2$ synthesis (b).

Figure 1.7(a) shows a cross-sectional TEM image of a close-packed film of CdSe QDs. While polycrystalline as well as amorphous regions are evident in the film, it is also clear that there is not a wide variation in QD interdot spacing. Figure 1.7(b) shows an optical microscope image of a close-packed CdSe QD film, illustrating that the films are smooth and optically clear. Figure 1.8 shows TEM images of close-packed CdSe QD films, deposited from more dilute solutions so that mono- and bi-layers can be seen.

1.5 Dark Conductivity in CdSe QD Films

There have been a number of recent studies of dark conductivity in CdSe QDs.[31, 48, 71-74] Those that are most relevant as a back-drop to the work in this thesis are briefly described below.

1.5.1 Summary of dark conductivity results of Ginger and Greenham[74]

Ginger and Greenham present conductivity studies of CdSe QDs in a sandwich geometry. The device studied consists of an indium tin oxide (ITO) bottom electrode, a spin-coated film of CdSe QDs about 200 nm thick, and a top metal electrode. When the top electrode is aluminum or calcium, significant dark conductivity is observed, with higher currents when the ITO electrode is at positive bias. When the top electrode is gold, far less current is passed through the device, and it is not found to have significant rectification. Due to the differences observed with different top electrodes, it is suggested that the conductivity is electron dominated, and that electron injection is difficult from either ITO or gold. This is shown to be consistent with the predicted positions of the CdSe QD conduction and valence states with respect to vacuum, as the

work functions for aluminum and calcium are above the QD conduction state and the

work functions of ITO and gold are just below it (Table 1.1).

Table 1.1: Comparison of the work functions of four metals to the conduction and valence state energies (below vacuum level) of a 4 nm CdSe QD, from Reference [74].

	Work Function, eV	Conduction State, eV	Valence State, eV
4 nm CdSe QD	-	4.6	6.7
Calcium	2.87	-	-
Aluminum	4.28	-	-
ITO	4.75	-	-
Gold	5.1	-	-

While the observation of a monotonically decreasing dark current after

application of a voltage step is consistent with the work of Morgan et al.[71], the functional

form found by Ginger and Greenham is a stretched-exponential rather than a power law

decay. Another discrepancy is that while Morgan et al. find that the current decays more

rapidly with increasing temperature, Ginger and Greenham find their observations to be

consistent with thermally activated hopping above 180 K.

Ginger and Greenham propose a model for these observations that is based on

slow filling of deep traps by electrons, resulting in space-charge limited current. In

addition, they estimate the electron mobility, μ_n, to be $\sim 10^{-4} - 10^{-6}$ cm^2 V^{-1} s^{-1}, and the

hole mobility, μ_p, to be $< 10^{-12}$ cm^2 V^{-1} s^{-1}.

1.5.2 Summary of dark conductivity results of Morgan et al.[71]

The extensive study of Morgan et al.[71] provides the most relevant back-drop for

the work that will be discussed in this thesis, as the silicon devices and QD films are

prepared according to the same methods used in this thesis. It is particularly significant

that Morgan *et al.* study a lateral geometry (as is done in this thesis), as opposed to the

sandwich geometry studied by Ginger and Greenham. As well as resulting in slightly

different physics, the sandwich geometry has two additional significant differences. First,

some portion of the QD film is likely damaged following the deposition of the top

electrode. Second, there is no gate electrode in the sandwich geometry.

The devices studied by Morgan *et al.* consist of an inverted field effect transistor

(FET) structure, with a back gate of degeneratively doped silicon, ~350 nm of thermally

grown oxide, and gold H-bar electrodes. A QD film of thickness 100 – 900 nm is

deposited over the entire sample, according to the methods described in Section 1.4

above (for CdSe QDs prepared using dimethylcadmium). At temperatures below 200 K,

the CdSe QD films studied by Morgan *et al.* are found to be highly resistive, with

resistivity greater than about 10^{14} ohms-cm. Measurements on gated silicon devices with

gold electrodes suggest that hole injection is not observable, and that electron injection is

observable only at very high negative voltages (i.e., greater than ~ -100 V on a 1 μm gap).

It is found that the films become more resistive with time, resulting in a power law decay

of the current after the application of a voltage step. The power law exponent is found to

be on the order of -0.1 to -1. Even when the film is measured for as long as 2×10^4

seconds, no steady state current is observed. Measurements on gaps of varying widths

confirm that the current transients scale at all times with applied field.

Temperature dependent measurements indicate that there is little change in the

current amplitude or the power law decay exponent from 6 K to ~ 150 K. From ~ 150 K

to ~ 220 K, the current amplitude increases slightly and the power law exponent becomes

more negative (i.e., the current transient decay is steeper). Above 220 K, the

observations are attributed to an artifact resulting from the increase in leakage current

with temperature.

It is concluded that the observed current is too large to be due only to the charging

of the film, and thus it must be due to current that passes through the film between the

two electrodes. However, the decay of the current is attributed to charge storage within

the film, which results in the film becoming more resistive with time. Because the

current still scales with field, it is concluded that the charge stored in the film cannot

extend more than 100 nm from the injecting contact. It is pointed out that this may

account for the different observations of Ginger and Greenham, as a charged region of

100 nm would extend across half of the sample length for the Ginger and Greenham

device structure. Morgan *et al*. explain the power law behavior of the decaying current

transients by proposing that the space charge near the injection contact is a Coulomb

glass. As the Coulomb glass relaxes in time, the escape of electrons from the space

charge region slows down. Larger power law exponents of the current transients are

attributed to a faster relaxation of the Coulomb glass in the space charge region. Thus,

samples with increased QD coupling (for example, with a smaller interdot spacing)

exhibit steeper power law decays because of faster Coulomb glass relaxation.

1.6 Photoconductivity in CdSe QD Films

Previous work by C. R. Kagan[27, 28] and C. A. Leatherdale[28, 54] as summarized in

Leatherdale *et al*.[28] establishes the background necessary to understand photoconductivity

processes in close-packed films of CdSe QDs. The samples in these studies consist of CdSe QDs synthesized using dimethylcadmium, and QD films prepared according to previously established methods,[27, 55, 67-70] as described in Section 1.4 above. The films are deposited on silicon substrates identical to those used by Morgan *et al.*[71]

A comparison of the spectral dependence of the photocurrent response of CdSe QD films reported in Leatherdale *et al* (see Figure 1.9) indicates that there is no photocurrent response at excitation energies below the band gap energy. The photocurrent spectral response also mirrors the other features that are present in the QD absorption spectrum. This is taken as clear evidence that the photogenerated carriers contributing to photoconductivity stem from the confined electron-hole pairs generated inside individual QDs. The deviation of the photocurrent data from the absorption spectrum at higher energies is attributed to the increase in the nonradiative recombination rate at higher energy excitation, which leads to a lower photocurrent efficiency per absorbed photon.

Leatherdale *et al* present a model for the photoconductivity of CdSe QD films based on ionization of quantum confined excitons. As the maximum potential drop between two neighboring QDs is far less than the potential confining an electron to a QD, the electron-hole pair is separated via a tunneling process. The highly field dependent behavior of the photocurrent is thus attributed to the highly field dependent exciton ionization efficiency. The rate of ionization of the exciton becomes more competitive with both the radiative and nonradiative recombination rates of the exciton as the field is increased. Leatherdale *et al* show that the field dependence of the photocurrent can be fit to a tunneling model,
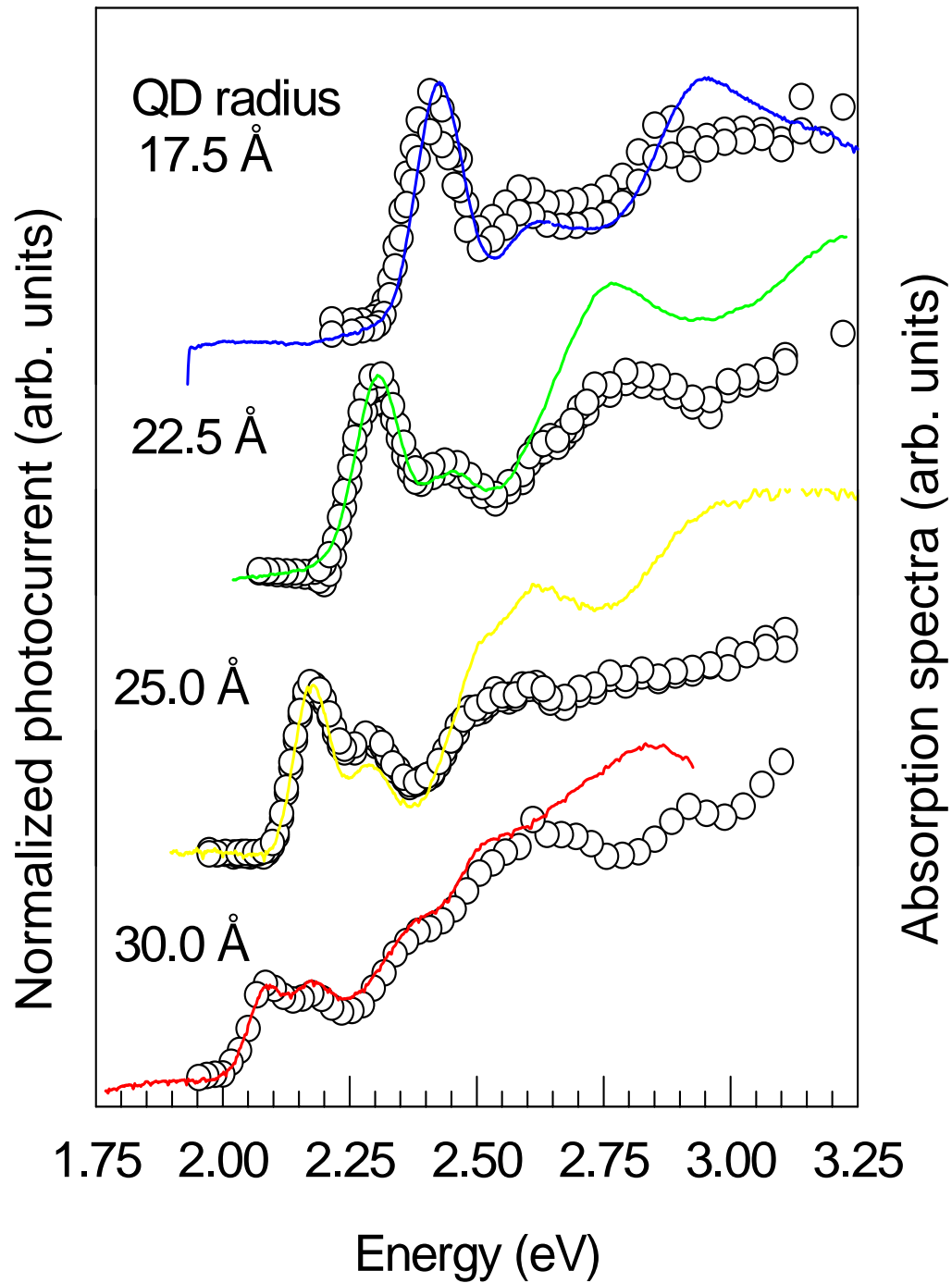
Figure 1.9: Spectral dependence of the photoconductivity of a film of CdSe QDs for four different sizes of QDs. Colored lines correspond to absorption spectra, and the open circles correspond to photocurrent data. From Leatherdale *et al.*

the functional form of which is given as:[28]

$$I(v) = \frac{\exp\left(\dfrac{-4\sqrt{2}\eta^2 d}{3m(ev-\gamma)}\left[\left(\dfrac{m\phi}{\eta^2}\right)^{3/2} - \left(\dfrac{m(\phi+\gamma-ev)}{\eta^2}\right)^{3/2}\right]\right)}{1+\exp\left(-\dfrac{\gamma-ev}{a}\right)} \tag{1.1}$$

where I is the photocurrent, v is the site-to-site potential, d is the QD spacing, m is the electron mass (taken in this model to be equal to the electron's rest mass), ϕ is the tunnel barrier height, γ is the energy difference between the initial and final states, e is the electron charge, and a describes to degree of wavefunction "tailing" outside of the QD.

Leatherdale *et al* report that the photoconductivity of CdSe QD films decreases with increasing temperature, without a change in the shape of the current-voltage curve (for most samples). This is attributed to the increase in the nonradiative exciton recombination rate with temperature, which leads to a decrease in the exciton ionization efficiency.

The QD films studied by Leatherdale *et al* are also found to have photocurrent that is linearly dependent on intensity. Because the photocurrent is not found to be transit-time limited, this indicates first-order recombination kinetics, as second-order (bimolecular) kinetics would produce a square-root dependence on intensity. The observed pseudo-monomolecular recombination kinetics are attributed to a large density of traps which serve as recombination centers for the majority carrier (assumed to be the electron); specifically, the density of traps must be much larger than the density of free carriers.

1.7 Thesis Overview

The work in this thesis concentrates on the interplay between chemistry and physics in the context of CdSe QD conductivity. In Chapter 2, initial efforts towards increasing QD conductivity through annealing are presented. While significant improvements in both dark conductivity and photoconductivity are observed, it proves to be difficult to describe exactly what changes the QDs, and especially the TOP/TOPO caps, undergo following high temperature (up to 430 $^{\circ}$C) annealing. Chapter 3 describes work undergone to enable photoconductivity studies of CdSe QDs synthesized using $Cd(acac)_2$ instead of dimethylcadmium. These efforts emphasize the fact that good physics requires good chemistry. The results of the achievement of good photoconductivity for films of CdSe QDs synthesized with $Cd(acac)_2$ are further discussed in Chapter 4. We find that these films are characterized by a low density of trapped charges, in contrast to previous results on films of QDs synthesized using dimethylcadmium. Chapter 5 is perhaps the strongest evidence of the interplay between chemistry and physics: here we use chemistry to greatly increase CdSe QD film photoconductivity, which leads us into a new regime of photophysics and a more complete picture of the physics behind CdSe QD conductivity.

1.8 References

1. M. A. Kastner, "Artificial Atoms," Physics Today **46**(24), 24-31 (1993).
2. J. M. Moison, F. Houzay, F. Barthe, L. Leprince, E. Andre, and O. Vatel, "Self-Organized Growth of Regular Nanometer-Scale InAs Dots on GaAs," Applied Physics Letters **64**(2), 196-198 (1994).
3. D. Leonard, M. Krishnamurthy, C. M. Reaves, S. P. Denbaars, and P. M. Petroff, "Direct Formation of Quantum-Sized Dots from Uniform Coherent Islands of InGaAs on GaAs-Surfaces," Applied Physics Letters **63**(23), 3203-3205 (1993).
4. B. O. Dabbousi, J. RodriguezViejo, F. V. Mikulec, J. R. Heine, H. Mattoussi, R. Ober, K. F. Jensen, and M. G. Bawendi, "(CdSe)ZnS core-shell quantum dots: Synthesis and characterization of a size series of highly luminescent nanocrystallites," Journal of Physical Chemistry B **101**(46), 9463-9475 (1997).
5. M. Nirmal, B. O. Dabbousi, M. G. Bawendi, J. J. Macklin, J. K. Trautman, T. D. Harris, and L. E. Brus, "Fluorescence intermittency in single cadmium selenide nanocrystals," Nature **383**(6603), 802-804 (1996).
6. B. R. Fisher, H. J. Eisler, N. E. Stott, and M. G. Bawendi, "Emission intensity dependence and single-exponential behavior in single colloidal quantum dot fluorescence lifetimes," Journal of Physical Chemistry B **108**(1), 143-148 (2004).
7. M. Bruchez, M. Moronne, P. Gin, S. Weiss, and A. P. Alivisatos, "Semiconductor nanocrystals as fluorescent biological labels," Science **281**(5385), 2013-2016 (1998).
8. Y. T. Lim, S. Kim, A. Nakayama, N. E. Stott, M. G. Bawendi, J. V. Frangioni, "Selection of quantum dot wavelengths for biomedical assays and imaging," Molecular Imaging **2**(1), 50-64 (2003).
9. S. Kim, Y. T. Lim, E. G. Soltesz, A. M. De Grand, J. Lee, A. Nakayama, J. A. Parker, T. Mihaljevic, R. G. Laurence, D. M. Dor, L. H. Cohn, M. G. Bawendi, and J. V. Frangioni, "Near-infrared fluorescent type II quantum dots for sentinel lymph node mapping," Nature Biotechnology **22**(1), 93-97 (2004).
10. M. Dahan, T. Laurence, F. Pinaud, D. S. Chemla, A. P. Alivisatos, M. Sauer, and S. Weiss, "Time-gated biological imaging by use of colloidal quantum dots," Optics Letters **26**(11), 825-827 (2001).
11. D. R. Larson, W. R. Zipfel, R. M. Williams, S. W. Clark, M. P. Bruchez, F. W. Wise, and W. W. Webb, "Water-soluble quantum dots for multiphoton fluorescence imaging in vivo," Science **300**(5624), 1434-1437 (2003).
12. B. Dubertret, P. Skourides, D. J. Norris, V. Noireaux, A. H. Brivanlou, and A. Libchaber, "In vivo imaging of quantum dots encapsulated in phospholipid micelles," Science **298**(5599), 1759-1762 (2002).
13. L. Manna, D. J. Milliron, A. Meisel, E. C. Scher, and A. P. Alivisatos, "Controlled growth of tetrapod-branched inorganic nanocrystals," Nature Materials **2**(6), 382-385 (2003).
14. L. Manna, E. C. Scher, and A. P. Alivisatos, "Shape control of colloidal semiconductor nanocrystals," Journal of Cluster Science **13**(4), 521-532 (2002).

15. L. Manna, E. C. Scher, and A. P. Alivisatos, "Synthesis of soluble and processable rod-, arrow-, teardrop-, and tetrapod-shaped CdSe nanocrystals," Journal of the American Chemical Society **122**(51), 12700-12706 (2000).

16. W. W. Yu, Y. A. Wang, and X. G. Peng, "Formation and stability of size-, shape-, and structure-controlled CdTe nanocrystals: Ligand effects on monomers and nanocrystals," Chemistry of Materials **15**(22), 4300-4308 (2003).

17. E. C. Scher, L. Manna, and A. P. Alivisatos, "Shape control and applications of nanocrystals," Philosophical Transactions of the Royal Society of London Series a-Mathematical Physical and Engineering Sciences **361**(1803), 241-255 (2003).

18. L. S. Li, J. T. Hu, W. D. Yang, and A. P. Alivisatos, "Band gap variation of size- and shape-controlled colloidal CdSe quantum rods," Nano Letters **1**(7), 349-351 (2001).

19. S. Kim and M. G. Bawendi, "Oligomeric Ligands for luminescent and stable nanocrystal quantum dots," Journal of the American Chemical Society **125**(48), 14652-14653 (2003).

20. N. Gaponik, D. V. Talapin, A. L. Rogach, A. Eychmuller, and H. Weller, "Efficient phase transfer of luminescent thiol-capped nanocrystals: From water to nonpolar organic solvents," Nano Letters **2**(8), 803-806 (2002).

21. H.-J. Eisler, V. C. Sundar, M. G. Bawendi, M. Walsh, H. I. Smith, and V. Klimov, "Color-selective semiconductor nanocrystal laser," Applied Physics Letters **80**(24), 4614-4616 (2002).

22. V. C. Sundar, H.-J. Eisler, and M. G. Bawendi, "Room-temperature, tunable gain media from novel II-VI nanocrystal-titania composite matrices," Advanced Materials **14**(10), 739-743 (2002).

23. S. Coe-Sullivan, W. K. Woo, J. S. Steckel, M. Bawendi, and V. Bulovic, "Tuning the performance of hybrid organic/inorganic quantum dot light-emitting devices," Organic Electronics **4**(2-3), 123-130 (2003).

24. S. Coe, W. K. Woo, M. G. Bawendi, and V. Bulovic, "Electroluminescence from single monolayers of nanocrystals in molecular organic devices," Nature **420**(6917), 800-803 (2002).

25. V. L. Colvin, M. C. Schlamp, and A. P. Alivisatos, "Light-Emitting-Diodes Made from Cadmium Selenide Nanocrystals and a Semiconducting Polymer," Nature **370**(6488), 354-357 (1994).

26. B. O. Dabbousi, M. G. Bawendi, O. Onitsuka, and M. F. Rubner, "Electroluminescence from Cdse Quantum-Dot Polymer Composites," Applied Physics Letters **66**(11), 1316-1318 (1995).

27. C. Kagan, "The Electronic and Optical Properties of Close Packed Cadmium Selenide Quantum Dot Solids," (Massachusetts Institute of Technology, Cambridge, 1996).

28. C. A. Leatherdale, C. R. Kagan, N. Y. Morgan, S. A. Empedocles, M. A. Kastner, and M. G. Bawendi, "Photoconductivity in CdSe quantum dot solids," Physical Review B **62**(4), 2669-2680 (2000).

29. M. V. Jarosz, N. E. Stott, M. Drndic, N. Y. Morgan, M. A. Kastner, and M. G. Bawendi, "Observation of bimolecular carrier recombination dynamics in close-packed films of colloidal CdSe nanocrystals," Journal of Physical Chemistry B **107**(46), 12585-12588 (2003).

30. M. V. Jarosz, V. P. Porter, B. R. Fisher, M. A. Kastner, and M. G. Bawendi, "Photoconductivity studies of treated CdSe quantum dot films exhibiting increased exciton ionization efficiency," submitted to Physical Review B (2004).

31. M. Drndic, M. V. Jarosz, N. Y. Morgan, M. A. Kastner, and M. G. Bawendi, "Transport properties of annealed CdSe colloidal nanocrystal solids," Journal of Applied Physics **92**(12), 7498 (2002).

32. W. U. Huynh, J. J. Dittmer, and A. P. Alivisatos, "Hybrid nanorod-polymer solar cells," Science **295**(5564), 2425-2427 (2002).

33. W. U. Huynh, J. J. Dittmer, N. Teclemariam, D. J. Milliron, A. P. Alivisatos, and K. W. J. Barnham, "Charge transport in hybrid nanorod-polymer composite photovoltaic cells," Physical Review B **67**(11), 115326 (2003).

34. A. L. Efros and M. Rosen, "Quantum size level structure of narrow-gap semiconductor nanorystals: Effect of band coupling," Physical Review B **58**(11), 7120-7135 (1198).

35. A. L. Efros and A. L. Efros, "Interband absorption of light in a semiconductor sphere," Soviet Physics Semiconductors **16**(7), 772-775 (1982).

36. L. E. Brus, "A simple model for the ionization potential, electron affinity, and aqueous redox potentials of smal semiconductor crystallites," Journal of Chemical Physics **79**(11), 5566-5571 (1983).

37. O. Madelung, ed., *Crystal and Solid State Physics*, Landolt Bornstein Numerical Data and Functional Relationships in Science and Technology (Springer-Verlag, Berlin, 1982), Vol. 17b: Physics of II-VI and I-VII Compounds, Semimagnetic Semiconductors.

38. C. B. Murray, "Synthesis and Characterization of II-VI Quantum Dots and Their Assembly into 3D Quantum Dot Superlattices," (Ph.D. Thesis, Massachusetts Institute of Technology, Cambridge, MA, 1995).

39. P. Guyot-Sionnest, M. Shim, C. Matranga, and M. Hines, "Intraband relaxation in CdSe quantum dots," Physical Review B **60**(4), R2181-R2184 (1999).

40. P. Guyot-Sionnest and M. A. Hines, "Intraband transitions in semiconductor nanocrystals," Applied Physics Letters **72**(6), 686-688 (1998).

41. M. Shim, S. V. Shilov, M. S. Braiman, and P. Guyot-Sionnest, "Long-lived delocalized electron states in quantum dots: A step-scan Fourier transform infrared study," Journal of Physical Chemistry B **104**(7), 1494-1496 (2000).

42. M. Shim and P. Guyot-Sionnest, "N-type colloidal semiconductor nanocrystals," Nature **407**(6807), 981-983 (2000).

43. M. Shim, C. J. Wang, and P. Guyot-Sionnest, "Charge-tunable optical properties in colloidal semiconductor nanocrystals," Journal of Physical Chemistry B **105**(12), 2369-2373 (2001).

44. C. J. Wang, M. Shim, and P. Guyot-Sionnest, "Electrochromic nanocrystal quantum dots," Science **291**(5512), 2390-2392 (2001).

45. C. J. Wang, M. Shim, and P. Guyot-Sionnest, "Electrochromic semiconductor nanocrystal films," Applied Physics Letters **80**(1), 4-6 (2002).

46. M. Shim, C. J. Wang, D. J. Norris, and P. Guyot-Sionnest, "Doping and charging in colloidal semiconductor nanocrystals," Mrs Bulletin **26**(12), 1005-1008 (2001).

47. M. Shim and P. Guyot-Sionnest, "Intraband hole burning of colloidal quantum dots," Physical Review B **64**(24), 245342 (2001).

48. D. Yu, C. J. Wang, and P. Guyot-Sionnest, "n-type conducting CdSe nanocrystal solids," Science **300**(5623), 1277-1280 (2003).

49. V. I. Klimov, D. W. McBranch, C. A. Leatherdale, and M. G. Bawendi, "Electron and hole relaxation pathways in semiconductor quantum dots," Physical Review B **60**(19), 13740-13749 (1999).

50. V. I. Klimov and D. W. McBranch, "Femtosecond 1P-to-1S electron relaxation in strongly confined semiconductor nanocrystals," Physical Review Letters **80**(18), 4028-4031 (1998).

51. D. S. Ginger, A. S. Dhoot, C. E. Finlayson, and N. C. Greenham, "Long-lived quantum-confined infrared transitions in CdSe nanocrystals," Applied Physics Letters **77**(18), 2816-2818 (2000).

52. B. L. Wehrenberg, C. J. Wang, and P. Guyot-Sionnest, "Interband and intraband optical studies of PbSe colloidal quantum dots," Journal of Physical Chemistry B **106**(41), 10634-10640 (2002).

53. B. L. Wehrenberg and P. Guyot-Sionnest, "Electron and hole injection in PbSe quantum dot films," Journal of the American Chemical Society **125**(26), 7806-7807 (2003).

54. C. A. Leatherdale, "Photophysics of Cadmium Selenide Quantum Dot Solids," (Ph.D. Thesis, Massachusetts Institute of Technology, Cambridge, MA, 2000).

55. C. B. Murray, D. J. Norris, and M. G. Bawendi, "Synthesis and characterization of nearly monodisperse CdE (E = S, Se, Te) semiconductor nanocrystallites," Journal of the American Chemical Society **115**(19), 8706-8715 (1993).

56. J. E. Bowen Katari, V. L. Colvin, and A. P. Alivisatos, "X-Ray Photoelectron Spectroscopy of CdSe Nanocrystals with Applications to Studies of the Nanocrystal Surface," Journal of Physical Chemistry **98**, 4109 (1994).

57. M. Bawendi and N. E. Stott, "Preparation of nanocrystallites from metal-containing salts," U.S. Patent Number 2002071952 (June 13 2002).

58. B. K. H. Yen, N. E. Stott, K. F. Jensen, and M. G. Bawendi, "A continuous-flow microcapillary reactor for the preparation of a size series of CdSe nanocrystals," Advanced Materials **15**(21), 1858-+ (2003).

59. M. W. Yu and X. G. Peng, "Formation of high-quality CdS and other II-VI semiconductor nanocrystals in noncoordinating solvents: Tunable reactivity of monomers," Angewandte Chemie-International Edition **41**(13), 2368-2371 (2002).

60. Z. A. Peng and X. G. Peng, "Nearly monodisperse and shape-controlled CdSe nanocrystals via alternative routes: Nucleation and growth," Journal of the American Chemical Society **124**(13), 3343-3353 (2002).

61. L. H. Qu, Z. A. Peng, and X. G. Peng, "Alternative routes toward high quality CdSe nanocrystals," Nano Letters **1**(6), 333-337 (2001).

62. X. G. Peng, "Green chemical approaches toward high-quality semiconductor nanocrystals," Chemistry-a European Journal **8**(2), 335-339 (2002).

63. Z. A. Peng and X. G. Peng, "Formation of high-quality CdTe, CdSe, and CdS nanocrystals using CdO as precursor," Journal of the American Chemical Society **123**(1), 183-184 (2001).

64. D. V. Talapin, A. L. Rogach, A. Kornowski, M. Haase, and H. Weller, "Highly luminescent monodisperse CdSe and CdSe/ZnS nanocrystals synthesized in a

hexadecylamine-trioctylphosphine oxide-trioctylphospine mixture," Nano Letters **1**(4), 207-211 (2001).

65. W.-K. Woo, "Fabrication and Characterization of Quantum-Confined Optoelectronic Devices Based on CdSe Nanocrystals," (Ph. D. Thesis, Massachusetts Institute of Technology, Cambridge, MA, 2002).

66. M. A. Hines and P. Guyot-Sionnest, "Synthesis and characterization of stronly luminescing ZnS-Capped CdSe nanocrystals," Journal of Physical Chemistry **100**(2), 468-471 (1996).

67. C. B. Murray, C. R. Kagan, and M. G. Bawendi, "Self-Organization of Cdse Nanocrystallites into 3-Dimensional Quantum-Dot Superlattices," Science **270**(5240), 1335-1338 (1995).

68. C. R. Kagan, C. B. Murray, and M. G. Bawendi, "Long-range resonance transfer of electronic excitations in close-packed CdSe quantum-dot solids," Physical Review B **54**(12), 8633-8643 (1996).

69. C. R. Kagan, C. B. Murray, M. Nirmal, and M. G. Bawendi, "Electronic energy transfer in CdSe quantum dot solids," Physical Review Letters **76**(9), 1517-1520 (1996).

70. C. B. Murray, C. R. Kagan, and M. G. Bawendi, "Synthesis and characterization of monodisperse nanocrystals and close-packed nanocrystal assemblies," Annual Review of Materials Science **30**, 545-610 (2000).

71. N. Y. Morgan, C. A. Leatherdale, M. Drndic, M. V. Jarosz, M. A. Kastner, and M. Bawendi, "Electronic transport in films of colloidal CdSe nanocrystals," Physical Review B **66**(7), 075339 (2002).

72. M. Drndic, R. Markov, M. V. Jarosz, M. G. Bawendi, M. A. Kastner, N. Markovic, and M. Tinkham, "Imaging the charge transport in arrays of CdSe nanocrystals," Applied Physics Letters **83**(19), 4008-4010 (2003).

73. D. S. Ginger and N. C. Greenham, "Charge transport in semiconductor nanocrystals," Synthetic Metals **124**(1), 117-120 (2001).

74. D. S. Ginger and N. C. Greenham, "Charge injection and transport in films of CdSe nanocrystals," Journal of Applied Physics **87**(3), 1361-1368 (2000).

Chapter 2

Transport properties of annealed CdSe QD films[*]

2.1 Introduction

Electrons confined to nanometer-sized regions in semiconductors or metals have been the subject of intense study for many years. The quantization of charge and energy resulting from the confinement makes such regions, or quantum dots, behave like artificial atoms.[1] With recent advances in techniques for synthesizing large numbers of metallic and semiconductor nanocrystals (NCs), it is now possible to make large arrays of artificial atoms in which particle size, inter-particle separation and chemical composition are controlled.[2] This opens the possibility of creating artificial solids with tunable electrical and optical properties. For example, it has been demonstrated that a Langmuir film of silver NCs undergoes a metal-insulator transition as a function of the separation between NCs in the array.[3]

Solids composed of metallic NCs have transport properties that are well described by a model of collective charge transport in disordered arrays.[4] Whereas the large number of conduction electrons in the metallic NCs provide substantial screening of long-range Coulomb interactions between electrons on different NCs, semiconductor NCs make possible the study of artificial solids in which such long-range interactions are very large. In these systems, transport measurements may show collective effects of charge ordering recently proposed by Levitov et al.[5, 6]

---

[*] Much of this chapter has appeared in print (M. Drndic et al. J. Appl. Phys., **92**(12), 7498, 2002)

Previous studies of colloidal CdSe NCs separated by organic capping molecules have been preformed on the as-deposited NCs,[7-9] and in this work we explore the properties of annealed CdSe NC solids. These previous studies have shown that these artificial solids are surprisingly insulating. Long-range Coulomb interactions between charges on different NCs slow down the dynamics of the injected electrons, an effect best described by an electron (Coulomb) glass model.[10] The current decays over extremely long time scales in response to a voltage step, and there is no steady-state current.[7, 8]

In order to increase the electrical current through the CdSe NC solids, the tunneling of electrons between NCs must be enhanced. This can be achieved by decreasing the physical separation and the height of the tunnel barriers between NCs in the array. The inter-dot separation is originally set by the length of the organic capping molecule.[2] One way to decrease the inter-dot separation, while keeping the NC size the same, is to anneal the NC solid at temperatures well below the melting temperature of the NC cores. This idea has been used to facilitate transport in arrays of cobalt NCs.[11]

In this work we describe electrical transport measured at temperatures ranging from 6 K to 250 K in three-dimensional close-packed arrays of organically capped CdSe NCs,[2] as a function of annealing time and temperature. After the solids are annealed, three changes are observed. First, transmission electron microscopy (TEM) images confirm that the separation between NCs decreases with annealing. Second, the optical absorption spectrum changes: the excitonic peaks of the NC solids shift to lower energies and broaden with annealing. Both the TEM and the absorption data provide evidence that dots remain distinct after annealing. Finally, the electronic properties of the solid change, and annealing results in greatly enhanced dark current and photocurrent. The

dark current generally increases exponentially with voltage; the data are well-described by the form $I \approx V/R_o \, e^{|V|/V_o}$, where V is the voltage across the array of dots, and R_o and V_o are constants that depend on the properties of the array. We show that R_o and V_o both decrease as the solid is annealed, which corresponds to the measured current increasing by up to three orders of magnitude. Similar changes are observed in measurements of the photocurrent in annealed NC solids. This enhancement of the current cannot be explained by the observed decrease of inter-dot separation alone. Rather, it is likely that chemical changes in the inter-dot organic material during annealing reduce the tunnel barrier height. Our results suggest that controlled annealing can be a useful tool for improving the conduction properties of NC solids.

2.2 Experimental Details

CdSe nanocrystals are prepared with diameters D ranging from 4.3 nm to 6.1 nm, with the rms deviation $\sigma \approx 5\%D$ measured from optical absorption.[2] According to the methods of Murray et al.,[2, 12, 13] a precursor solution consisting of dimethylcadmium, tri-n-octylphosphine (TOP) and TOP selenide (TOPSe) is rapidly injected into tri-n-octylphosphine oxide (TOPO) which has been degassed under vacuum and then brought to 350 $^{\circ}$C under a nitrogen atmosphere. NCs synthesized according to these methods are capped with an organic molecule, tri-n-octylphosphine oxide (TOPO), which creates a large potential barrier for electrons moving between the NCs ($E_b \sim 1$ eV)[9], and whose length defines the surface-to-surface separation $d = (1.1 \pm 0.1)$ nm between nearest neighbor NCs.[2]
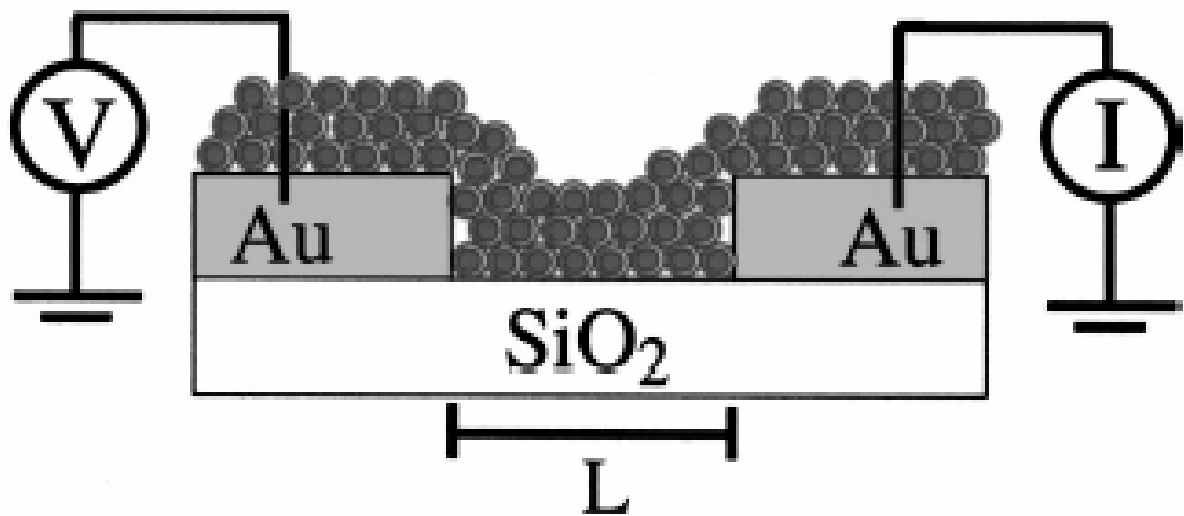
Figure 2.1: Schematic of the device used to study the electrical properties of close-packed CdSe NC solids. Gold electrodes, separated by distances of $L = 1$ μm and $L = 2$ μm, are microfabricated on quartz substrates. NC diameters vary from $D = 4.3$ nm to $D = 6.1$ nm in this work.

NC films are made according to previously established procedures.[2, 12, 14-17] The NCs are separated from all other chemicals present in the growth solution through three size-selective precipitations based on a solvent and non-solvent procedure.[12] Methanol is used as the non-solvent and hexane and butanol are used as the solvents. These methods results in a powder consisting of only NCs and the monolayer of TOP/TOPO required to passivate the NC surface. Close-packed films are made by drop casting from a concentrated solution containing the cleaned NCs and a 9:1 mixture of hexane:octane.

The NC solids are depositing on already electrically contacted devices, and are allowed to dry for several hours at room temperature in an inert atmosphere glovebox. Figure 2.1 is a schematic of the typical device geometry used in this study for electrical measurements of close-packed arrays of NCs, showing a film deposited on top of gold electrodes. The devices consist of microfabricated gold/titanium electrodes, 0.11 μm thick and 800 μm long, on insulating quartz substrates 0.5 mm thick. We have used separations between electrodes of $L = 1$ μm and 2 μm. Details of the device preparation are described in References[8, 9]. Most of the electrical measurements presented here correspond to a NC solid composed of approximately 10^9 TOPO-capped CdSe NCs between gold electrodes $L = 2$ μm apart. The thickness of the solid is ~ 0.4 μm (~ 70 monolayers), with a length corresponding to ~300 NCs between the electrodes.

For transport measurements, the CdSe NC solids are annealed in vacuum inside the cryostat, up to temperatures $T_a = 110$ ^{o}C. For $T_a > 110$ ^{o}C, samples are annealed in a separate system consisting of a hot plate in a forming gas atmosphere (95% nitrogen and 5% hydrogen). The samples are then transferred back into the cryostat for electrical measurements. Unless otherwise noted, the annealing time is 15 minutes if done in a

forming gas atmosphere, or $\approx$ 1 hour if done in vacuum (~10^{-6} Torr). We have annealed

one transport sample in forming gas at these lower temperatures ($T_a < 110$ °C) to ensure

that its electrical transport properties are similar to those of the samples annealed in

vacuum. For TEM measurements samples are deposited on carbon grids, and for

absorption measurements samples are deposited on glass slides. Both are annealed in a

forming gas atmosphere.

Electrical transport measurements are performed in vacuum ($p \approx 10^{-6}$ Torr) at

temperatures ranging from $T = 6$ K to $T = 250$ K, and at applied electric fields up to

$E = 2.5$x10^8 V/m. As illustrated in Fig. 1, a voltage V is applied across the electrodes and

a current I is measured with a current amplifier. Control measurements on substrates

without NCs ensure that the substrate conduction is negligible up to $T \sim 250$ K. The

current detection limit in our measurement system is $\sim$ 5 fA. A green light-emitting

diode (LED) is mounted ~3 mm above the device in the cryostat. The peak wavelength

of the LED is $\lambda \approx 565$ nm, and the power $P \approx 50$ μW. This allows us to photoexcite the

NCs and to measure photocurrent as a function of applied voltage.

2.3 Results

2.3.1 General results

The van der Waals attraction between NCs causes them to self-assemble into

hexagonal close-packed arrays, and these arrays can be imaged using TEM. TEM images

provide direct evidence that annealing decreases the inter-dot separation in the NC solid.

Figure 2.2 shows TEM images of arrays of CdSe NCs with $D \approx 6.1$ nm as deposited

[Figure 2.2(a)], and after annealing at 350 °C [Figure 2.2(b)] and 430 °C [Figure 2.2(c)].

54
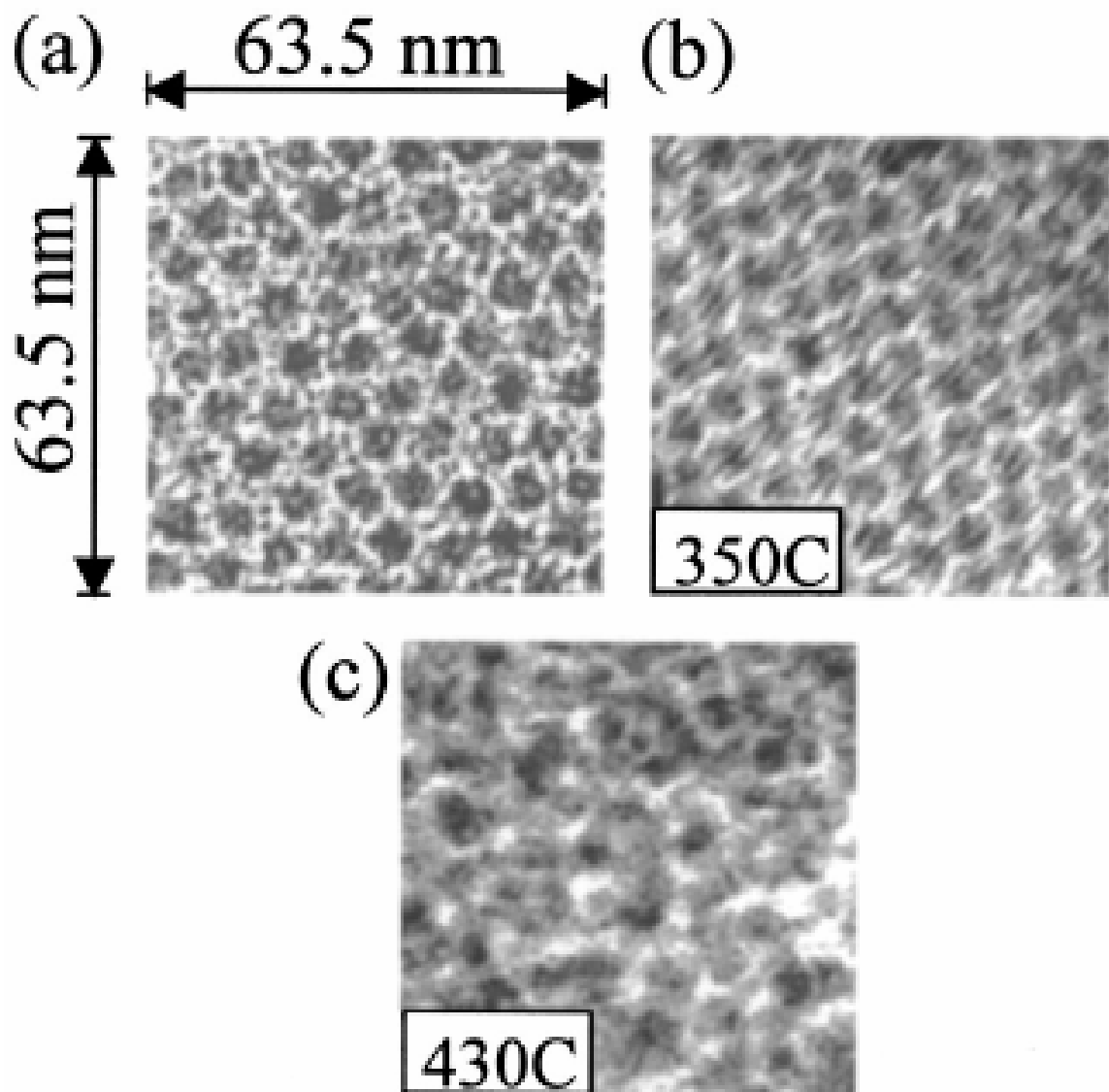
Figure 2.2: Transmission electron micrographs of CdSe NC solids with diameter $D =$ 6.1 nm: (a) as deposited, and after annealing in forming gas at (b) $T_a = 350\,^{\circ}$C and (c) $T_a = 430\,^{\circ}$C. The interdot separations found from these data are $d \approx 1.1$ nm for (a) and $d \approx$ 0.5 nm for (b). The NCs are no longer distinct at $430\,^{\circ}$C.

To estimate the average NC separation in Figures 2.2(a) and 2.2(b) we have counted the number of NCs in the fixed sample area $A = 63.5 \times 63.5$ nm^2 shown in Figure 2.2. There are $N \approx 78$ dots counted in this area before annealing, whereas there are $N \approx 94$ dots after annealing at 350 °C. From the TEM data, the NC sizes after annealing at 350 °C appear unchanged. More significantly, we see no evidence of broadening of the size distribution. Given these observations, and since $N \propto A/(D+d)^2$ and $d \approx 1.1$ nm (see Reference [2]) for the unannealed sample, we estimate that the inter-dot separation is reduced to $d \sim 0.5$ nm after annealing at 350 °C. After heating at 430 °C, the NCs no longer appear distinct in the TEM images [Figure 2.2(c)].

In addition to sample characterization with TEM, optical absorption measurements have been used to characterize the distribution of NC sizes and to probe the coupling of the NCs to their environment.[2, 18, 19] Figure 2.3(a) shows the evolution of the absorption spectrum for an array of TOPO-capped CdSe NCs with $D \approx 4.9$ nm as deposited and after annealing at $T_a = 110$, 300 and 350 °C. The absorption spectra in Figure 2.3 are shifted vertically for clarity and the positions of the band-edge peaks are indicated. In all of the spectra, the first (i.e., reddest) peak corresponding to the size-dependent band gap is clearly visible. As the annealing temperature is increased, the absorption spectrum shifts to the red and the peaks broaden. The presence of clear and sharp size-dependent excitonic features in the spectra of the annealed solids is additional evidence that the dots are still distinct. After annealing we observe an increased background in the absorption spectra, which has a long tail at red wavelengths. We infer from its wavelength dependence that it arises from scattering in the film. There may also be contributions from absorption of the pyrolyzed organic material.
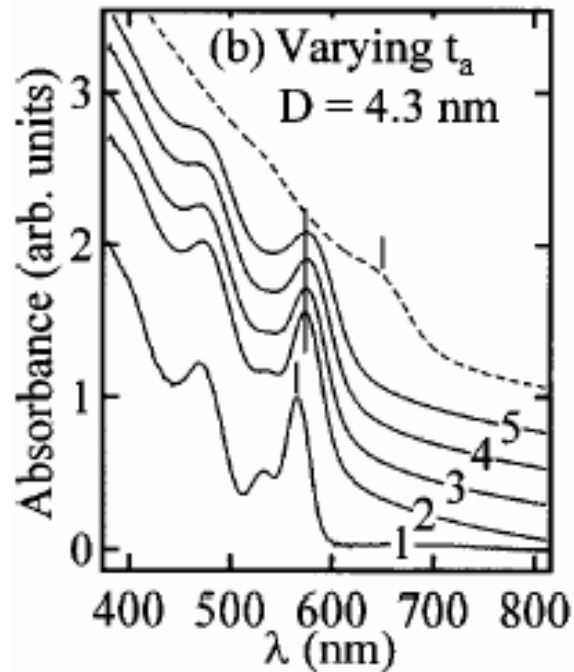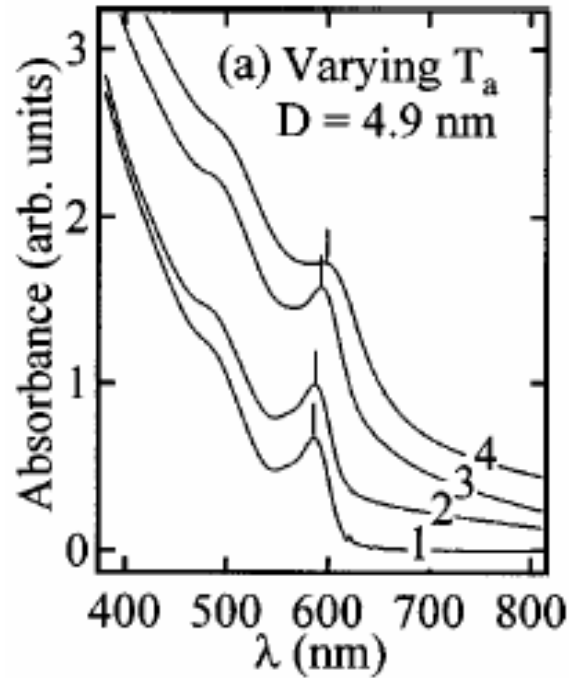
Figure 2.3: Absorption spectra of CdSe NC solids deposited on glass slides before annealing (curve 1) and after annealing in forming gas as a function of (a) annealing temperature T_a, for $D = 4.9$ nm and (b) annealing time t_a, for $D = 4.3$ nm. The absorption spectra are shifted vertically for clarity and the positions of the band-edge peaks are indicated. (a) The curves labeled 1-4 are as-deposited, and then after annealing at $T_a =$ 110, 300, and 350 °C, respectively. (b) The curves labeled 1-5 are as prepared and annealed at 350 °C for $t_a =$ 5, 10, 15, 35 min., respectively. The dashed curve is for the same film after annealing at $T_a = 400$ °C for 10 minutes.

The band-edge peak at $\lambda \approx 587$ nm ($E = 2.11$ eV) in the as-prepared film shifts by $\Delta E \approx -5, -30$, and -40 meV after annealing at $T_a = 110$, 300 and $350\ ^{\circ}$C, respectively. As a reference, the band gap of bulk CdSe corresponds to $E = 1.8$ eV ($\lambda \approx 690$ nm),[20] whereas the peak after annealing at $350\ ^{\circ}$C is at 2.07 eV.

Figure 2.3(b) shows the evolution of the absorption spectrum for one array of smaller TOPO-capped CdSe dots with $D \approx 4.3$ nm as deposited and after annealing at $T_a = 350\ ^{\circ}$C for annealing times of $t = 5, 10, 15$ and 35 minutes. A subsequent annealing at $T_a = 400\ ^{\circ}$C for $t = 10$ minutes is also shown by the dashed curve. Curves 2 - 5 in Figure 2.3(b) indicate that the effect of annealing for longer times at the same temperature ($T_a = 350\ ^{\circ}$C) is to increase the width of the peak while affecting its position only slightly. The band edge peak, which is at $\lambda \approx 566$ nm ($E \approx 2.19$ eV) before annealing, shifts by $\Delta E \approx -30$ meV after annealing at $T_a = 350\ ^{\circ}$C for 5 minutes. After subsequent annealing at $T_a = 350\ ^{\circ}$C for longer times, the band-edge peak shifts by only $\Delta E \approx -5$ meV from curve 2 to curve 5. After annealing at $T_a = 400\ ^{\circ}$C, the peak shifts by $\Delta E \approx -290$ meV (with respect to the as-prepared sample) to $E = 1.9$ eV, making it very close to the gap of bulk CdSe.

From the TEM and absorption data, we have confidence that the dots are still physically distinct after annealing, as long as $T_a \leq 350\ ^{\circ}$C. We now describe how the transport properties of the annealed NC solids. Figure 2.4 shows typical current-voltage (*I-V*) curves on log-linear plots of a NC solid measured at $T = 77$ K. Measurements are shown both in the dark [Figure 2.4(a)] and with illumination from the LED [Figure 2.4(b)], for the film as-deposited (labeled I), and after annealing at $T_a = 110\ ^{\circ}$C (labeled II) and $T_a = 300\ ^{\circ}$C (labeled III). The solid lines in Figures 2.4(a) and 2.4(b) represent voltage sweeps at a rate $\Delta V/\Delta t \approx 1$ V/s from $V = 0$ to positive voltages and back to $V = 0$,
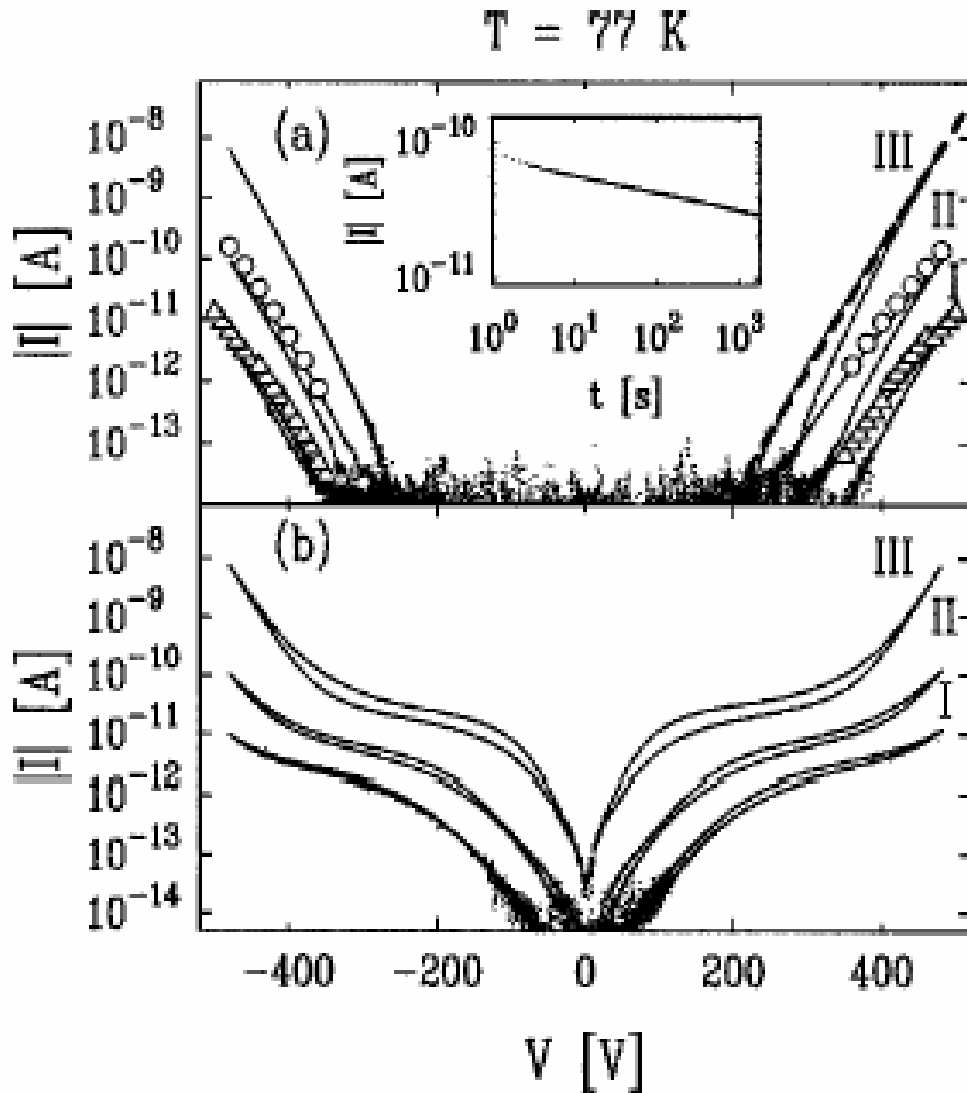
Figure 2.4: Current-voltage curves of a CdSe NC solid at $T = 77$ K (a) in the dark, and (b) during illumination with a green LED. Curves labeled I - III are for the as prepared film, and after annealing at $T_a = 110$ and 300 °C, respectively. The NC diameter is $D = 4.9$ nm for the film used. In (a) the solid lines represent voltage sweeps at a rate $\Delta V/\Delta t \approx 1$ V/s from $V = 0$ to positive voltages and back to $V = 0$, and then symmetrically to negative voltages and back to $V = 0$. Triangles (Δ) and circles ($\bigcirc$) are the amplitudes of the current at 1s after applying a voltage step ($V = 0$ for $t < 0$, $V = V_{el}$ for $t \geq 0$). The dashed line represents the exponential fit for curve III. Inset: One current transient, which is well-described by $I(t) \approx 78\, t^{-0.13}$ pA (t is in seconds), for an applied voltage step at $V = -460$ V after annealing at 110 °C.

and then symmetrically to negative voltages and back to $V = 0$. The triangles ($\triangle$) and circles ($\bigcirc$) in Figure 2.4(a) are the amplitudes of the dark current at 1 s after applying a voltage step ($V = 0$ for $t < 0$, $V = V_{el}$ for $t \geq 0$), for the films as-deposited ($\triangle$) and after annealing at 110 °C ($\bigcirc$).

We first focus on the dark-current data of Figure 2.4(a). These clearly show the following features: (i) a hysteresis in the *I-V* curves, (ii) an approximately exponential increase of the current with voltage, and (iii) an increased current through the solid after annealing. We next discuss these features in turn.

2.3.2 (i) *I-V* curve hysteresis

The hysteresis is such that the measured current is larger as the voltage sweeps up, from $|V| = 0$ to 500 V. This hysteresis in the *I-V* curves is consistent with transient measurements, in which we apply voltage steps of the form $V = 0$ for $t < 0$, and $V = V_{el}$ for $t \geq 0$, and observe the current $I(t)$ decreasing as a power law in time, $I(t) = I_o t^{-\alpha}$ for $t \geq 0$.[8] We have measured 30 minute long current transients $i(t)$ in response to voltage steps up to $|V| = 500$ V. One such current transient, for an applied voltage step at $V = -460$ V after annealing at 110 °C is shown in the inset of Figure 2.4 (a). This current transient is well-described by $I(t) = 78t^{-0.13}$ pA (t is in seconds). Similarly, the current transients at other applied voltages are well-described by power laws $I(t) = I_o t^{-\alpha}$. We find that the exponent $\alpha = (0.11 \pm 0.04)$ and that α is independent of the applied voltage V.

Although the current decays in time in response to a voltage step, and there is no steady-state current, the small values of α correspond to extremely slow decays of the current. We find no significant change of $\alpha \sim 0.1$ with annealing. As shown in Figure

60

2.4(a), the amplitudes of the dark current at 1 s after applying a voltage step, which are represented by triangles ($\triangle$) and circles ($\bigcirc$), are in good agreement with the current values measured by sweeping V.

2.3.3 (ii) Exponential increase of current with voltage

The measured current is well-described by an exponential form: we choose an exponential fit with a linear prefactor, $I \approx V/R_o\, e^{|V|/V_o}$, in order to extract a characteristic voltage V_o [V], and an equivalent resistance R_o [Ω] of the array. For illustration, one such exponential fit is represented by a dashed line for curve II in Figure 2.4(a). From such exponential fits to the data in Figure 2.4(a), we obtain V_o and R_o for voltage sweeps up, from $|V| = 0$ to 500 V. For the i-V curve before annealing (curve I), we find $V_o \approx 31$ V and $R_o \approx 7\text{x}10^{20}$ Ω. R_o corresponds to a large sheet resistance of $\sim 10^{23}$ Ω per square.

2.3.4 (iii) Increased current after annealing

The measured current increases as the NC solid is annealed (curves II and III). The current after annealing at 300 $^{\text{o}}$C (curve III) is approximately three orders of magnitude larger than the original current (curve I) at fixed $|V| \approx 500$ V. The I-V curves after annealing are also slightly steeper, corresponding to a decrease in V_o. From exponential fits to curves I – III in Figure 2.4(a), as illustrated for curve II with a dashed line, we find V_o decreases from ≈ 31 to 23 V, and R_o decreases from $\approx 7\text{x}10^{20}$ to $1\text{x}10^{20}$ Ω.

Using the LED in the cryostat, we have also performed preliminary measurements of the photocurrent through NC solids before and after annealing. For the as-deposited NC solids before annealing, a detailed study of the photocurrent can be found in

Reference [9]. Figure 2.4(b) shows the corresponding current-voltage curves for the same

sample as in Figure 2.4(a), under constant excitation from the LED, before annealing

(labeled I) and after annealing at temperatures $T_a = 110$ °C (labeled II) and $T_a = 300$ °C

(labeled III). From Figure 2.4(b) we see that, like the dark current, the photocurrent is

also enhanced by annealing. In the voltage range where the dark current is negligible ($|V|$

< 200 V), the photocurrent increases by up to two orders of magnitude after the NC solid

is annealed at $T_a = 300$ °C.

From Figure 2.4(b), it also appears that the photocurrent saturates at large electric

fields ($E > 10^8$ V/m). This saturation of photocurrent has not been observed in previous

studies of as-deposited NC solids, presumably because lower fields have been used.[9]

Although this saturation is an interesting feature that might be useful for applications, its

origin has to be investigated further. At fields larger than $E \approx 2x10^8$ V/m, the rise in the

current appears to correspond to the onset of dark current [compare with Figure 2.4(a)].

Because the LED is not monochromatic and because the intensity of light incident on the

sample is not well controlled, more detailed photocurrent measurements using laser

excitation are underway to investigate the origin of this saturation of the photocurrent.

The *I-V* curves in Figure 2.4 are presented as functions of voltage across the NC

solid. However, when *I-V* curves for NC solids with $L = 1$ μm and $L = 2$ μm are

compared, we find that both the dark and photocurrent scale with the electric field ε.

Specifically, the dark current follows $I \propto e^{\varepsilon/\varepsilon_o}$, where $\varepsilon_o = V_o/L$, and ε_o is independent of

the gap size L. We have confirmed this dependence for both the as-deposited and

annealed samples.

2.3.5 Measurements on NCs with varying parameters

The measurements described above have been performed on NC solids with different parameters, including gap size L [see Figure 2.1(a)], NC diameter D, annealing temperature T_a, and time. The results are summarized for TOPO-capped NCs in Table 2.1. Here V_o is the exponent from the exponential fits to I-V curves for $L = 2$ μm. The other fit parameter R_o is, to a first approximation, inversely proportional to the film thickness. R_o ranges from ~10^{22} to ~10^{25} Ω per square for solids from ~1 to ~ 0.01 μm thick. The effects of annealing on transport do not depend on whether or not voltages are applied to the sample before annealing. We have also observed enhanced dark current and photocurrent for samples that have been stored at room temperature in vacuum ($p \sim$ 10^{-6} Torr) for several days. Finally, the results presented above are for NCs solids deposited on quartz substrates, but we have also successfully used annealing to improve the conductivity of NC solids deposited on degenerately doped Si substrates with a thermally grown gate oxide (SiO_2).

Table 2.1: Summary of results for TOPO-capped CdSe NC solids as a function of NC diameter, D, and annealing temperature, T_a. V_0 is the exponent from fits to I-V curves for $L = 2$ μm.

Sample	D (nm)	T_a (°C)	V_0 (V)
A	6.1	RT	78 ± 1
A	6.1	350	32 ± 5
B	4.9	RT	31 ± 4
B	4.9	110	28 ± 2
B	4.9	300	23 ± 5
C	4.3	350	21 ± 1

2.4 Discussion

We have demonstrated enhancement of the dark current and photocurrent in NC solids and the corresponding red-shift and broadening of the absorption spectra. The dark current is found to be approximately an exponential function of the applied electric field. The functional form of the *I-V* curves is approximately preserved after annealing, but the current increases by several orders of magnitude. In addition, TEM data show that the interdot separation decreases upon annealing.

Redshifts in the absorption spectra of NC systems have been previously observed as a function of the solvent composition,[18, 19] NC diameter and concentration.[21, 22] These redshifts have been attributed to the enhancement of either classical (dipole) coupling,[18] or quantum mechanical coupling between NCs.[21, 22]

The redshifts in this work can be attributed to the change in polarization energy of the quantum-confined exciton when the dielectric environment around the NCs is changed. In the mean field approximation the average dielectric constant of the medium around each NC, ε_m, can be estimated as the volume-weighted average of dielectric constants for the organic spacer ($\varepsilon_r = 2.1$)[18, 19] and for the CdSe NC ($\varepsilon_r = 6.2$)[18, 19]. This is done by assuming a close-packed 3D array of CdSe NC and using the following relationship:

$$\varepsilon_m = \varepsilon_r + 4\sqrt{2}\pi / 3(6.2 - \varepsilon_r)[R/(2R+d)]^3, \qquad (2.1)$$

where R is the NC radius, ε_r is the dielectric constant of TOPO, the factor of 6.2 is the dielectric constant of CdSe, and d is the surface-to-surface separation. When the interdot separation decreases, ε_m increases because the volume fraction of CdSe increases. The average dielectric constant ε_m can also increase because the dielectric constant of the

organic material surrounding the NCs may increase with annealing. Correspondingly, the excitonic peak shifts to lower energies. The core-shell model of Reference [18, 19] can be applied in our case. From the TEM data we have found that the interdot separation decreases from $d = 1.1$ to ~ 0.5 nm after annealing at $\sim 350\ ^{\circ}C$, which here corresponds to the first excitonic peak shifting by $\Delta E \sim -40$ meV. Taking $\varepsilon_r = 2.1$ for TOPO and $\varepsilon_r = 6.2$ for CdSe NCs, and calculating ε_m using Equation (2.1), the model of Equations (5) and (6) in References [18, 19] predicts that the change in NC spacing results in an energy shift of $\Delta E \sim -10$ meV, which is smaller than what is observed experimentally. Agreement is obtained only if, in addition to a decrease in the interdot separation, one assumes that the dielectric constant of the organic cap increases slightly during annealing, from $\varepsilon_r = 2.1 \sim 3$. Such a change in ε_r can arise from chemical changes in the organic material during annealing, when TOPO decomposes into a carbonaceous substance under elevated temperatures. Correspondingly, the average dielectric constant of the medium ε_m increases from $\varepsilon_m = 3.8$ to 4.7 both because the dielectric constant of the organic cap increases and because the interdot separation decreases.[23] It should be noted that, while this analysis the average dielectric constant was estimated as a volume average as given by Equation (2.1), another way to estimate the average dielectric constant is to use the Maxwell Garnett theory.[24] This theory predicts a very similar result, predicting that the average dielectric constant of the medium, ε_m, increases from $\varepsilon_m \sim 3.5$ to ~ 4.4. Using either analysis, the magnitude of the observed absorption spectrum redshifts in this work can therefore be understood to result from the increase in the dielectric constant of the environment surrounding an individual NC.

We find only a weak temperature dependence of the dark current in the

measurement temperature range of T = 6 K to T = 250 K; in particular, the exponent V_o in exponential fits of the *I-V* curves is approximately temperature independent. This weak temperature dependence suggests that electron tunneling is the main transport mechanism in CdSe NC solids for T < 250 K. References [7, 8] provide evidence that the dark current is limited by electron tunneling from a space-charge region near the electron-injecting contact into unoccupied dots. Similar behavior has been observed in linear chains of carbon particles for voltages lower than the threshold predicted for collective transport across the array.[25] As discussed below, the transport measurements shown here suggest that Coulomb correlations play a major role in the transport through CdSe NC solids, before and after annealing.

For the dark current measurements in Figure 2.4(a), we find that an approximately temperature-independent exponential form $I \propto e^{|V|/Vo}$ of the current-voltage curves; qualitatively, this form is expected for electron tunneling, and results from the lowering of the interdot potential barriers when an electric field is applied across the NC solid. However, a simple tunneling model fails to fit our dark current-voltage curves accurately; this model predicts a value for the coefficient V_0 which is larger by two orders of magnitude than observed experimentally. This can be shown by estimating the probability for electron tunneling $|T|^2$ from once NC to its nearest neighbor. In the semiclassical approximation,

$$|T|^2 \sim \exp\left[-2\int_0^d dx \sqrt{(2m^*/\eta^2)(E_b - E_0 - e\varepsilon x)}\right], \qquad (2.2)$$

where $m^* \approx 0.1m_e$ (Reference [20]) is the effective electron mass in CdSe, $\varepsilon \approx V/(E_m L)$ is the electric field inside the NC solid, d is the width of the barrier, E_b is the height of the barrier, and E_0 is the ground state energy inside a NC. For small applied voltages per NC

compared with the barrier height ($e\varepsilon d \ll E_b - E_0$), this expression reduces to

$$|T|^2 \sim \exp(\beta V),\tag{2.3}$$

consistent with the form observed experimentally. However,

$$\beta = \sqrt{(2m^*/\eta^2)(E_b - E_0)^{-1}}\ ed^2/(2\varepsilon_m L),\tag{2.4}$$

and for $d = 1.1$ nm, $L = 2\ \mu$m, $\varepsilon_m = 4.7$ [for $D = 5$ nm; see Equation (2.1)], and assuming $E_b - E_0 \sim 1$ eV,[9] we find that $V_0 \sim 7\text{x}10^3$ V, whereas the measured value is ~ 30 V, two orders of magnitude smaller.

In order to obtain agreement between the simple tunneling model in Equations (2.2) – (2.4) and our measurements, we would have to assume that the barrier height $E_b - E_0$ is $\sim 20\ \mu$eV, because the order of magnitude of the other parameters, barrier width d, and the dielectric constant ε_m are known from other measurements.[2, 9] Such a value for the barrier height seems unreasonably small for tunneling between the conductions states of CdSe NCs into an organic molecule (TOPO), and indeed, a larger value of the order $\sim$ 1 eV was found to fit the previous photocurrent measurements.[9]

The increased current after annealing is most likely caused by a combination of the decreased separation and the chemical transformation of the organic caps during annealing. When the width of the tunnel barrier is decreased by $|\Delta d|$, the tunneling probability is expected to increase by $\sim e^{\alpha|\Delta d|}$ ($\alpha^{-1} \sim 0.1$ nm for alkane molecules[9]). For annealing at 350 $^{\circ}$C, we have found $|\Delta d| \sim 0.6$ nm, so the tunneling probability is expected to increase by a factor of ~ 400. This is consistent with results for the dark current, but smaller than observed for the photocurrent at small applied voltages. Previous photocurrent measurements[9] were made with a different organic cap, tri-*n*-

butylphosphine oxide (TBPO), whose length is $d = (0.7 \pm 0.1)$ nm^2, and whose barrier

height is similar to that of TOPO. These studies have shown that the tunneling

probability at low fields, inferred from the photocurrent *I-V* measurements, increases by a

factor of 5 times smaller than expected from a tunneling model with a barrier height of ~

1 eV when the barrier width is decreased. It is therefore likely that the changes in

transport properties with annealing are caused both by the decreased separation and by

the chemical transformation of the organic caps during annealing in a reducing

atmosphere. The transformation of the organic molecule TOPO into a carbonaceous

substance could lower the tunnel barrier between NCs.

We find that the characteristic voltage V_0 obtained from the exponential fits to the

I-V curves is comparable to the Coulomb interaction energies in the NC array. In the

measurements on different sample lengths, we have found that the current depends on the

electric field across the device. Therefore, for N NCs across the gap, $N \approx L/(D + d)$, the

exponential form of the dark current can be rewritten as $I \propto e^{v/v_0}$, where v is the applied

voltage difference across one NC in the array and $v_0 = V_0/N$. In estimating v_0 after

annealing we take into account the decrease of the interdot separation. We find that v_0 is

comparable to the Coulomb interaction energy E_{int} between charges on nearest-neighbor

NCs. Specifically, from the data in Table 2.1, we estimate $v_0 \sim 50 - 280$ meV. On the

other hand, for charges on nearest-neighbor NCs embedded in a medium of average

dielectric constant ε_m, the Coulomb interaction is $E_{int} = e^2/(4\pi\varepsilon_o\varepsilon_m(D + d))$. For $D = 4.9$

nm, $d = 1.1$ nm, and $\varepsilon_m \approx 3.7$ [from Equation (2.1)], we find $E_{int} \sim 60$ meV, which is of

the same order of magnitude as v_o. This agreement between v_o and the Coulomb

interaction energy E_{int} between electrons on nearest-neighbor NCs seems to suggest the

importance of Coulomb interactions in the tunneling current. However, while the conductance through arrays of metallic NCs has been studied theoretically,[4] we do not have a theoretical treatment of tunneling limited by long-range Coulomb interactions that might explain the exponential voltage dependence of the dark current.

We also find that the changes of v_o (= V_0/N) after annealing are comparable to the redshifts ΔE of the NC band edge absorption peak. For example, in Figure 2.3(a) for D = 4.9 nm, we find $\Delta E \sim$ -30 meV after annealing at 300 ^{o}C, whereas the corresponding change in v_o, found from the data in Figure 2.4(a), is $\Delta v_o \sim$ - 20 meV. These two quantities should be comparable if both of them reflect the Coulomb interaction between electron charges at a distance comparable to the NC diameter D. Specifically, we propose that the redshifts reflect the Coulomb interaction energy of the electron-hole pair, whereas v_o reflects the Coulomb interaction energy between electrons on nearest-neighbor NCs.

2.5: Conclusions

We have demonstrated that annealing of NC solids reduces the distance between NCs and alters their optical and transport properties. Annealing results in greatly enhanced dark current and photocurrent in NC solids; this is ascribed to an enhancement of interdot tunneling. Annealing also results in redshifts of the absorption spectra that may be due to the change in the dielectric environment surrounding the NCs. Our measurements suggest that Coulomb interactions between electrons on neighboring NCs play an important role in the tunneling current, both before and after annealing. Controlled annealing might serve as a useful tool to tune the properties of NC arrays and

facilitate the observation of new collective phenomena.

2.6: References

1.   M. A. Kastner, "Artificial Atoms," Physics Today **46**(24), 24-31 (1993).
2.   C. B. Murray, C. R. Kagan, and M. G. Bawendi, "Synthesis and characterization of monodisperse nanocrystals and close-packed nanocrystal assemblies," Annual Review of Materials Science **30**, 545-610 (2000).
3.   C. P. Collier, R. J. Saykally, J. J. Shiang, S. Henrichs, and J. R. Heath, "Reversible tuning of silver quantum dot monolayers through the metal-insulator transition," Science **277**(5334), 1978-1981 (1997).
4.   A. A. Middleton and N. S. Wingreen, "Collective transport in arrays of small metallic dots," Physical Review Letters **71**(19), 3198-3201 (1993).
5.   L. S. Levitov and B. Kozinsky, "Charge ordering and hopping in a triangular array of quantum dots," Los Alamos National Laboratory Preprint Archive, Condensed Matter, Preprint number 9912484 (2003).
6.   D. S. Novikov, B. Kozinsky, and L. S. Levitov, "Ordered and disordered electron states in a quantum dot array," Los Alamos National Laboratory Preprint Archive, Condensed Matter, Preprint Number 0111345 (2001).
7.   D. S. Ginger and N. C. Greenham, "Charge injection and transport in films of CdSe nanocrystals," Journal of Applied Physics **87**(3), 1361-1368 (2000).
8.   N. Y. Morgan, C. A. Leatherdale, M. Drndic, M. V. Jarosz, M. A. Kastner, and M. Bawendi, "Electronic transport in films of colloidal CdSe nanocrystals," Physical Review B **66**(7), 075339 (2002).
9.   C. A. Leatherdale, C. R. Kagan, N. Y. Morgan, S. A. Empedocles, M. A. Kastner, and M. G. Bawendi, "Photoconductivity in CdSe quantum dot solids," Physical Review B **62**(4), 2669-2680 (2000).
10.   W. Xue and P. A. Lee, "Monte Carlo simulations of the electron glass," Physical Review B **38**(13), 9093-9098 (1988).
11.   C. T. Black, C. B. Murray, R. L. Sandstrom, and S. Shouheng, "Spin-dependent tunneling in self-assembled cobalt-nanocrystal superlattices," Science **290**(5494), 1131-1134 (2000).
12.   C. B. Murray, D. J. Norris, and M. G. Bawendi, "Synthesis and characterization of nearly monodisperse CdE (E = S, Se, Te) semiconductor nanocrystallites," Journal of the American Chemical Society **115**(19), 8706-8715 (1993).
13.   C. B. Murray, "Synthesis and Characterization of II-VI Quantum Dots and Their Assembly into 3D Quantum Dot Superlattices," (Ph.D. Thesis, Massachusetts Institute of Technology, Cambridge, MA, 1995).
14.   C. Kagan, "The Electronic and Optical Properties of Close Packed Cadmium Selenide Quantum Dot Solids," (Ph.D. Thesis, Massachusetts Institute of Technology, Cambridge, MA, 1996).
15.   C. B. Murray, C. R. Kagan, and M. G. Bawendi, "Self-Organization of Cdse Nanocrystallites into 3-Dimensional Quantum-Dot Superlattices," Science **270**(5240), 1335-1338 (1995).

16. C. R. Kagan, C. B. Murray, and M. G. Bawendi, "Long-range resonance transfer of electronic excitations in close-packed CdSe quantum-dot solids," Physical Review B **54**(12), 8633-8643 (1996).

17. C. R. Kagan, C. B. Murray, M. Nirmal, and M. G. Bawendi, "Electronic energy transfer in CdSe quantum dot solids," Physical Review Letters **76**(9), 1517-1520 (1996).

18. C. A. Leatherdale and M. G. Bawendi, "Observation of solvatochromism in CdSe colloidal quantum dots," Physical Review B **63**(16), 5315 (2001).

19. M. Iwamatsu, M. Fujiwara, N. Happo, and K. Horii, "Effects of dielectric discontinuity on the ground-state energy of charged Si dots covered with a SiO2 layer," Journal of Physics: Condensed Matter **9**, 9881 (1997).

20. H. Landolt and R. Bornestein, *Numerical Data and Functional Relationships in Science and Technology* (Springer-Verlag, Berlin, 1961).

21. M. V. Artemyev, A. I. Bibik, L. I. Gurinovich, S. V. Gaponenko, and U. Woggon, "Evolution from individual to collective electron states in a dense quantum dot ensemble," Physical Review B **60**(3), 1504-1506 (1999).

22. O. I. Micic, S. P. Ahrenkiel, and A. J. Nozik, "Synthesis of extremeley small InP quantum dots and electronic coupling in their disordered solid films," Applied Physics Letters **78**(25), 4022-4024 (2001).

23. C. P. Collier, T. Vossmeyer, and J. R. Heath, "Nanocrystal superlattices," Annual Review of Physical Chemistry **49**, 371-404 (1998).

24. J. C. Maxwell Garnett, "Colours in metal glasses and in metallic films," Philosophical Transactions of the Royal Society of London Series A-Mathematical Physical and Engineering Sciences **203**, 385-420 (1904).

25. A. Bezyradin, R. M. Westervelt, and M. Tinkham, "Self-assembled chains of graphitized carbon naoparticles," Applied Physics Letters **74**(18), 2699-2701 (1999).

Chapter 3

Enabling photoconductivity studies of QDs synthesized using Cd(acac)$_2$

3.1 Introduction

Because photoconductivity measurements are sensitive to the optical, electronic, and structural properties of CdSe QD films, they prove to be an excellent probe of the quality of as-synthesized QDs, as well as the quality of QD films. This chapter is intended to be a phenomenological account of how QD synthesis chemistry and QD film preparation affect photoconductivity measurements. It is a great example of how chemistry and physics are intimately connected. Simply put, good physics requires good samples.

About two and a half years ago, the nanocrystal synthesis procedures in the Bawendi lab underwent two major changes. The first was that a new method was developed by N. E. Stott[1] to synthesize CdSe QDs using a cadmium salt (cadmium acetylacetonate, or Cd(acac)$_2$) rather than the highly toxic and pyrophoric dimethylcadmium.[2, 3] This prep also allows the use of 99% tri-*n*-octylphosphine oxide (TOPO), rather than the 90% that is required for the dimethylcadmium-based prep. This change was soon followed by a second. We ran out of our "magic" lot of tri-*n*-octylphosphine (TOP) that had served us well for so many years. Both of these changes

proved to have an enormous impact on photoconductivity measurements of CdSe QD films.

Chapter 4 will more deeply investigate the consequences of the Cd(acac)$_2$ synthesis on the physics of photoconductivity.[4] This chapter focuses only on how the magnitude of the photocurrent is affected by how the QDs and QD films are prepared. Specifically, we find that the photoconductivity is strongly affected by which lot of 90% TOP is used to synthesize the QDs. We show that this irreproducibility between lots of TOP can be minimized by purifying the TOP, and a successful purification procedure is presented. The photoconductivity also proves to be highly dependent on how exactly the QDs are cleaned prior to film deposition, especially when purified TOP is used. The procedures for making films using CdSe QDs prepared with dimethylcadmium are not sufficiently rigorous to obtain high photoconductivity using QDs synthesized with Cd(acac)$_2$. We present a modified procedure for size-selecting and making films of QDs prepared with Cd(acac)$_2$. Unfortunately, we also find that TOP can easily be contaminated. While the source of the contamination was not identified, we show that a contaminated bottle of TOP can affect the magnitude of the measured photoconductivity by over three orders of magnitude.

3.2 Experimental Methods

3.2.1 CdSe QD preparation

CdSe QDs with a diameter of ~ 5 nm are synthesized according to the methods developed by N. E. Stott.[1] A solvent mixture consisting of 6.25 g tri-*n*-octylphosphine oxide (TOPO, Sigma-Aldrich, 99%), 5.75 g hexadecylamine (HDA, Sigma-Aldrich,

90%), and 3.4 mL tri-*n*-octylphosphine (TOP, 90%) is degassed for two hours under vacuum at 140 ^{o}C. Meanwhile, 0.317 g of Cd(acac)$_2$ (1 mmol, Alfa Aesar, 98%), 0.5686 g of 1,2-hexadecanediol (HDDO, 2.2 mmol, Sigma-Aldrich, 90%), and 8 mL of TOP (90%) are degassed together for one hour under vacuum at 100 ^{o}C. When this mixture has cooled to room temperature, 2 mL of 1.5 M TOPSe are added. After the TOPO solution has finished degassing, it is brought under an inert atmosphere and heated to 360 ^{o}C, where it is usually allowed to stay for ~ 1- 2 minutes. At this point, the heating mantle and glass wool are quickly removed, and the precursor mixture (Cd(acac)$_2$, HDDO, TOP, and TOPSe) is rapidly injected into the hot TOPO solution. CdSe nanocrystals are formed nearly immediately, and the desired size is achieved without further heating. After injection, the sample is allowed to stir at 80 ^{o}C for 0 – 24 hours, at which point 5 mL of hexane are added prior to cooling the sample to room temperature (to prevent solidification).

The QD samples presented in this chapter (labeled Sample A – I in Figure 3.1) are all synthesized according to the above method. However, they use various different manufacturers and batches of TOP, as is indicated in Figure 3.1. Samples A and B use aliquots of QDs from the same prep, which uses TOP manufactured by Fluka from a lot labeled in Figure 3.1 as "lot 1" (this is what is referred to in Section 3.1 as the "magic" lot of TOP). Sample C is from a different QD prep, but the prep is synthesized with the same bottle of Fluka TOP. Sample D is from yet a different QD prep that is synthesized with that same bottle of Fluka TOP, except that the bottle is surmised to have become contaminated by that point. Sample E is from a QD prep synthesized using a different lot of Fluka TOP, labeled in Figure 3.1 as "lot 2." Sample F uses QDs synthesized with TOP

Sample	TOP	Fluor.	Freezer?	# Filter Steps	Loaded Air-Free?	i(250 V), pA
A	Fluka – lot 1	Good	No	0	No	7.1
B	Fluka – lot 1	Good	No	1	No	1000
C	Fluka – lot 1	Good	No	1	Yes	5200
D	Fluka – lot 1 - contaminated	Good	No	2	Yes	1.7
E	Fluka – lot 2	Good	No	1	Yes	7.0
F	Alfa – G02L25	Good	No	1	Yes	1300
G	Alfa- I25L01	Poor	No	1	Yes	5.5
H	Alfa – I25L01 -purified	Great	No	1	Yes	58
I	Alfa – I25L01 -purified	Great	Yes	2	Yes	930

Figure 3.1: Summary of CdSe QD film samples. "Fluor." refers to a qualitative description of the quality of the fluorescence from the QDs in the growth solution; "# filter steps" refers to how many times during the size selection procedure the sample was filtered from the butanol/hexane mixture – 1 means only before the last precipitation with methanol, and 2 means before the second and last methanol precipitations (all samples were filtered once from the hexane/octane solution prior to film deposition); "Freezer?" refers to whether or not the sample was put in the freezer and centrifuged prior to beginning the size selection; "loaded air-free?" refers to whether the sample was loaded into the cryostat inside of an inert atmosphere glove box or not; "i(250 V)" refers to the photocurrent at 250 V and an excitation power of ~1 mW.

manufactured by Alfa Aesar, with a lot number (as designated by Alfa Aesar) of G02L25.

Sample G uses QDs synthesized with TOP manufactured by Alfa Aesar under lot number

I25L01. Samples H and I use QDs from the same prep, which are also synthesized using

Alfa Aesar TOP from lot I25L01; however, in this case the TOP is purified through a

column of basic alumina prior to use, as is described below in Section 3.2.2

3.2.2 TOP purification

The apparatus used for the purification of the TOP (for the QDs of Samples H and

I) is shown in Figure 3.2. For larger volumes of TOP than are used in the work in this

chapter, a pre-fabricated column with a round reservoir has been used. For the samples

studied in this chapter, only 50 mL of TOP is purified, so the column consists of an air

condenser fitted with a separate 50 mL round reservoir. The column is packed with ~ 10

g activated basic alumina (Sigma-Aldrich, listed as: aluminum oxide, activated, basic,

Brockman I, standard grade, ~ 150 mesh). All septa (on top of the round reservoir, on the

second neck of the pear collection flask, and on the final receptacle for the TOP) are

reinforced with wire to ensure that the argon pressure does not force off any of the septa.

Before adding the TOP, the apparatus and the activated alumina are purged well with

argon.

The TOP is added into the round reservoir in an air-free manner using a canula.

The TOP is then slowly pushed through the column of activated alumina with a positive

pressure of argon. While the unpurified TOP that is added to the round reservoir has a

slight yellow hue, the TOP that emerges from the column appears to be clear. After
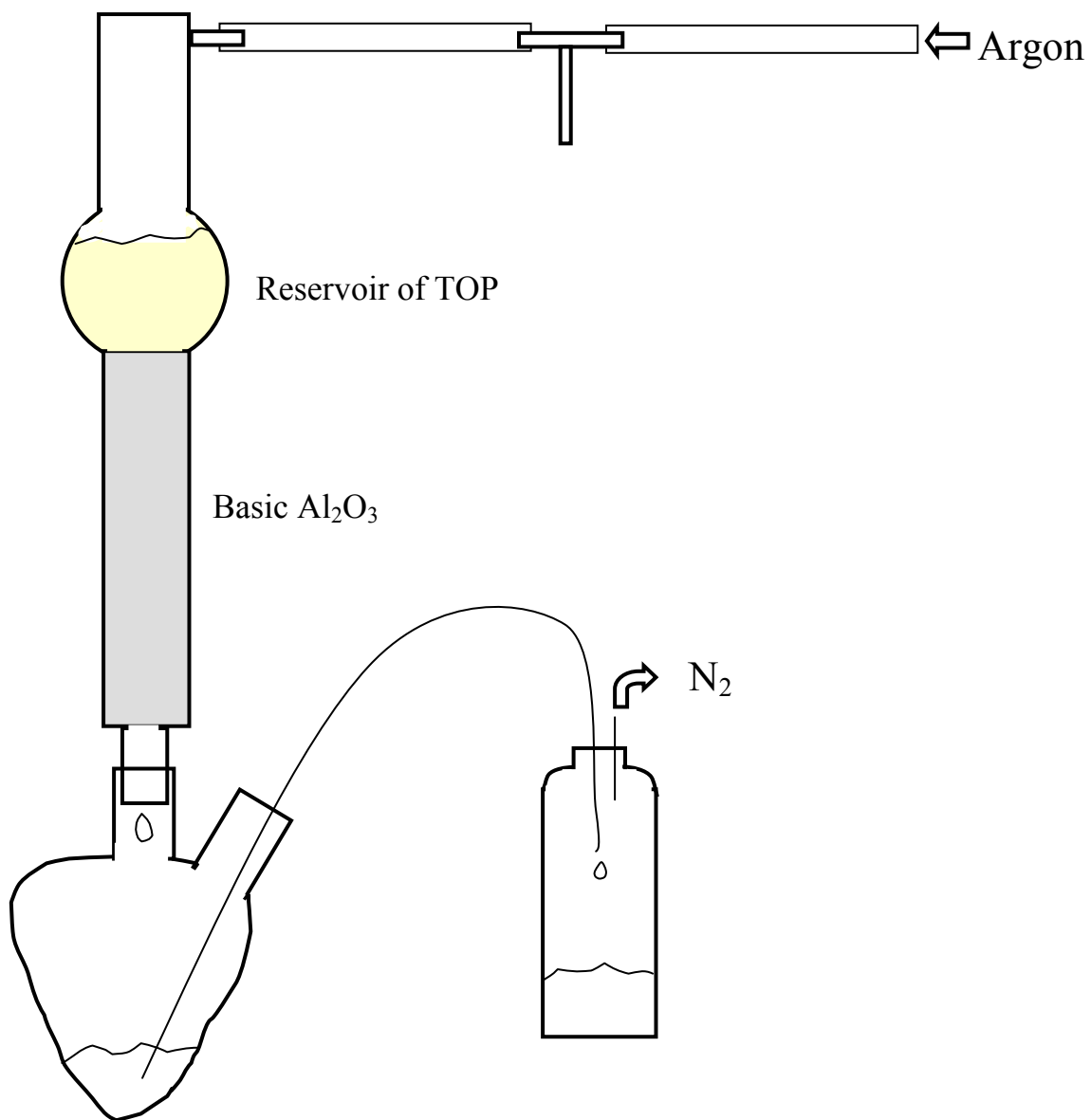
Figure 3.2: Air-free apparatus for purifying TOP through a column of basic alumina. Some caution should be taken with all of the glass joint seals and the rubber septa on top of the column and TOP receptacle, as the filtering is done at a relatively high argon pressure.

purification, the TOP is stored under an argon atmosphere on a Schlenk line (for the samples studied in this chapter) or in an inert atmosphere glove box.

3.2.3 Size selection

The procedures used for the size selection of the QD samples presented in this chapter are based on previously established methods.[2, 3] The benefits of size selection are two-fold. First, as the term suggests, the size distribution of the QD sample is narrowed, which facilitates better close-packing in QD films. Second, size-selection also serves as a washing procedure, isolating the QDs from the rest of the chemicals present in the growth solution. For QDs synthesized using dimethylcadmium, the QDs primarily need to be separated from excess TOP/TOPO in the growth solution, so that the final solution for film deposition consists of only QDs and the monolayer of TOP/TOPO necessary to passivate and solvate the QDs.

However, as is obvious from the much longer list of reagents, the growth solution of QDs synthesized using $Cd(acac)_2$ consists of far more than just excess TOP and TOPO. Therefore, the size-selection procedure ultimately has to be modified. Various different procedures were tried before settling on the optimum procedure (which is used for Sample I).

For all samples, a 5 mL aliquot of QDs is taken from the growth solution (after 5 mL of hexane has been added to it, as described in Section 3.2.1). For Samples A-H, the aliquot of QDs is centrifuged for 5 minutes at 3900 rpm, in an attempt to remove any precipitate. For Sample I, the 5 mL aliquot is first placed in the freezer for 15 minutes (with as much additional hexane as is necessary to keep the sample from freezing, which

is usually ~ 2 – 3 mL), which encourages additional material (that appears to be white in color) to precipitate from the growth solution. The QDs used for Sample I are also centrifuged for 5 minutes at 3900 rpm to remove the precipitate. Much more precipitate is removed from Sample I than from Samples A-H, due to the additional step in the freezer.

For all of the samples, the supernatant is decanted after centrifugation; the precipitate (and any QDs that may have gotten trapped in it) is discarded. 5 mL of butanol is added to the supernatant. With the QD sample stirring, methanol is added drop-wise until flocculation of the QDs is first observed; this is referred to as the endpoint. An additional 1 mL of methanol is added, and the solution is then centrifuged for 5 minutes at 3900 rpm. The supernatant is discarded, and the precipitate is dissolved in ~ 3 mL each hexane and butanol.

For Samples D and I only, the solution at this point is filtered through a 0.2 μm PTFE syringe filter. Then, for all samples, a second precipitation with methanol is performed. After reaching the endpoint, ~ 10 additional drops of methanol (from a buret) are added. This solution is centrifuged for 5 minutes at 3900 rpm; the supernatant is again discarded. The precipitate is dissolved in ~ 2 mL each of hexane and butanol.

For Samples B - H only, the solution at this point is filtered through a 0.2 μm PTFE syringe filter. For Sample I only, the solution at this point is filtered through a 0.1 μm PTFE syringe filter. For all samples, a third precipitation with methanol is then performed, again adding ~ 10 drops of methanol after the endpoint has been reached. After centrifugation for 5 minutes at 3900 rpm, the supernatant is discarded and the

precipitate is dissolved in a minimal volume of anhydrous hexane. This solution is dried under vacuum at room temperature.

3.3.4 Film deposition

The film deposition procedure used for the samples presented in this chapter is based on previously established methods.[2, 3, 5-9] For all of the samples, the dried sample of QDs obtained after the size-selection process is dissolved in ~ 1 mL 9:1 hexane: octane. For Samples A – H, this solution is filtered through a 0.2 μm PTFE syringe filter. For Sample I, the QD solution is filtered though a 0.02 μm aluminum oxide syringe filter (Anotop 10, by Whatman). The pore size of the syringe filter used in this step is the only difference amongst Samples A - I with regards to the film deposition procedure. After filtration, a test film is drop cast from the QD solution onto a glass slide. Films on glass slides are used to determine the approximate thickness of the QD film, for the optical microscopy images in Figures 3.3 – 3.12 and Figure 3.14, and for the Atomic Force Microscopy (AFM) images in Figure 3.13.

The filtered solution of QDs is dried at room temperature under vacuum, brought under an inert atmosphere, and then brought into an inert atmosphere glove box. In the glove box, the QD sample is dissolved again in ~ 0.05 – 0.3 mL of 9:1 hexane: octane. This concentrated solution is drop cast onto the quartz devices used for photoconductivity measurements.

The quartz devices have photolithographically patterned gold electrodes, which are electrically contacted prior to film deposition. The quartz substrates are 0.5 mm thick,

and the electrodes are 800 μm long and 0.11 μm thick. The electrodes used for the experiments in this chapter are spaced by 2μm.

3.3.5 Photoconductivity measurements

For Samples A and B, the QD film samples are taken out of the glove box and loaded into a cold-finger cryostat in air. The cryostat is then quickly evacuated, so that the sample is only exposed to air for ~ 10 – 20 minutes. For Samples C – I, the cryostat is brought into the glove box and the samples are loaded into the cryostat inside of an inert atmosphere. The cryostat is then brought out of the glove box (filled with nitrogen and sealed) and evacuated as for Samples A and B. The final pressure in the cryostat is < 10^{-5} Torr. All of the photoconductivity measurements presented in this chapter are preformed at 77 K. The back of the quartz device is connected to ground.

A Kiethley 6517 electrometer is used to source voltage and to measure current. A 514 nm Ar^+ laser provides the photoexcitation, with a power of ~ 1 mW (illuminating a spot with a radius of ~ 1 – 2 mm). Current-voltage curves are acquired by stepping in 10 V steps from 0 V to the maximum voltage, $V_M \geq 250$ V, from $+ V_M$ to $- V_M$, and finally from $- V_M$ back to 0 V.

3.3.6 Optical microscopy

Optical microscopy images are taken of QD films deposited on glass slides. A Nikon optical microscope is used, with either a 10 X, 20 X, or 50 X objective.

3.3.7 Atomic Force Microscopy

Atomic Force Microscopy (AFM) images are taken using a Digital Instruments Nanoscope IIIa in D3000 tapping mode. A 5 μm x 5 μm area is scanned, with the forward direction of each line scan measuring topography and the reverse direction of each line scan recording phase information.

3.3 Results and Discussion

3.3.1 Filtration of film solution

Figure 3.3 shows optical microscopy images taken with a 10X objective. The film shown in Figure 3.3(a) is deposited from a sample of QDs (the same ones as those used for Sample C) in 9:1 hexane: octane before the solution is filtered through a 0.2 μm PTFE syringe filter. Figure 3.3(b) shows a film that is deposited from the same solution after filtration through a 0.2 μm PTFE syringe filter. Clearly, this final filtration step is crucial for the achievement of smooth, clear QD films that are free of contamination. It appears that this final filtrating step gets rid of particulates that are present in the final QD solution. These particulates could be dust, some additional solid organic substances, or possibly QDs that have aggregated.

3.3.2 Filtration during size selection

It seems, however, that filtration of the final solution of QDs in 9:1 hexane: octane is not sufficiently rigorous to achieve either high quality films or high levels of photocurrent. This can be seen by comparing Samples A and B; between these two samples, the only difference in their preparation is that Sample A is not filtered during the

(a)

500 μm
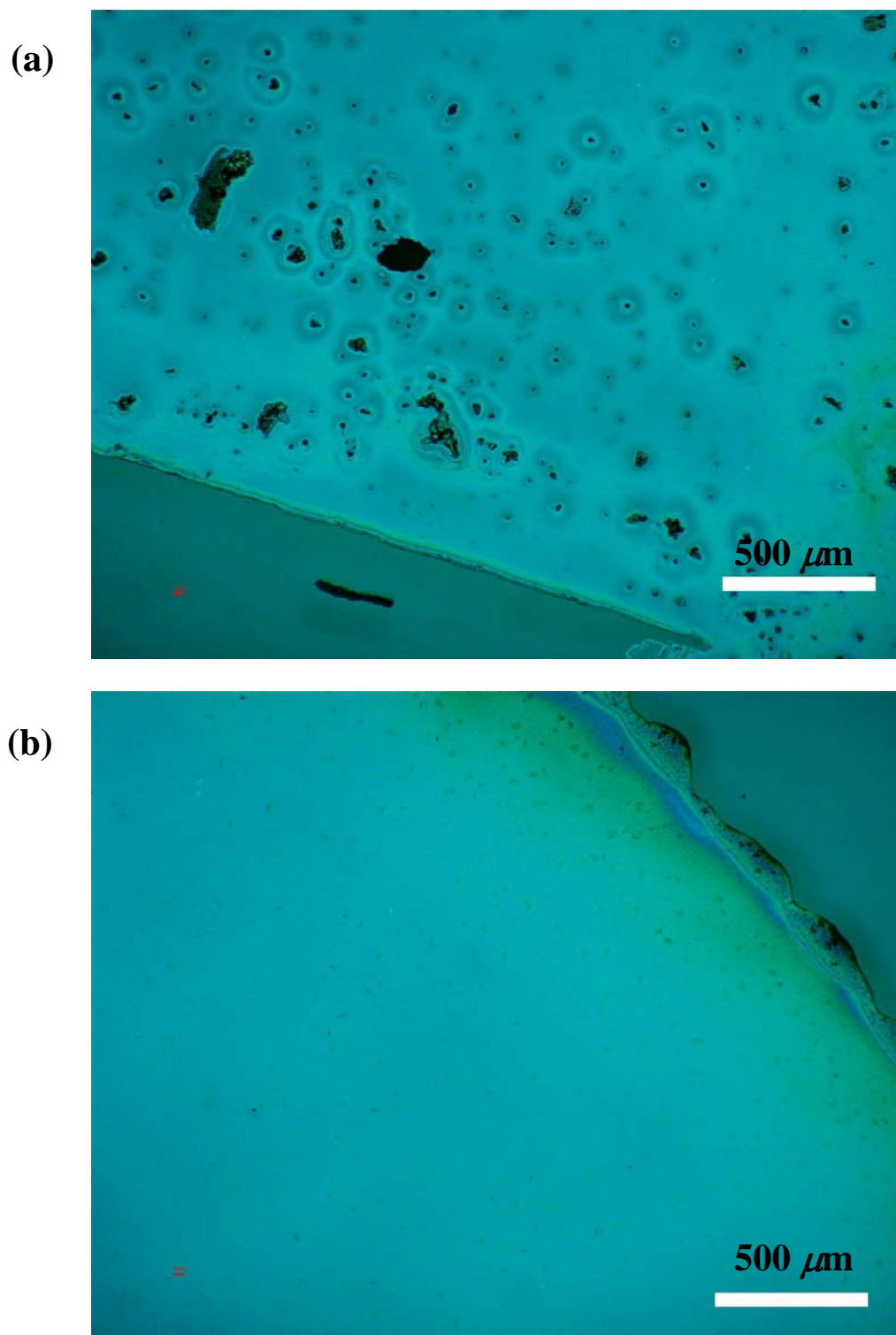
(b)

500 μm

Figure 3.3: The effects of filtering the final film solution prior to deposition. (a) Optical microscopy image of a film deposited from an unfiltered solution of 9:1 hexane: octane. (b) An optical microscopy image of a film deposited from the solution used to make the film in (a) after it has been filtered through a 0.2 μm syringe filter. This sample is sample C

size selection process, while the QDs used for Sample B are filtered through a 0.2 μm

PTFE syringe filter prior to the final precipitation with methanol. Figure 3.4(a) shows an

optical microscopy image of a film of QDs from Sample A deposited on a glass slide;

Figure 3.4(b) shows the photocurrent-voltage (*i-V*) curve for QDs from Sample A

deposited on a quartz electrical device. Similarly, Figure 3.5(a) shows an optical

microscopy image corresponding to Sample B, and Figure 3.5(b) shows an *i-V* curve

corresponding to Sample B. A comparison of Figures 3.4(a) and 3.5(a) clearly shows

that the film corresponding to Sample A is much dirtier than the film corresponding to

Sample B: while Figure 3.4(a) exhibits evidence of particulate matter, Figure 3.5(a)

seems to have evidence of only bubbles. Correspondingly, a comparison of Figures

3.4(b) and 3.5(b) clearly shows that Sample A has ~ 20 fold less photocurrent at 250 V

than Sample B.

Since the QD solutions in 9:1 hexane: octane for both Samples A and B are

filtered prior to film deposition, it is unlikely that the particulate matter in Figure 3.4(a) is

due to dust or aggregated QDs. The likely explanation seems to be that the particulate

matter corresponds to some organic substance that is crystallizing or precipitating as the

film of QDs dries. Apparently when the QD solution in hexane and butanol is filtered

prior to the last precipitation with methanol, much of this organic matter is filtered out.

Further evidence for this is that the QD solution in hexane and butanol appears slightly

cloudy prior to filtration, and clear after filtration. Furthermore, whatever is left in the

syringe filter is not colored, so it appears that it is not aggregated QDs that are making the

QD solution cloudy. This excess organic could be salts (known to be formed in the

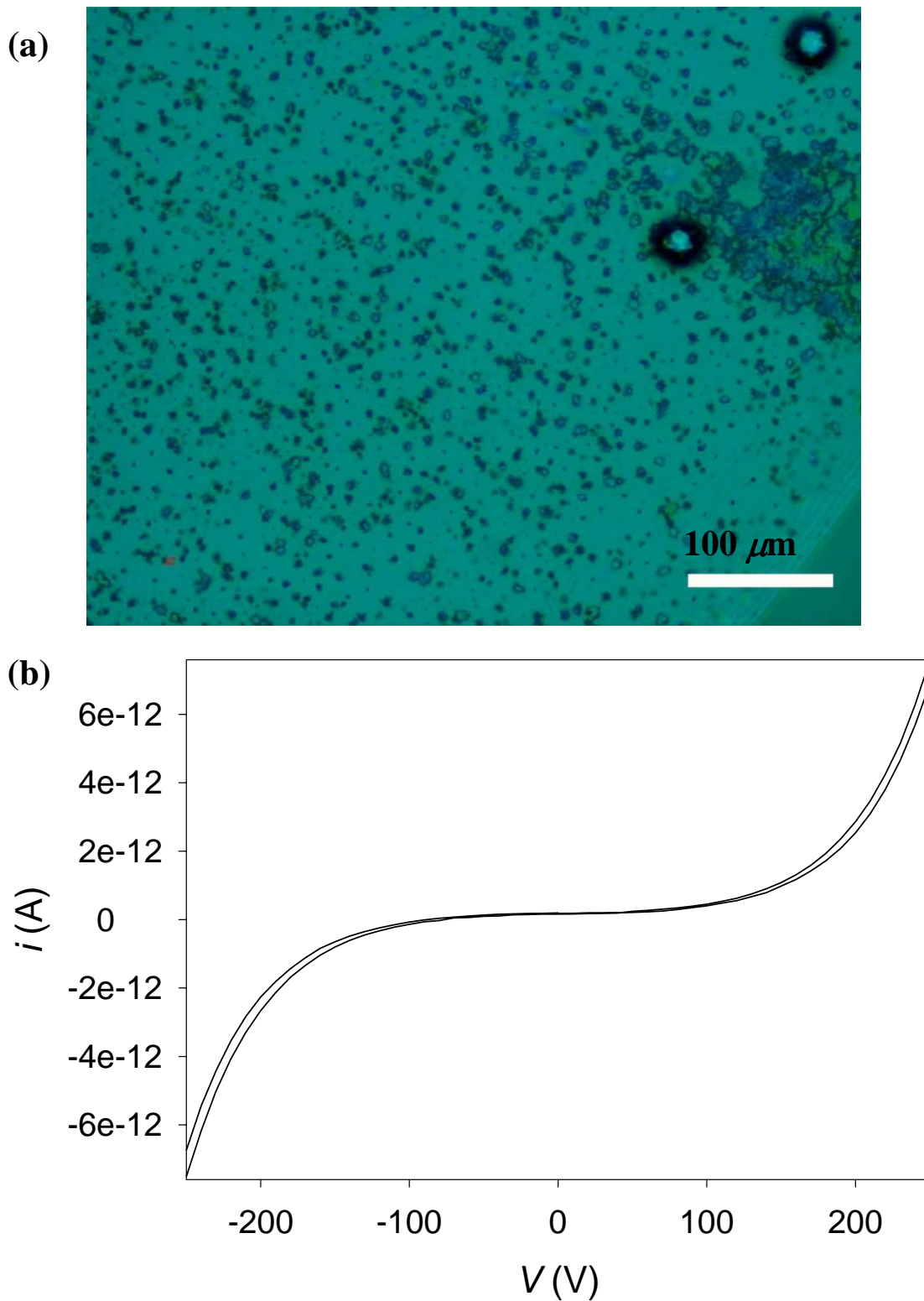**(a)**

(b)

Figure 3.4: Sample A. (a) Optical microscopy image of a film from Sample A deposited on a glass slide. (b) Current-voltage curve measured for Sample A, taken at 77 K on a 2μm gap with an excitation intensity of ~ 1mW.

growth solution), any of the extra ingredients (i.e., other than TOP and TOPO) of the

Cd(acac)$_2$ prep, or possibly other byproducts of the prep.

3.3.3 Loading samples into the cryostat air-free

In order to protect the QD films from oxidation, and to make results from sample

to sample not dependent on the varying time that it takes to load the sample into the

cryostat in air, we started to load the QD devices into the cryostat from within an inert

atmosphere glove box. This change is the only difference between Sample B (which is

loaded in air) and Sample C (which is never exposed to air). An optical microscopy

image and *i-V* curve for Sample B are given in Figures 3.5(a) and 3.5(b), respectively; the

corresponding data for Sample 3.6 are given in Figures 3.6(a) and 3.6(b). As is expected,

because the films on glass slides used for optical microscopy are not kept free from air

exposure, the structural characteristics of the QD film for Sample C remain very nice,

with only very small bubbles appearing in the film. However, the photocurrent is

improved 5 fold from the photocurrent for Sample B. There also appears to be a slightly

different shape to the *i-V* curve of Sample C. Similar changes are seen in QD samples

that have been chemically treated to increase photocurrent, as will be discussed in

Chapter 5.

3.3.4 TOP contamination

Figure 3.7 shows optical microscopy and *i-V* data for Sample D. At first glance, it

appears that the sample preparation for Sample D should be identical to that of Sample C,

except that it uses QDs from a separate (although apparently identical) prep, and it is

(a)

100 μm

(b)

Figure 3.5: Sample B. (a) Optical microscopy image of a film from Sample B deposited on a glass slide. (b) Current-voltage curve measured for Sample B, taken at 77 K on a 2μm gap with an excitation intensity of ~ 1mW.

(a)

100 μm

(b)

Figure 3.6: Sample C. (a) Optical microscopy image of a film from Sample C deposited on a glass slide. (b) Current-voltage curve measured for Sample C, taken at 77 K on a 2μm gap with an excitation intensity of ~ 1mW.

even more thoroughly cleaned during size selection. However, while the film of Sample D in Figure 3.7(a) appears only slightly worse than the film of Sample C in Figure 3.6(a), the *i-V* curves in Figures 3.6(b) and 3.7(b) are clearly very different from each other. In fact, the photocurrent for Sample D at 250 V is more than 3000 fold less than the photocurrent for Sample C at the same voltage.

Unfortunately, it was concluded that the bottle of TOP used to synthesize the QDs for Samples A – D got contaminated, between the synthesis of the QDs for Samples C and D. A high level of photocurrent is recovered by keeping everything constant, except trying a different bottle (and, in this case, a different manufacturer) of TOP. Because TOP is very good at dissolving many compounds (including the type of rubber gloves that are used in the glove box), it seems that TOP contamination is facile. And clearly, as is seen in the photocurrent characteristics of Sample C versus Sample D, this contamination can have an enormous effect on the photoconductivity of QD films. Because of the nature of the problem, it is difficult to surmise what exactly contaminates the TOP and causes this problem. Suffice it to say, great care should always be taken in handling TOP to reduce (or, more preferably, eliminate) contamination.

3.3.5 TOP variation

As the last of the "magic" lot of TOP manufactured by Fluka (labeled lot 1 in Figure 3.1) became contaminated, it became necessary to find a new lot of TOP from Fluka, or a new manufacturer of TOP altogether. Unfortunately, there is an enormous degree of variation between different lots and manufacturers of TOP. Samples C, E, F, and G represent samples that are processed identically, except that they are synthesized
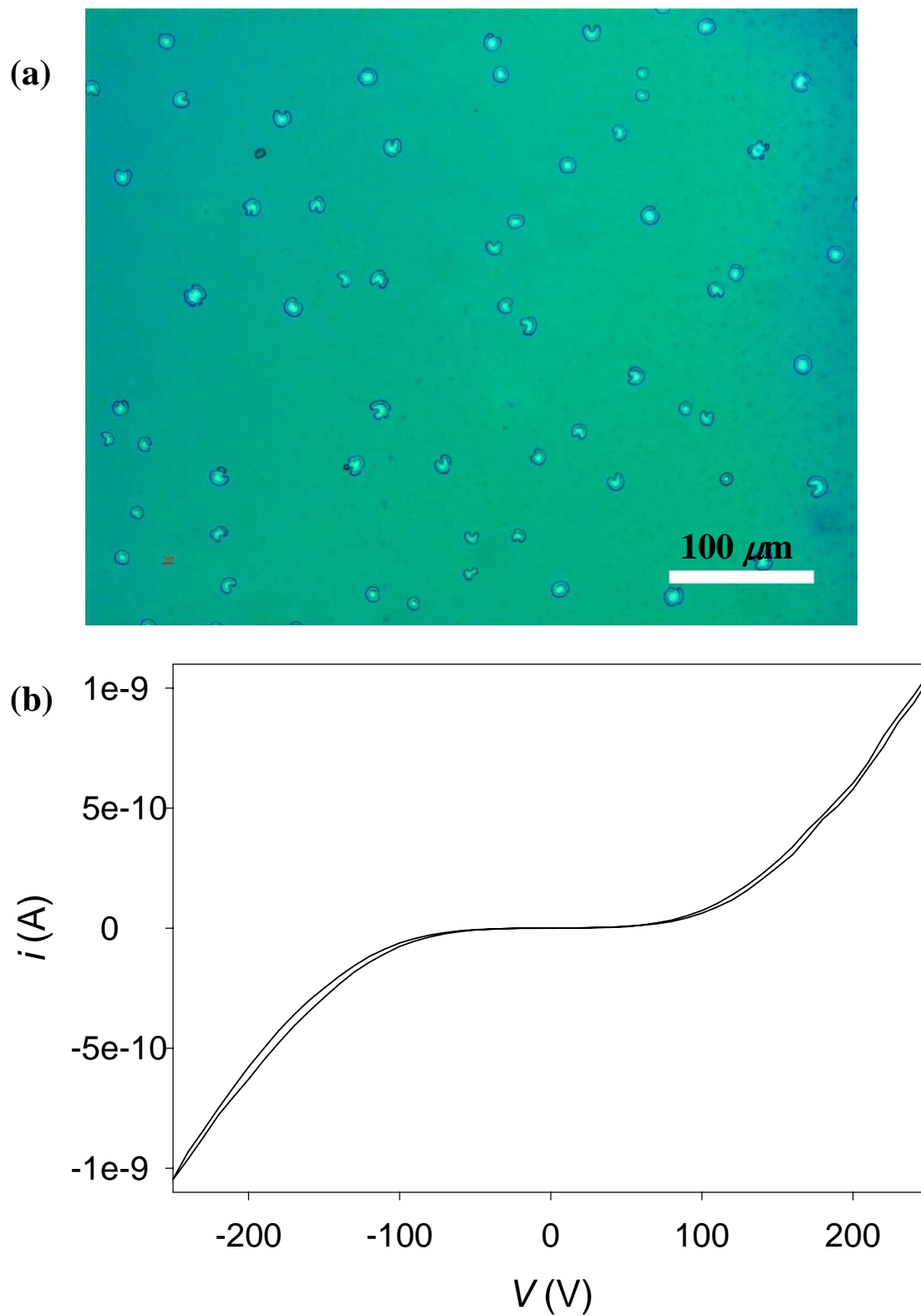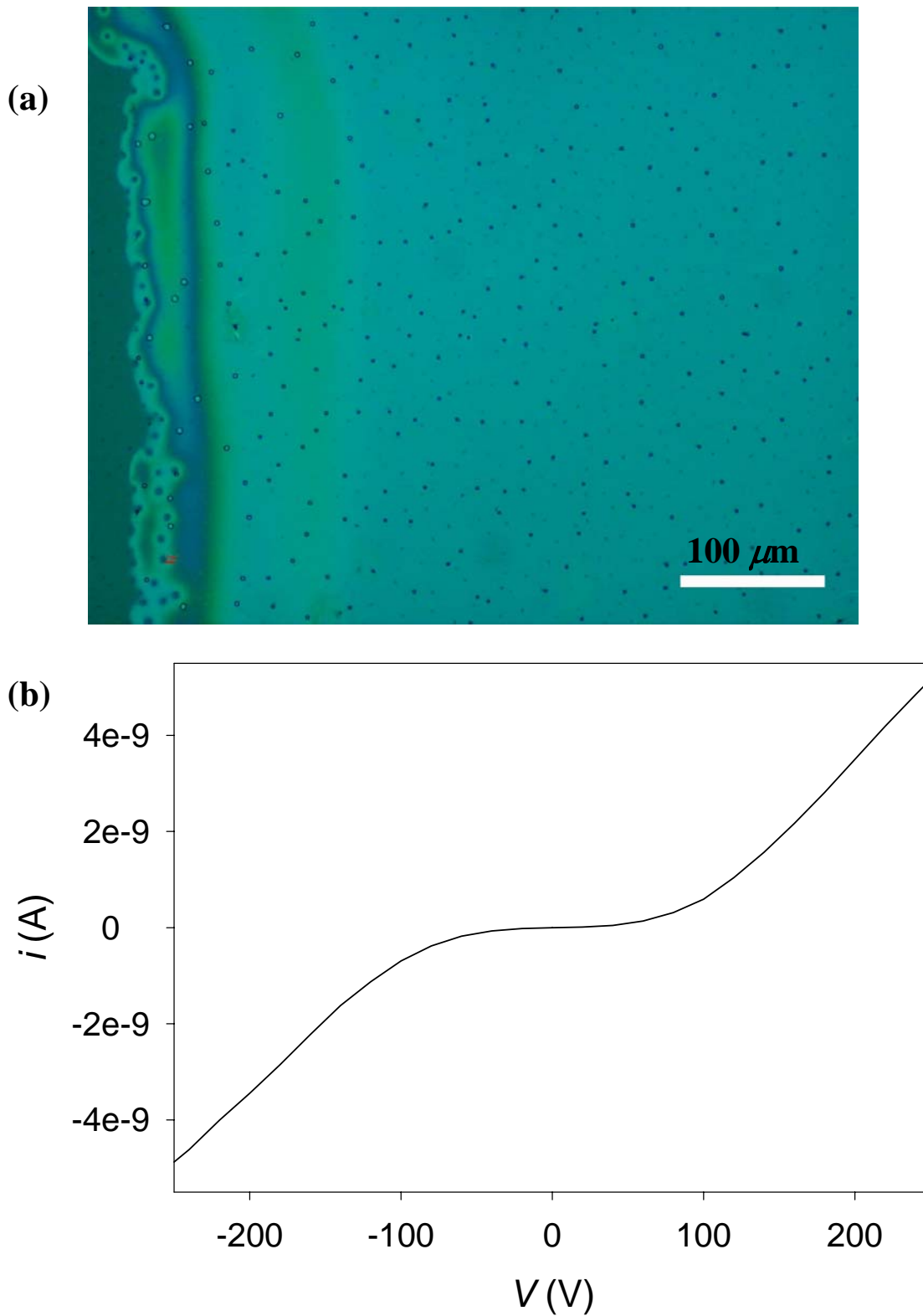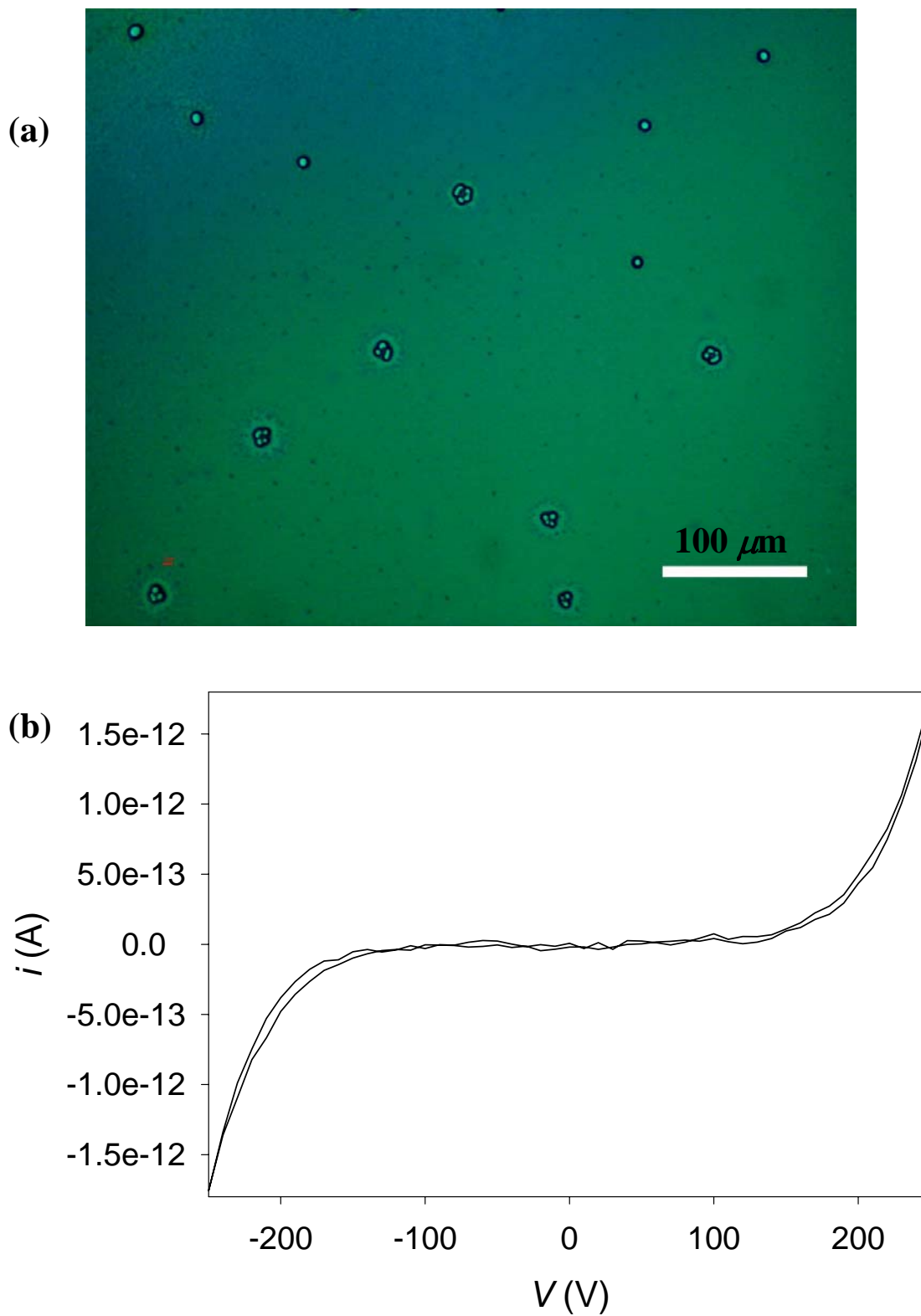
Figure 3.7: Sample D. (a) Optical microscopy image of a film from Sample D deposited on a glass slide. (b) Current-voltage curve measured for Sample D, taken at 77 K on a 2μm gap with an excitation intensity of ~ 1mW.

using four different bottles of TOP. Because of the clear effects of contamination, as

discussed in Section 3.3.4, newly opened bottles of TOP were tried if the

photoconductivity seemed poor; this did not have a significant effect, so it can be

concluded that the effects observed are truly due to TOP variations form lot to lot, and

from manufacturer to manufacturer.

For Sample C, which has already been discussed, TOP manufactured by Fluka

and labeled in Figure 3.1 as lot 1 is used. For Sample E, TOP from another lot (lot 2) of

TOP manufactured by Fluka is used. For Sample F, the TOP used to synthesize the QDs

is lot G02L25, manufactured by Alfa Aesar. For Sample G, the TOP used is lot I25L01,

also manufactured by Alfa Aesar. In all cases the TOP is reported by the manufacturer to

have a purity of 90%.

The optical microscopy and photocurrent data for Sample C are given in Figures

3.6(a) and 3.6(b), respectively. For Sample E, the corresponding data are given in

Figures 3.8(a) and (b); for Sample F, the corresponding data are shown in Figures 3.9(a)

and 3.9(b); for Sample G, the corresponding data are shown in Figures 3.10(a) and

3.10(b).

Samples C (Fluka, lot 1) and F (Alfa Aesar, lot G02L25) exhibit both high

photoconductivity (> 1 nA at 250 V), and clear, smooth films with no observable

contamination or particulate matter. In contrast, Samples F (Fluka, lot 2) and G (Alfa, lot

I25L01) exhibit $\sim 500 - 1000$ fold less photocurrent than Samples C and F, as well as

apparently lower quality films. The film for Sample G, in Figure 3.10(a), does appear

fairly clear and smooth, although it seems to have many small particulates, on the order

of $< \sim 5 - 10$ μm. Furthermore, as is indicated in Figure 3.1, the QDs used for Sample G

(a)

100 μm

(b)

i (A)

V (V)

Figure 3.8: Sample E. (a) Optical microscopy image of a film from Sample E deposited on a glass slide. (b) Current-voltage curve measured for Sample E, taken at 77 K on a 2 μm gap with an excitation intensity of ~ 1mW.

Figure 3.9: Sample F. (a) Optical microscopy image of a film from Sample F deposited on a glass slide. (b) Current-voltage curve measured for Sample F, taken at 77 K on a $2\,\mu m$ gap with an excitation intensity of $\sim 1mW$.

Figure 3.10: Sample G. (a) Optical microscopy image of a film from Sample G deposited on a glass slide. (b) Current-voltage curve measured for Sample G, taken at 77 K on a 2μm gap with an excitation intensity of $\sim$ 1mW.

also exhibit poor fluorescence (when in the growth solution). The film for Sample E, in

Figure 3.8(a), looks far worse, with contamination that resembles small crystallites on the

order of ~ 20 μm; these may be due to organic contamination crystallizing out of the film

as it dries.

3.3.6 TOP purification

While it has not been rigorously investigated, it is suspected that the

contamination in the 90% TOP leading to so much photocurrent and film variation

between different lots of TOP is likely due to dialklyl phosphines or acidic impurities in

the TOP (i.e., phosphonic or phosphinic acids). In order to eliminate the irreproducibility

of different lots of TOP, we purified the TOP used to synthesize the QDs of Sample G

(Alfa Aesar lot I25L01). The purification procedure, described in Section 3.2.2 and

illustrated in Figure 3.2, involves passing the TOP through a column of activated basic

alumina in an air-free manner.

Sample H uses QDs synthesized with TOP that is purified according to the

procedures of Section 3.2.2. As is indicated in Figure 3.1, the fluorescence of the QDs in

the growth solution used for Sample H is much better than for the QDs synthesized with

the same TOP prior to purification (used for Sample G). Figures 3.11(a) and 3.11(b)

show the optical microscopy and photocurrent data, respectively, for Sample H. The

photocurrent is clearly improved by a factor of 10 over Sample G. However, the

photocurrent is still an order of magnitude lower than that for Samples B and C. The

optical microscopy image of Sample H in Figure 3.11(a) seems to reveal the reason for

this: the film is definitely not as smooth, clear, and free of contamination as the films of

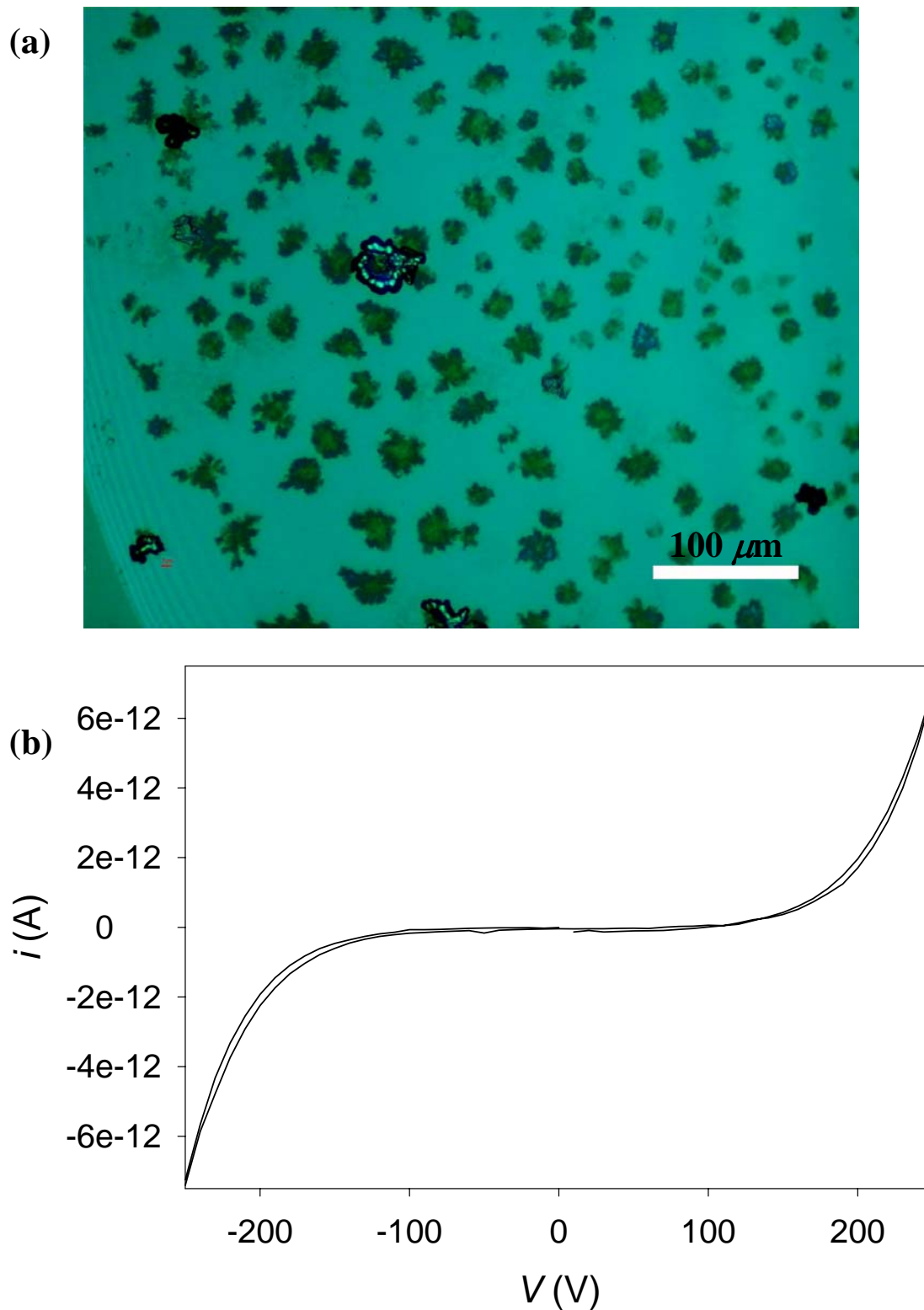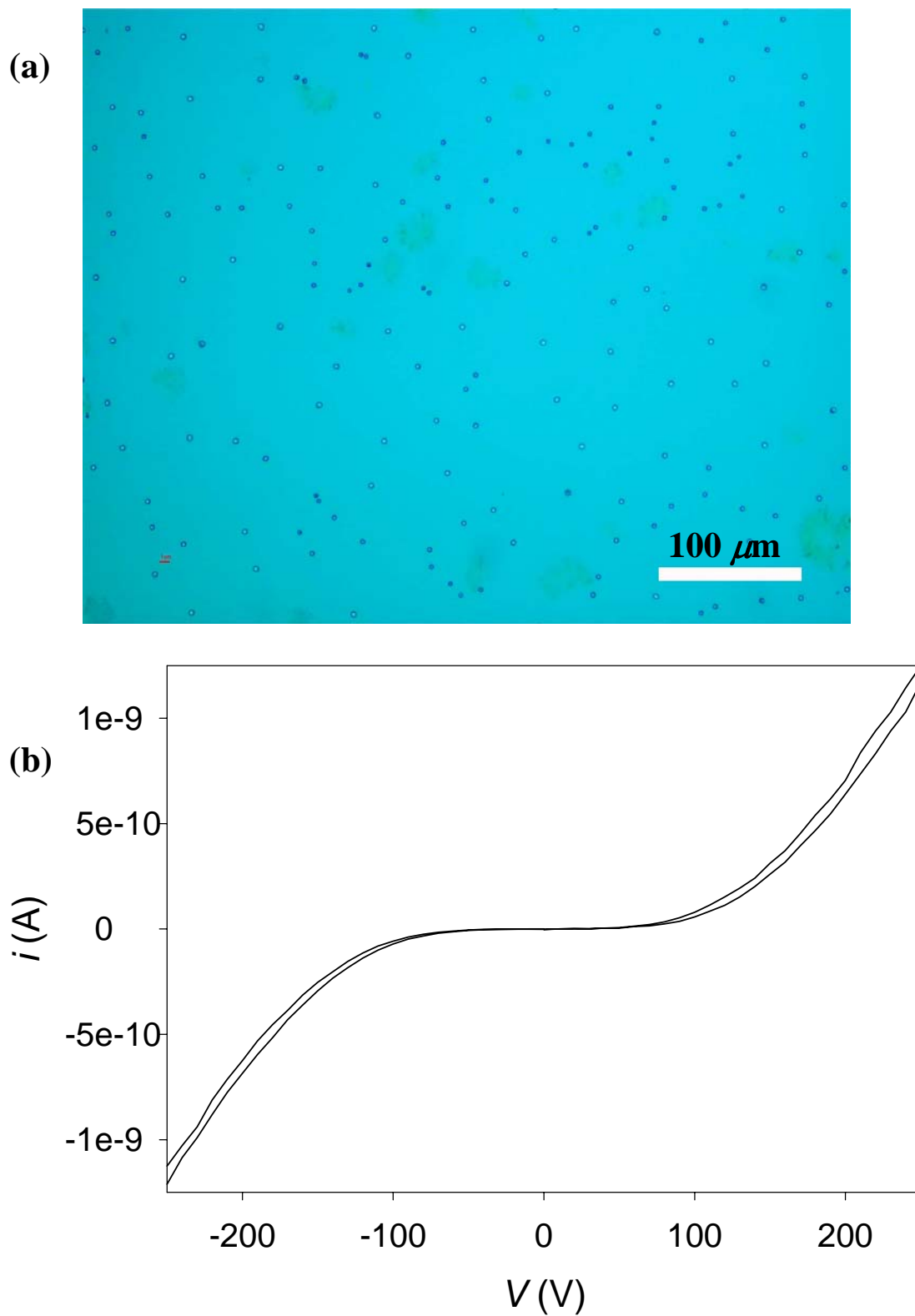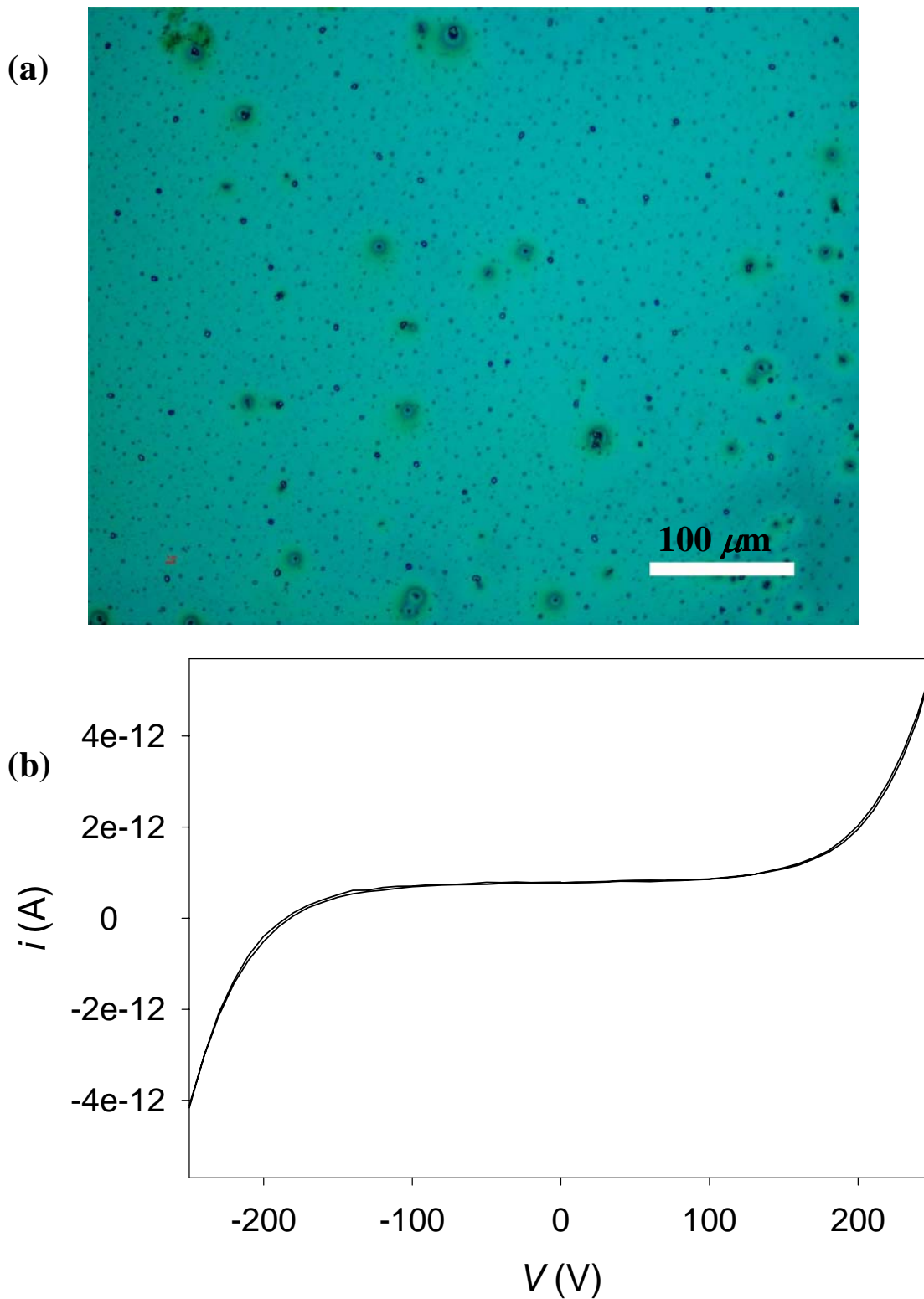96

(a)

250 μm

(b)
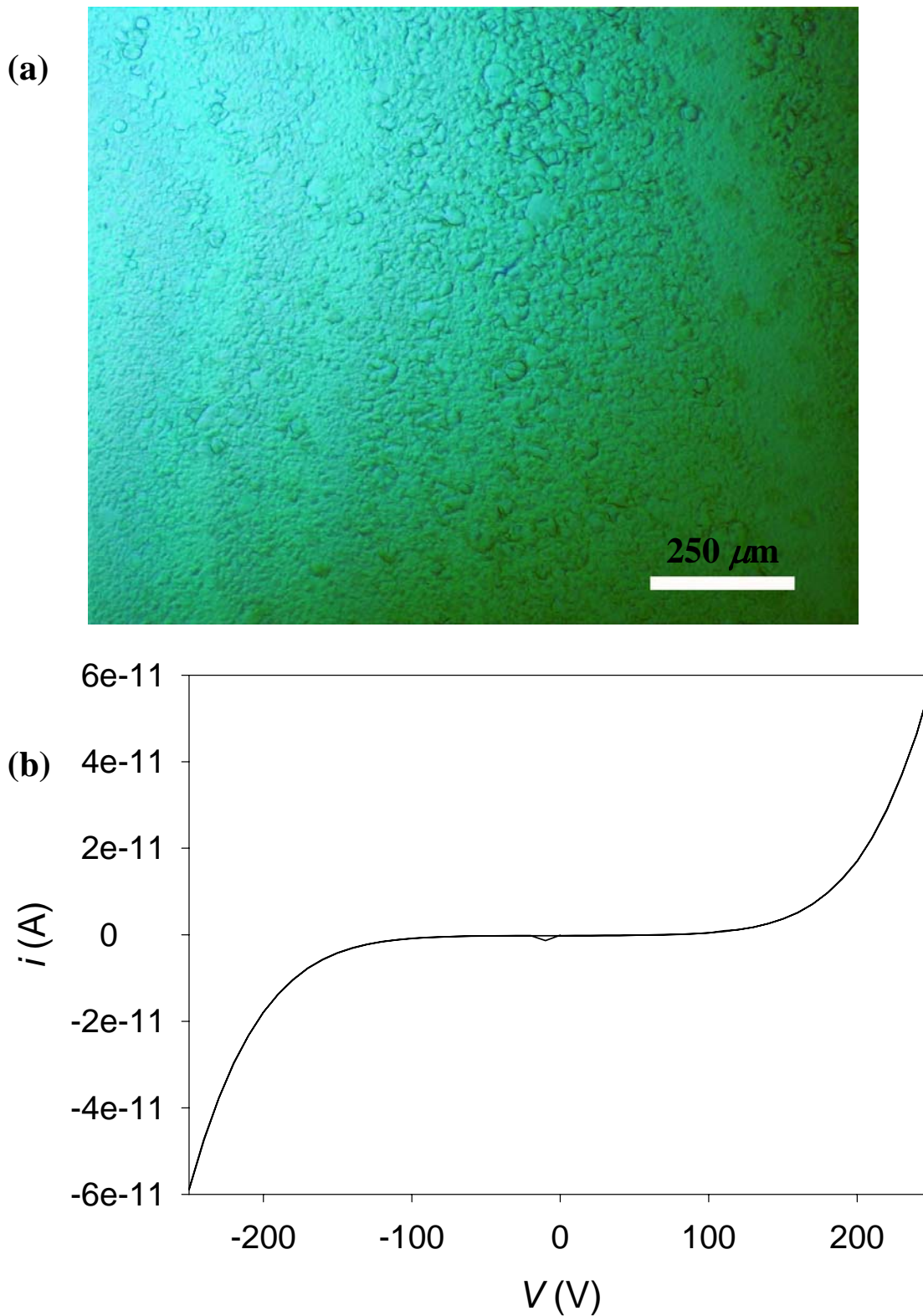
Figure 3.11: Sample H. (a) Optical microscopy image of a film from Sample H deposited on a glass slide. (b) Current-voltage curve measured for Sample H, taken at 77 K on a 2μm gap with an excitation intensity of ~ 1mW.

Samples A, B, C, or F. In fact, the film appears substantially cloudier than the film of

Sample G (synthesized with the same TOP prior to purification).

Figure 3.12 shows optical microscopy images of a sample that is prepared in a

similar manner to Sample H. It appears that some different material is present in the QD

film, and in places seems to be precipitating out of or phase separating from the QD film.

These images are a strong clue that samples using QDs synthesized with the purified TOP

exhibit lower photoconductivity due to contaminants in the film. Figure 3.13 is an

additional clue pointing to the same conclusion. Figure 3.13(a) shows an AFM

topography image of the sample film of QDs shown in Figure 3.12. There is a substantial

degree of roughness in the film. Figure 3.13(b) shows the phase image that corresponds

to the topography image in Figure 3.13(a). The phase image is sensitive to what kind

material is beneath the tip (as a "stickier" material will interact more with the tip than a

harder material), so the phase image in Figure 3.13(b) indicates that there are two

different materials in the film. The image is strongly suggestive of a different (probably

organic) material crystallizing on top of the QD film.

3.3.7 Improving QD film quality

In order to improve the photoconductivity of QDs synthesized with the purified

TOP, it appears that it is necessary to further clean the QD samples during the size

selection and film deposition processes. We developed a procedure that is designed to

get rid of as much extra organic from the QD sample as possible. For Sample I, QDs are

synthesized with purified TOP. Prior to adding butanol to the growth solution, the QD

sample is placed in the freezer for ~ 15 minutes to encourage precipitation of salts and

(a)

100 μm

(b)

50 μm
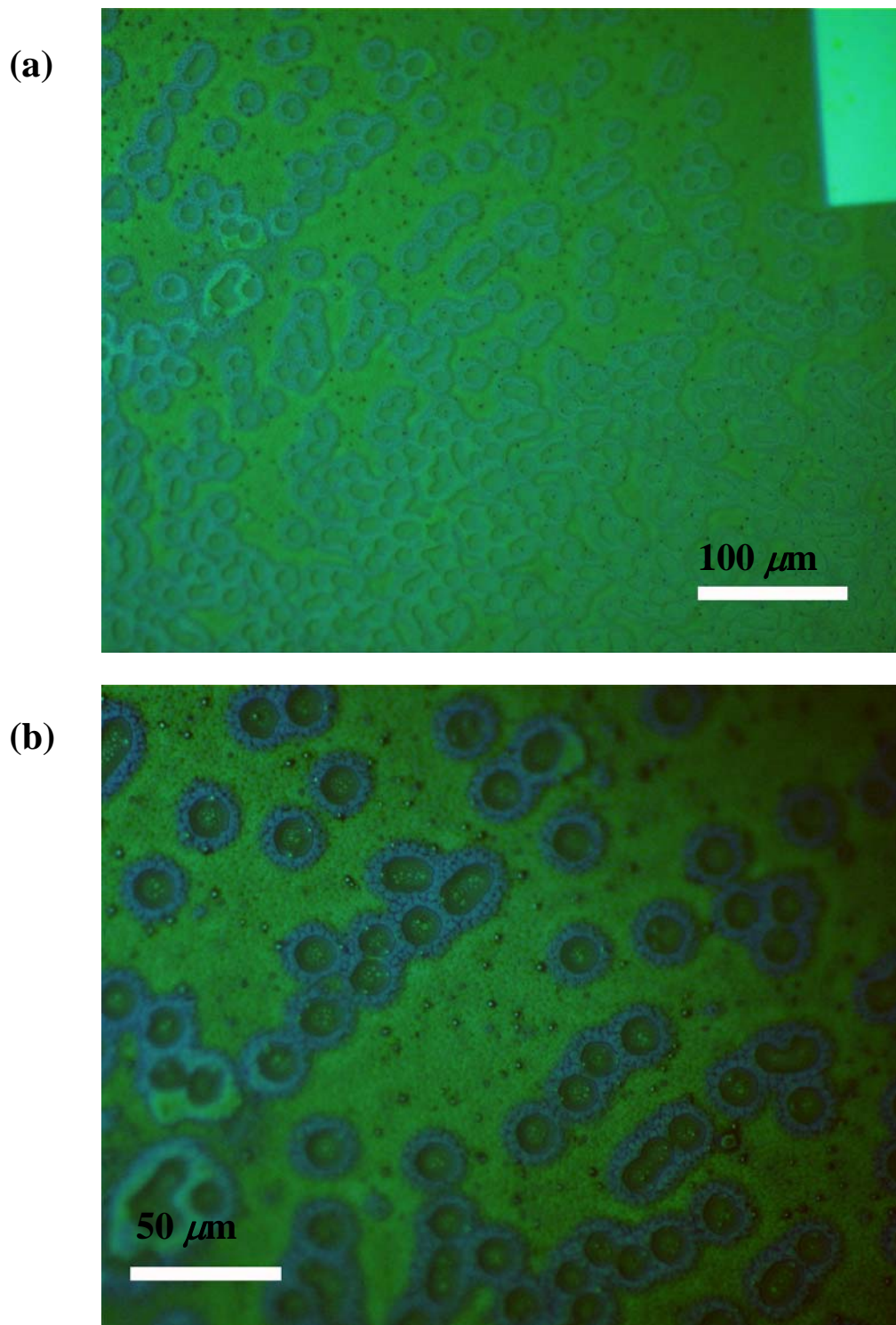
Figure 3.12: Optical microscopy image of a film of QDs deposited on a quartz electrical device, at lower (a) and higher (b) magnifications. The sample used to deposit this film was prepared in a similar manner to sample H, and served as a strong clue that contaminants in the film were likely responsible for the lower level of photoconductivity being observed.

(a)

(b)
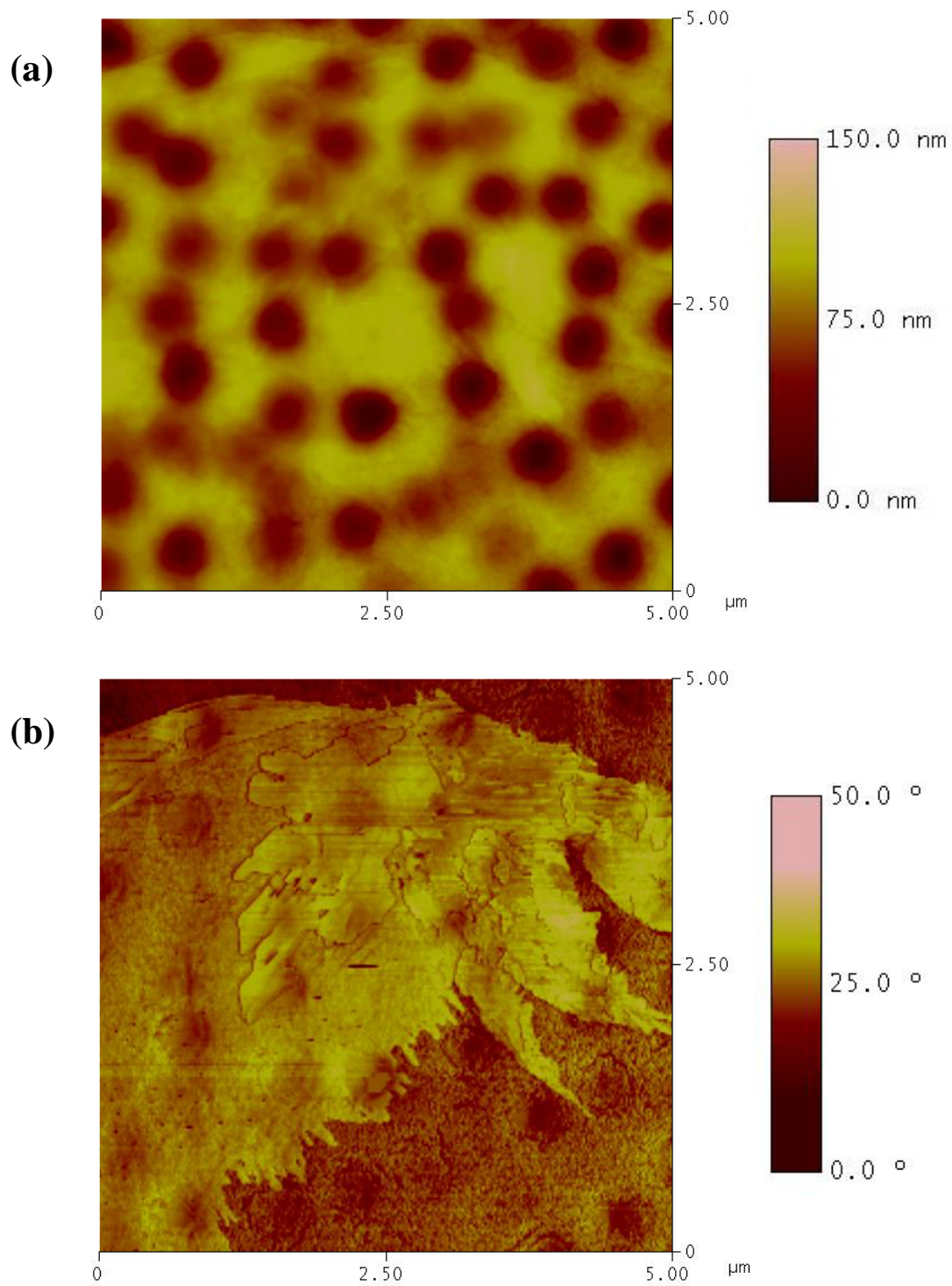
Figure 3.13: Atomic force microscopy (AFM) of a film of QDs deposited on a glass slide. The sample used to deposit this film was prepared in a similar manner to sample H, using the same QDs used for the sample shown in Figure 3.12. (a) is the topography data, taken during the forward scan, and (b) is the phase image, taken simultaneously during the reverse scan.

less soluble organics. The QD sample is then centrifuged, as for Samples A – H. After centrifugation, much more precipitate is present in Sample I than in the samples that are not placed in the freezer prior to centrifugation.

Another change for Sample I is that the QDs are filtered from the hexane and butanol solution prior to both the second and the third size selection steps. For these filtration steps, a 0.2 μm and a 0.1 μm PTFE syringe filter, respectively, are used. The final change (with respect to Sample H) is that the final filtration step from the 9:1 hexane: octane solution uses a 0.02 μm aluminum oxide syringe filter, rather than a 0.2 μm PTFE syringe filter.

Figures 3.14(a) and 3.14(b) show the optical microscopy and photocurrent data, respectively, for Sample I. In comparison to Sample H, the film seems far smoother, clearer, and free of contamination. Correspondingly, the photocurrent is 10 fold higher than the photocurrent for Sample H, and 100 fold higher than the photocurrent for Sample G (using QD synthesized with the same Alfa Aesar TOP prior to purification). The combination of purifying the TOP and rigorously cleaning the QDs prior to film deposition successfully brings the photocurrent back up near the levels of Samples B, C, and F.

3.4 Conclusion and summary of modified procedures

A comparison of the optical microscopy images and *i-V* curves for Samples A – I clearly shows how exquisitely sensitive photoconductivity measurements are to the quality of QDs, as well as the quality of QD films. Due to the pyrophoric and toxic nature of dimethylcadmium, it is highly desirable to be able to use CdSe QDs synthesized

(a)

(b)
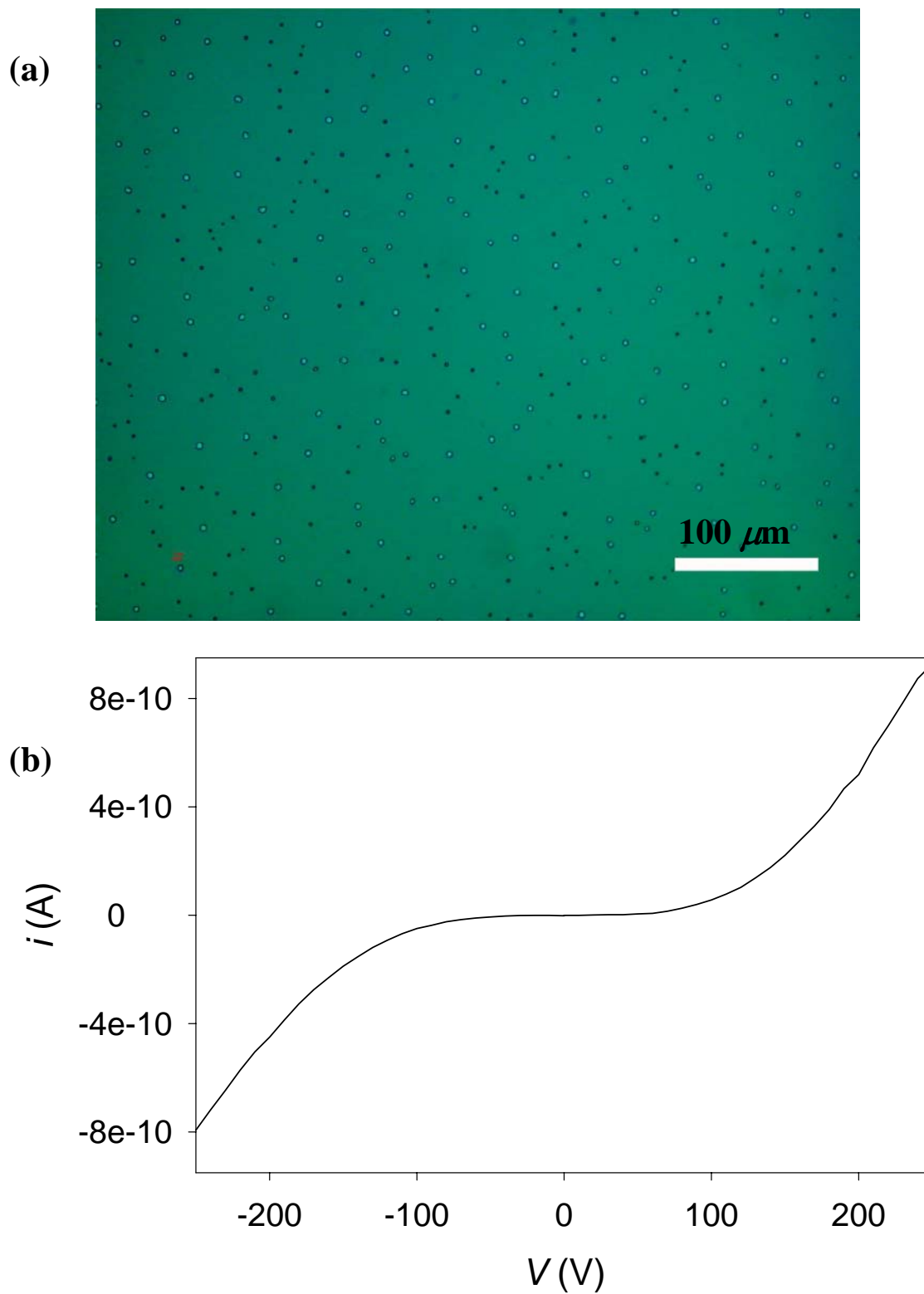
Figure 3.14: Sample I. (a) Optical microscopy image of a film from Sample I deposited on a glass slide. (b) Current-voltage curve measured for Sample I, taken at 77 K on a 2μm gap with an excitation intensity of ~ 1mW.

102

from a cadmium salt, such as Cd(acac)$_2$, for photoconductivity devices. The prep developed by N. E. Stott[1] using Cd(acac)$_2$ also has the additional benefit of being able to use 99% TOPO, which is not possible with the dimethylcadmium-based prep.

We have shown that, in order to be able to use the Cd(acac)$_2$- based prep for photoconductivity measurements, great care must be taken to thoroughly clean the QDs of all excess organics that are present in the growth solution. Furthermore, the magnitude of the photocurrent measured from a QD sample depends strongly on which lot and manufacturer of 90% TOP is used to synthesize the QDs. In addition, it is unfortunately found that TOP is easily contaminated, and that such contamination can decrease the magnitude of measured photocurrent by more than a factor of 3000. While the source of the contamination was never tracked down, the irreproducibility between lots of TOP can be minimized by purifying the TOP through a column of activated basic alumina. Using purified TOP also seems to decrease the quality of the QD films. However, nice films and high levels of photoconductivity can be regained by cleaning the QD samples even more rigorously prior to film deposition.

In summary, the following procedure was shown to purify TOP and clean QD samples sufficiently for the observation of high levels of photoconductivity:

For TOP purification, 50 mL of TOP is passed through a column containing 10 g of activated basic alumina in an air-free manner. This TOP is used to synthesize CdSe QDs using Cd(acac)$_2$, as outline is Section 3.2.1 and developed be N. E. Stott.[1] 5 mL of hexane is added to the QD growth solution to keep the sample from solidifying at room temperature. In order to make QD films, a 5 mL aliquot is taken from the hexane/growth solution mixture.

Another ~ 2 – 3 mL of hexane is added to this aliquot, in order to keep it from solidifying as it is put in the freezer for ~ 15 minutes. The sample is then centrifuged for 5 minutes at 3900 rpm, and the precipitate is discarded (along with any dots that become trapped in the precipitate).

~ 5 mL of butanol is added to the supernatant, and the QDs are precipitated with methanol to ~ 1 mL past the endpoint. After centrifugation, the supernatant (which, as for all three precipitation steps, should have color remaining) is discarded, and the precipitate is dissolved in ~ 3 mL of hexane and ~ 3 mL of butanol. This solution is filtered through a 0.2 μm PTFE syringe filter, and then a second precipitation with methanol is carried out (this time going past the endpoint by ~ 10 drops). The sample is centrifuged, and the supernatant is again discarded. The precipitate is dissolved in ~ 2 mL hexane and ~ 2 mL butanol, and filtered through a 0.1 μm PTFE syringe filter. A final precipitation with methanol is performed, going ~ 10 drops past the endpoint again. After centrifugation and discarding of the supernatant, the precipitate is dissolved in anhydrous hexane and dried under vacuum.

The dried QDs are dissolved in ~ 1 mL 9:1 hexane: octane, and then this solution is filtered through a 0.02 μm aluminum oxide syringe filter. After drying the QD solution under vacuum, the sample is brought under argon into an inert atmosphere glove box. The QDs are dissolved again in 9:1 hexane: octane in order to make a concentrated solution which is drop-cast onto the device of interest.

3.5 References

1.   M. Bawendi and N. E. Stott, "Preparation of nanocrystallites from metal-containing salts," U.S. Patent Number 2002071952 (June 13 2002).
2.   C. B. Murray, C. R. Kagan, and M. G. Bawendi, "Synthesis and characterization of monodisperse nanocrystals and close-packed nanocrystal assemblies," Annual Review of Materials Science **30**, 545-610 (2000).
3.   C. B. Murray, D. J. Norris, and M. G. Bawendi, "Synthesis and characterization of nearly monodisperse CdE (E = S, Se, Te) semiconductor nanocrystallites," Journal of the American Chemical Society **115**(19), 8706-8715 (1993).
4.   M. V. Jarosz, N. E. Stott, M. Drndic, N. Y. Morgan, M. A. Kastner, and M. G. Bawendi, "Observation of bimolecular carrier recombination dynamics in close-packed films of colloidal CdSe nanocrystals," Journal of Physical Chemistry B **107**(46), 12585-12588 (2003).
5.   C. Kagan, "The Electronic and Optical Properties of Close Packed Cadmium Selenide Quantum Dot Solids," (Ph.D. Thesis, Massachusetts Institute of Technology, Cambridge, MA, 1996).
6.   C. B. Murray, C. R. Kagan, and M. G. Bawendi, "Self-Organization of Cdse Nanocrystallites into 3-Dimensional Quantum-Dot Superlattices," Science **270**(5240), 1335-1338 (1995).
7.   C. R. Kagan, C. B. Murray, and M. G. Bawendi, "Long-range resonance transfer of electronic excitations in close-packed CdSe quantum-dot solids," Physical Review B **54**(12), 8633-8643 (1996).
8.   C. R. Kagan, C. B. Murray, M. Nirmal, and M. G. Bawendi, "Electronic energy transfer in CdSe quantum dot solids," Physical Review Letters **76**(9), 1517-1520 (1996).
9.   C. A. Leatherdale, C. R. Kagan, N. Y. Morgan, S. A. Empedocles, M. A. Kastner, and M. G. Bawendi, "Photoconductivity in CdSe quantum dot solids," Physical Review B **62**(4), 2669-2680 (2000).

Chapter 4

Observation of bimolecular carrier recombination dynamics[*]

4.1 Introduction

It has become increasingly apparent that photoionization and charging play an important role in the optical properties of quantum dots (QDs).[1-3] There have been many recent studies probing the electrical properties of semiconductor QDs,[2-14] as well as demonstrations of the application of these electrical properties to devices such as light emitting diodes[15-17] and photovoltaic devices.[18-20] In order to realize the full potential of semiconductor QDs, and to better comprehend their opto-electronic properties, it is essential to understand the details of their electrical properties. Photoconductivity is a good method for such a study, as it provides information about photoionization, charge transport, and charge carrier recombination.

We present a study of the intensity-dependent photoconduction of close-packed films of CdSe QDs. We show that it is possible to observe photoconduction that is characterized by a low density of trapped charges, in contrast to previous studies. Furthermore, we provide insight into the recombination processes in these films by fitting current vs. intensity plots to the steady state solution of the kinetic equations governing carrier density, which enables us to extract the ratio of carriers to trapped charges. We confirm our physical model of the recombination processes by demonstrating that we can

---

change the shape of the current vs. intensity plots as predicted by our model: we can

make the plots more linear by decreasing the charge density through decreasing the

applied voltage, or by increasing the density of trapped charges through slow aging of the

sample.

4.2 Experimental

4.2.1 Sample Preparation

The quartz substrates used for the photoconductivity measurements are

photolithographically patterned with gold electrodes (heights and lengths of 0.11μm and

800μm, respectively). The electrodes used for these experiments are separated by 1μm

and they are electrically contacted prior to film deposition.

According to the methods of Stott et al.,[21] TOPO/TOP-capped CdSe QDs with a

diameter of 47 Å are synthesized by rapid injection of cadmium 2,4-pentanedionate

(98%), tri-*n*-octylphosphine (TOP, 90%), 1,2-hexadecanediol (HDDO, 90%), and tri-*n*-

octylphosphine selenide (TOPSe, from 1.5M stock solution) into a hot solvent consisting

of TOP, tri-*n*-octylphosphine oxide (TOPO, 99%), and 1-hexadecylamine (HDA, 90%).

The absorption spectrum after this step for the quantum dots used for these experiments is

shown in Figure 4.1. After the growth solution has cooled to 80 ^{o}C, hexane is added to

prevent solidification once the sample cools to room temperature. The solution is then

placed in the refrigerator for one hour and then centrifuged to remove excess insoluble

organics and any salts that may have formed during the reaction. A precipitation using

butanol and hexane as the solvents and methanol as the nonsolvent is repeated three times

in order to remove excess TOPO/TOP which would prohibit close-packing of the QD
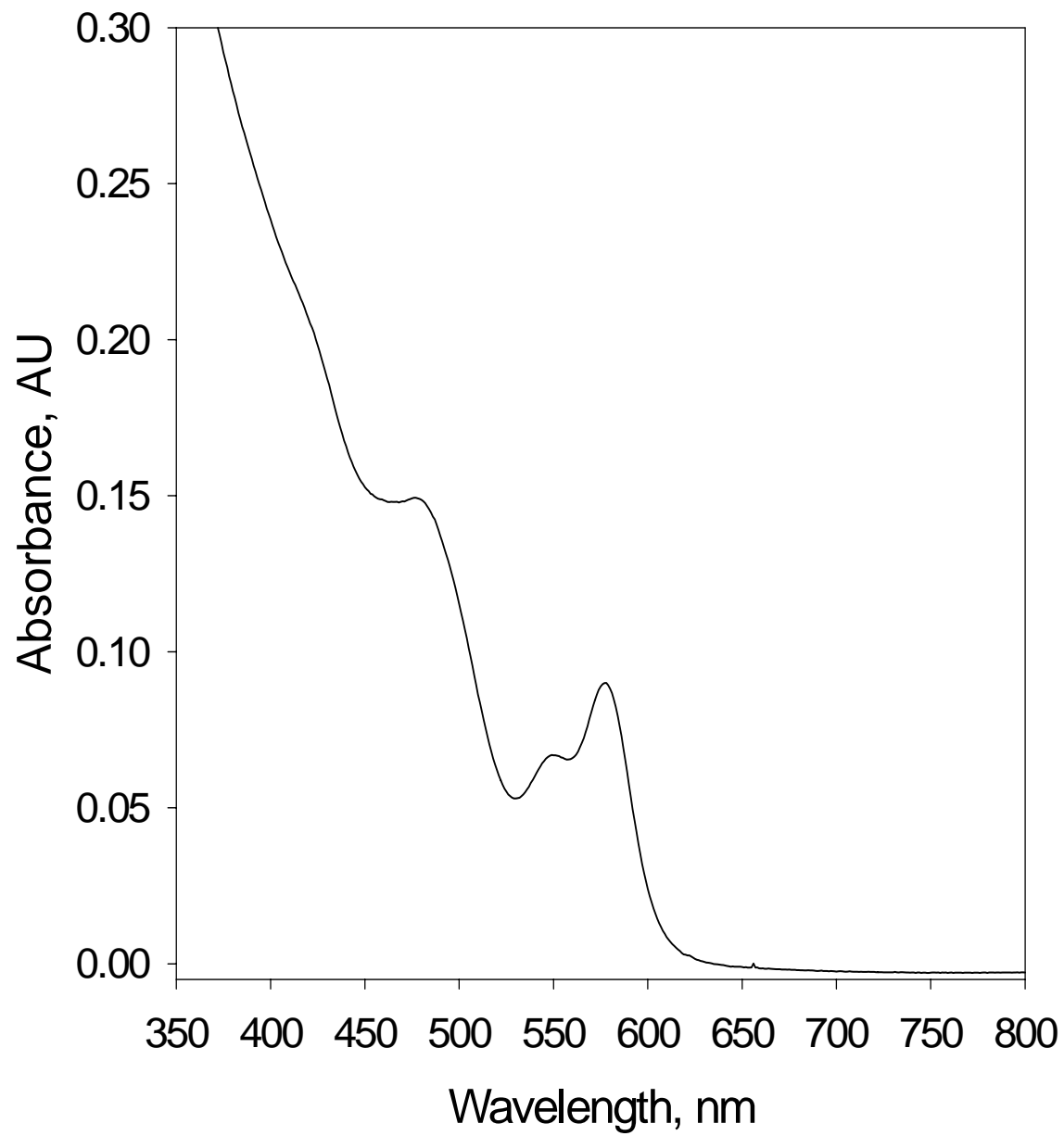
Figure 4.1: Absorption spectrum of the quantum dots used in these studies.

film.[10, 22, 23] The precipitations also have the effect of narrowing the size distribution. The hexane/butanol/QD solution is filtered prior to the second and third precipitation using 0.2 μm and 0.1 μm syringe filters, respectively, in order to further remove excess insoluble organics and salts. According to previously established methods for making close-packed CdSe QD films,[10, 23-26] the final precipitate is dried under vacuum and redissolved in a 9:1 mixture of hexane: octane; this solution is filtered through a 0.02 μm syringe filter. The close-packed films are deposited in an inert atmosphere by drop-casting the QD solution onto the prepared quartz substrates.[27] Analysis of close-packed regions of QDs in transmission electron microscopy (TEM) images indicates that the QDs are separated by 1.2 ± 0.4 nm, consistent with previous studies.[25] A low-resolution TEM image illustrating the tendency for the QDs to close-pack and a representative high-resolution TEM image confirming the spherical and crystalline nature of the QDs are shown in Figures 4.2(a) and 4.2(b), respectively.

4.2.2 Measurements

The measurement device is shown in the inset of Figure 4.3. The measurements are performed at 77 K under vacuum in a cold-finger cryostat. The samples are loaded into the cryostat inside of an inert atmosphere glove box and the cryostat is subsequently evacuated to $< 10^{-5}$ Torr so that contact with air is minimized. A Keithley 6517 electrometer is used to measure current as well as to apply a source-drain voltage. The 514 nm line of an Ar^{+} laser is used as the excitation source, with excitation intensities up to 25 mW/cm^2. A neutral density filter wheel is used to adjust the excitation intensity for intensity dependent measurements. Previous work by Leatherdale et al.[10] on the

110

(a)

10 nm
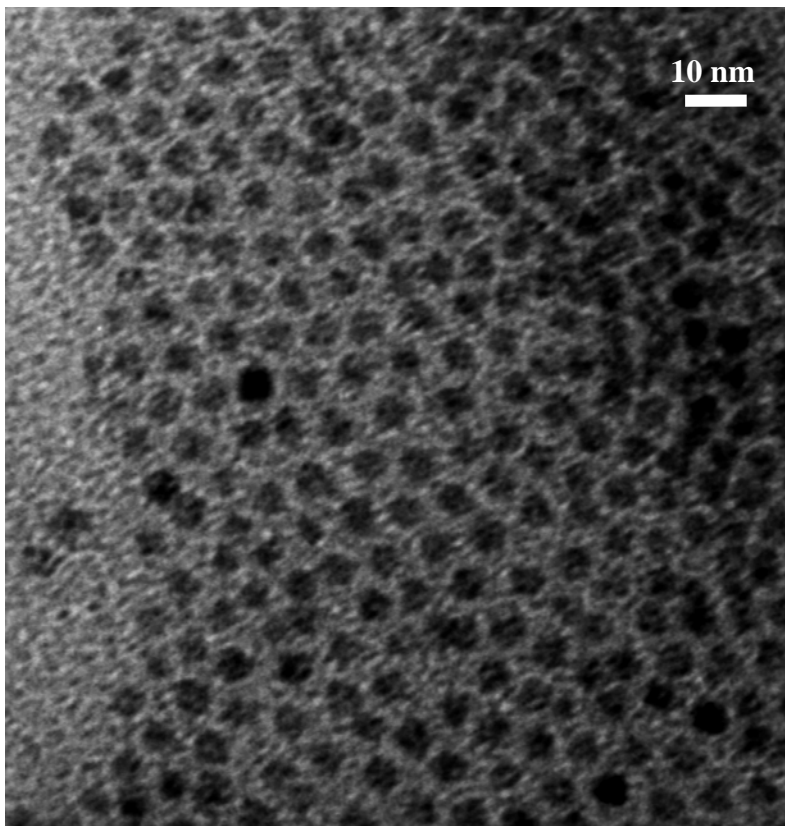
(b)
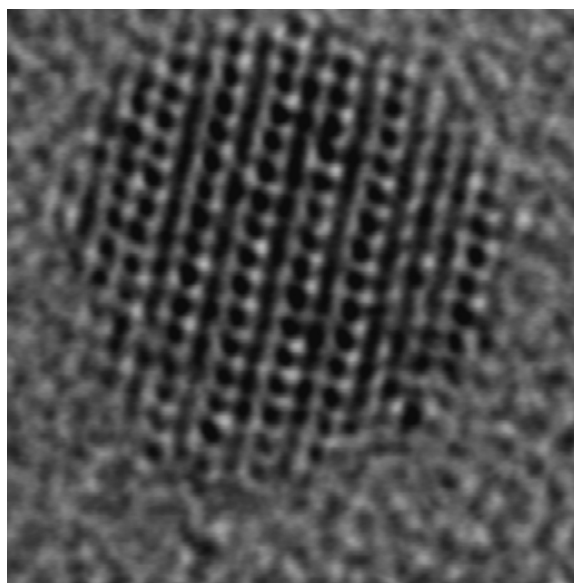
Figure 4.2: (a) Low-resolution TEM image showing the close-packed nature of CdSe QD films. This sample of 5.7nm diameter CdSe QDs is prepared in the same way as those measured in the photoconductivity studies, except that the film is deposited from a more dilute solution in order to be visible with TEM. (b) High-resolution TEM image of one QD from the same sample of QDs seen in (a), confirming the spherical and crystalline nature of the QDs.

photoconductivity of close-packed films of CdSe quantum dots confirms that the

photoconduction is field dependent, that it results from the field-induced separation of

excitons, and that it is not due to photoinjection from the gold electrodes.

4.3 Results and Discussion

4.3.1 Model for intensity dependence

We base our physical model for the intensity dependence of the photocurrent on

well-established equations for charge carrier kinetics, starting with the equation for the

rate of change of the carrier density (n, which is linearly related to the current)

$$\frac{dn}{dt} = G - (N_t + n)nb \tag{4.1}$$

where G is the rate of photogeneration of carriers and is linearly related to the intensity,

N_t is the density of trapped charges, and b is a normalized factor for recombination

efficiency.[28] It is assumed that electrons are the majority carrier,[10] and that they must

recombine with a hole in order to be removed; the rate of annihilation is represented by

the negative term of Equation (4.1). The term ($N_t + n$) represents the total density of

holes available for recombination. There are at least n holes, as each carrier originates

from the separation of the electron and hole in the photo-generated exciton. In addition,

there are N_t trapped holes in the film that do not have a carrier electron as their counter-

charge – that is, for charge neutrality these trapped holes must be associated with an

electron that is trapped deep enough that it cannot contribute to conductivity. The most

likely scenario is that the trapped holes are in surface state traps such as unpassivated

selenium, and the trapped electrons reside either in the surface ligands (for instance, in an

acidic impurity such as those always present in TOP) or in radical species such as SeO_2^-

or O_2^-.[29] We deduce that SeO_2^- is a likely possibility since it is known that SeO_2 is

formed on the surface of oxidized CdSe nanocrystals,[30] and since SeO_2 is often used as an

oxidizing agent,[31] it is likely that the reduced form, SeO_2^-, could be present on the surface

of the nanocrystals.

At equilibrium, the steady-state approximation may be used so that Equation (4.1)

becomes

$$G = (N_t + n)nb \qquad (4.2)$$

If the density of trapped charges is much larger than the carrier density, Equation (4.2)

reduces to

$$G \approx N_t nb, \qquad (4.3)$$

which results in a linear relationship between current and intensity. If, on the other hand,

the carrier density is much larger than the density of trapped charges, Equation (4.2)

reduces to

$$G = n^2 b, \qquad (4.4)$$

which results in the current having a square root dependence on the intensity.

4.3.2 Nonlinear intensity dependence is observed

Figure 4.3 shows a typical graph of current vs. intensity. The measurement is

taken with an applied field of 10^6 V/cm.   As Figure 4.3 shows, a nonlinear intensity

dependence is observed, suggesting that the density of trapped charges in this system is

not much larger than the carrier density, and the recombination is best described as

bimolecular. This is in contrast to previous work[10] that shows a linear intensity

dependence of the photocurrent. The linear intensity dependence in that case is attributed
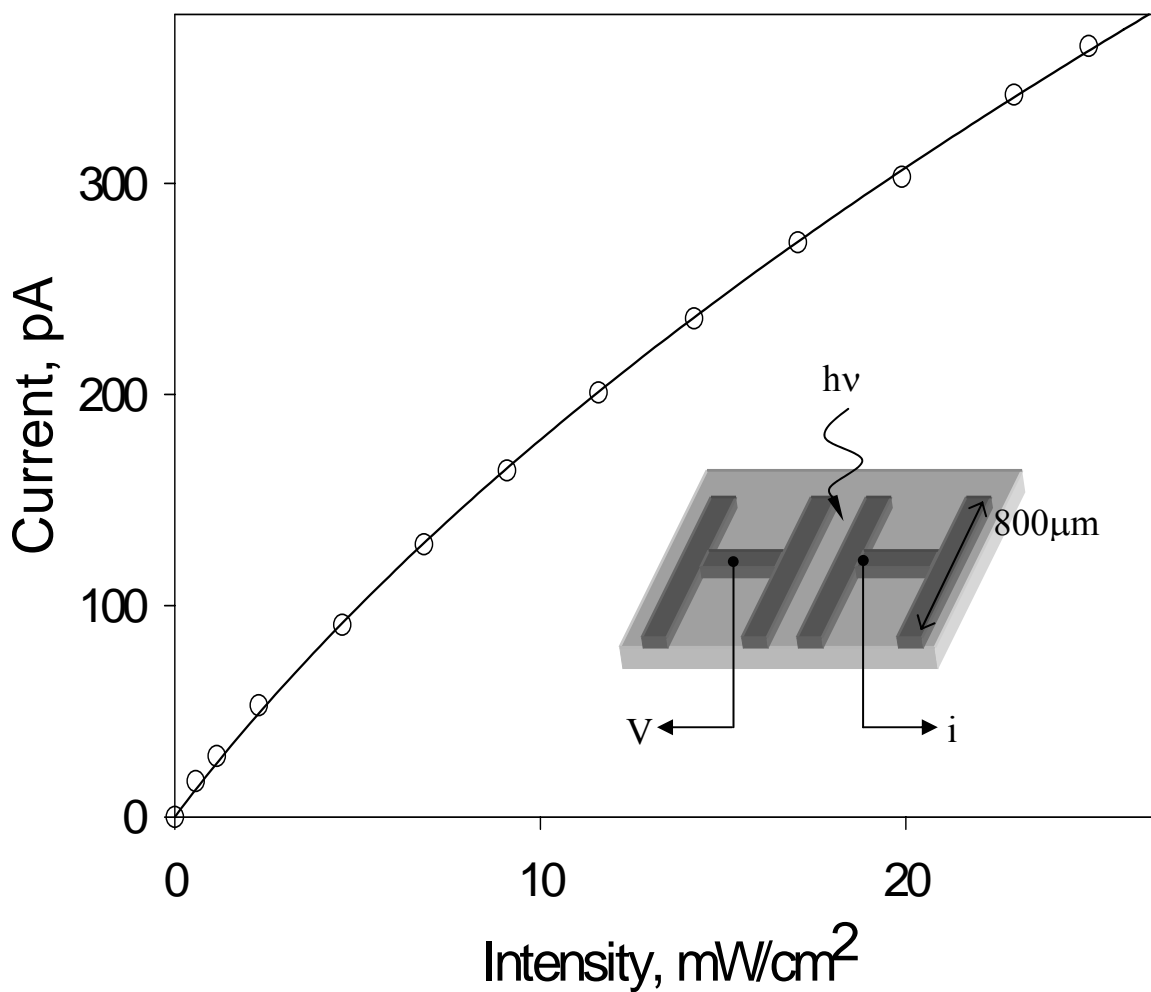
Figure 4.3: Representative graph of current vs. intensity. The circles correspond to the data, and the solid line corresponds to the fit to Equation (4.11). The extracted ratio of n/N_t at the highest measured intensity is ~0.6. The inset shows the measurement device. The substrate is quartz, and the electrodes are 1000 Å of gold on top of 100 Å of titanium. The length of the electrodes is 800 μm and they are separated by 1 μm. The sample is illuminated with 514 nm light from an Ar$^+$ laser.

to pseudo-monomolecular recombination, meaning that the density of trapped charges is much larger than the carrier density, and thus the recombination is described by Equation (4.3). We suggest that the films we measure here have a lower density of trapped charges, because of the different methods used to synthesize the QDs and because the exposure to air has been minimized.

4.3.3 Fits to the data

For further analysis of Equation (4.2), it is necessary to rewrite the equation in terms of the parameters that are measured in the experiment: current (i) and intensity (I). Since the parameters G and n are linearly related to I and i, respectively, we make the following substitutions:

$$I \cdot m(V) = G \tag{4.5}$$

and

$$i \cdot a(V) = n. \tag{4.6}$$

where $m(V)$ is a voltage dependent parameter that incorporates the voltage-dependent exciton separation efficiency and the absorption cross-section of the film. $a(V)$ is a voltage dependent parameter, with

$$a(V) = L/(AVe\mu), \tag{7}$$

where L is the length of the electrodes, A is the area of the side of the electrodes in contact with the film, and μ is the mobility. The equation for $a(V)$ is derived from the relationship between conductivity (σ) and n:

$$\sigma = \frac{iL}{AV} = ne\mu . \tag{4.8}$$

These substitutions result in a quadratic equation relating current and intensity (for all values of i and N_t). Because there are only two independent parameters in Equation (4.3), we define

$$\alpha = (\frac{b}{m}a^2) \tag{4.9}$$

and

$$\beta = (\frac{b}{m}N_t a) \tag{4.10}$$

The intensity dependence of the current then becomes:

$$i = \frac{1}{2\alpha}\left(-\beta + \sqrt{\beta^2 + 4\alpha I}\right) \tag{4.11}$$

Equation (4.11) is used to fit the current vs. intensity data, with α and β as the fitting parameters. Figure 4.3 shows an example of the fit for some representative data.

It is possible with further manipulation of the above equations to extract additional information from the fit parameters. Given Equation (4.6) and that

$$\frac{\alpha}{\beta} = \frac{a}{N_t} \quad , \tag{4.12}$$

it is possible to extract the ratio of carriers to trapped charges at a particular intensity:

$$\frac{n}{N_t} = \frac{\alpha}{\beta}i \quad . \tag{4.13}$$

For the data in Figure 4.3, $\frac{n}{N_t}$ ~0.6 at the highest measured intensity value, which confirms that in this case the trap density and the carrier density are of comparable magnitudes.

116

Table 4.1: Voltage dependence of n/N_t at the highest measured intensity for the data in Figure 4.4.

Field, V/cm	n/N_t at highest I
5×10^4	0.17
3×10^5	0.34
1.3×10^6	0.68

Table 4.2: Oxidation dependence of n/N_t at the highest measured intensity for the data in Figure 4.5.

Day #	n/N_t at highest I
1	3.8
5	0.58
12	0.34

4.3.4 Changing the shape of *i* vs. *I*

Because the deviation from linearity in the *i* vs. *I* plots depends on the carrier density relative to the density of trapped charges, our model predicts the shape of the curve to have a dependence on voltage. That is, at low voltage (and thus low carrier density), one would expect a more linear response than at high voltage. Figure 4.4 shows that this behavior is in fact observed. As Table 4.1 shows, the calculated ratios of $\frac{n}{N_t}$ at fixed intensity follow the expected trend of increasing with voltage, due to the increasing carrier density, *n*. In addition, the weak dependence of $\frac{n}{N_t}$ on voltage suggests that the exponential dependence of current on voltage is due to the strong voltage dependence of the mobility, rather than *n*.

In addition to changing the shape of the current vs. intensity curve through increasing the carrier density (by increasing the voltage), it should also be possible to change the shape of the curve by increasing the density of trapped charges. Our data suggest that it is possible to do this by slowly aging the sample. With a pressure of only 10^{-5} Torr, there is enough oxygen around that the sample will slowly oxidize if left in the cryostat for an extended period of time. The film was measured on the first day it was loaded in the cryostat (Day 1), after remaining in the cryostat for four days (Day 5), and after remaining in the cryostat for eleven days (Day 12). Figure 4.5 shows the evolution of the shape of the current vs. intensity curve at an applied field of 3×10^5 V/cm as the sample is slowly aged. As expected, the curve becomes more linear as the sample ages because the trap density is increased and, as Table 4.2 shows, the calculated values of
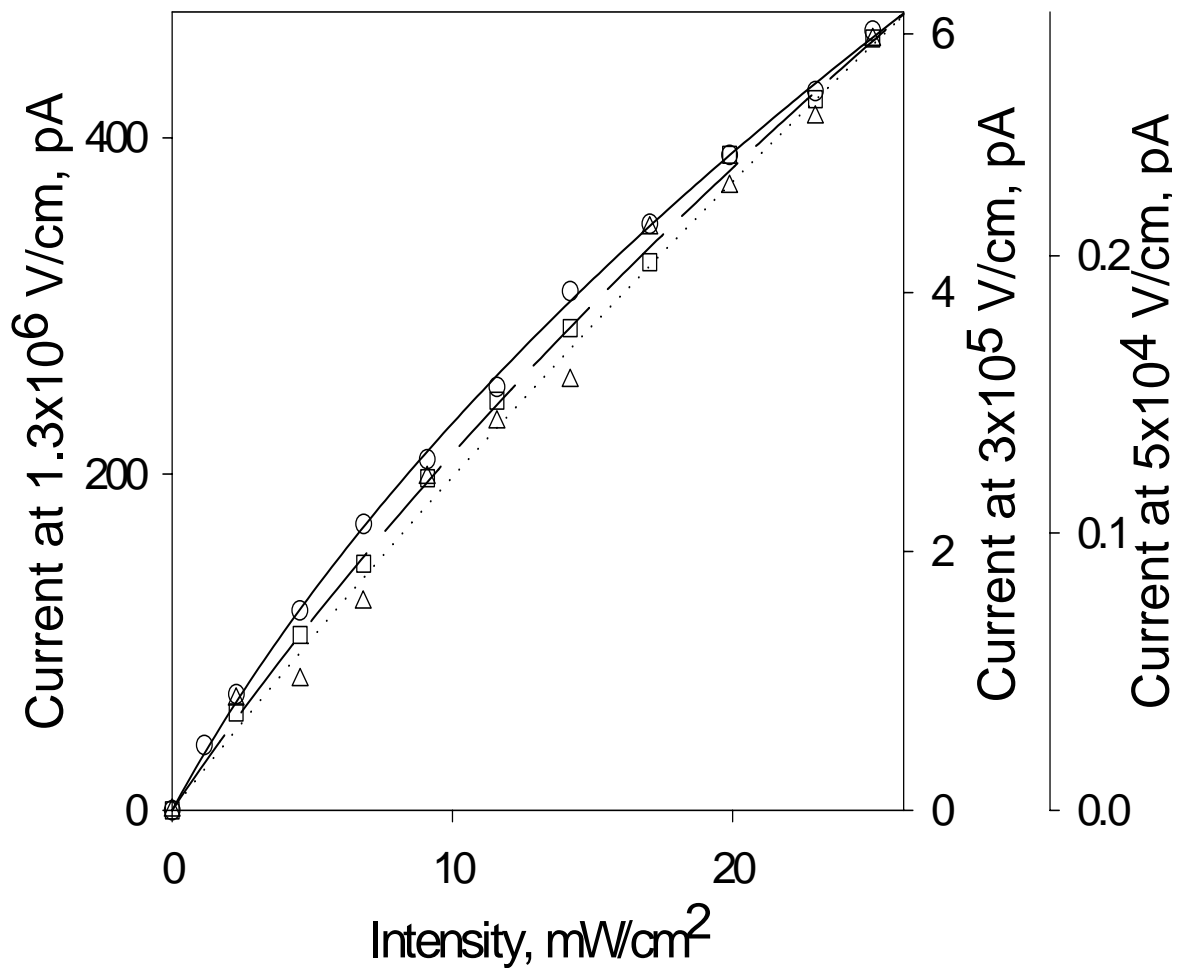
Figure 4.4: Voltage dependence of the shape of the current vs. intensity plot. The circles, squares, and triangles are the data at fields of 1.3×10^6 V/cm, 3×10^5 V/cm, and 5×10^4 V/cm, respectively. The solid, dashed, and dotted lines are the fits to Equation (4.11) for the data at 1.3×10^6 V/cm, 3×10^5 V/cm, and 5×10^4 V/cm, respectively.
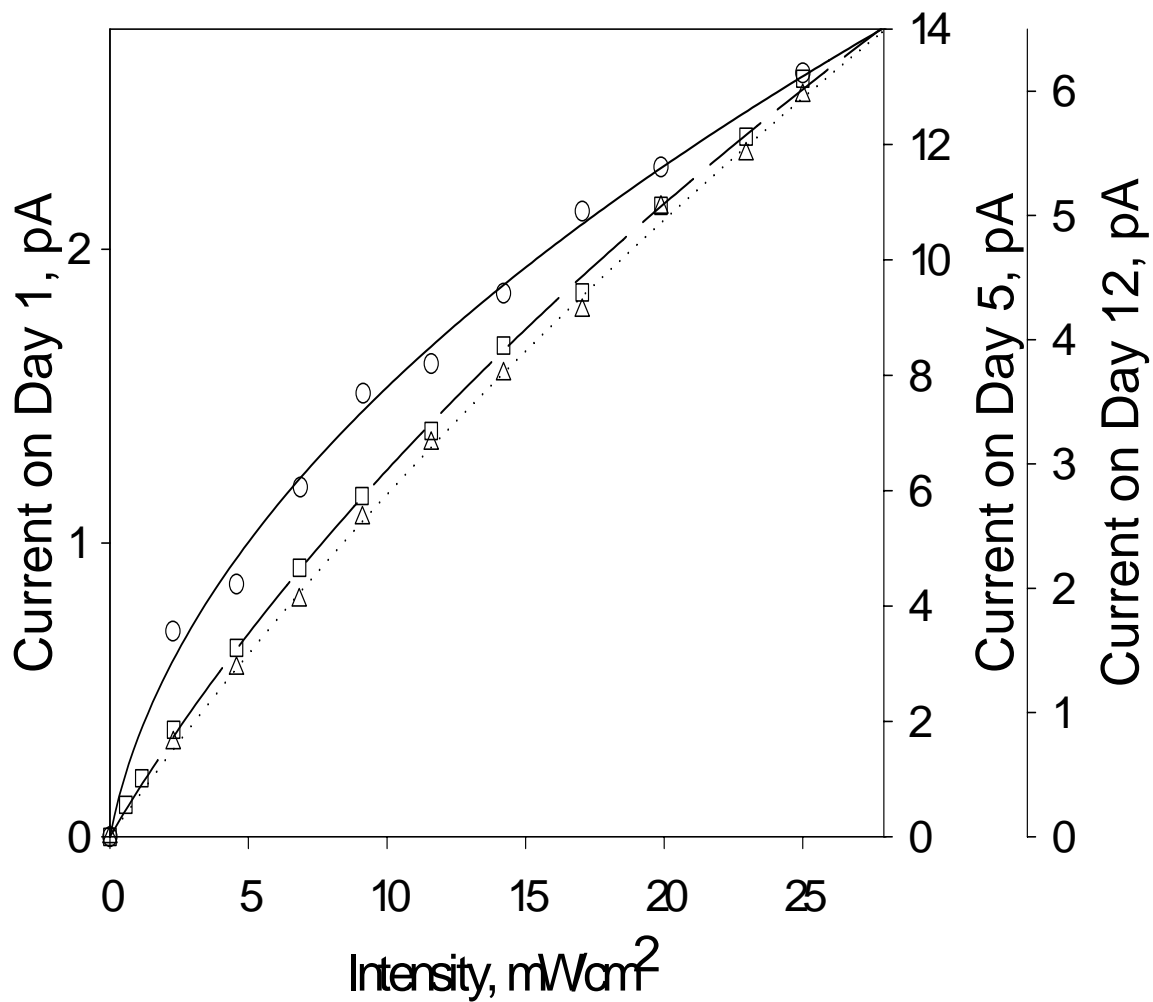
Figure 4.5: Oxidation dependence of the shape of the current vs. intensity plot at a field of 3×10^5 V/cm. The circles, squares, and triangles correspond to the data for Day 1, Day 5, and Day 12, respectively. The solid, dashed, and dotted lines correspond to the fits to equation (2) for the data from Day 1, Day 5, and Day 12, respectively.

$\dfrac{n}{N_t}$ decrease as well. Counter to our expectations, however, while the curve does become more linear from Day 1 to Day 5, the current also increases. This increase in current could be due to a mobility increase (perhaps because additional solvent was removed while the sample was at room temperature and under vacuum) or an increase in the exciton separation efficiency (perhaps due to residual physisorbed oxygen being removed from the film[32, 33]). In the latter case, the increase in n would be accompanied by a even larger increase in N_t (due to aging), therefore still resulting in a decrease in $\dfrac{n}{N_t}$.

4.4 Conclusion

We present the observation of photoconduction in close-packed films of CdSe quantum dots with a low enough density of trapped charges to exhibit bimolecular carrier recombination. These data are shown to be an improvement over previous measurements, which show quasi-monomolecular recombination dynamics due to having a much higher density of trapped charges than carriers. We attribute the improvement to a different synthetic procedure and the fact that the exposure of the films to air was minimized. The intensity dependence of the photocurrent is fit to an equation that is derived from the equations for carrier recombination dynamics, and the ratio of carrier density to density of trapped charges is extracted. We further confirm that these data are a reflection of the recombination dynamics of the system by demonstrating that we can alter the shape of the current vs. intensity curve by changing the carrier density (through changing the voltage), and we suggest that it may also possible to also change the shape by changing the density of trapped charges through slow aging of the sample.

4.5 References and Notes

1.   M. Nirmal, B. O. Dabbousi, M. G. Bawendi, J. J. Macklin, J. K. Trautman, T. D. Harris, and L. E. Brus, "Fluorescence intermittency in single cadmium selenide nanocrystals," Nature **383**(6603), 802-804 (1996).
2.   W. K. Woo, K. T. Shimizu, M. V. Jarosz, R. G. Neuhauser, C. A. Leatherdale, M. A. Rubner, and M. G. Bawendi, "Reversible Charging of CdSe Nanocrystals in a Simple Solid State Device," Advanced Materials **14**(15), 1068-1071 (2002).
3.   M. Shim, C. J. Wang, and P. Guyot-Sionnest, "Charge-tunable optical properties in colloidal semiconductor nanocrystals," Journal of Physical Chemistry B **105**(12), 2369-2373 (2001).
4.   J. L. Blackburn, R. J. Ellingson, O. I. Micic, and A. J. Nozik, "Electron relaxation in colloidal InP quantum dots with photogenerated excitons or chemically injected electrons," Journal of Physical Chemistry B **107**(1), 102-109 (2003).
5.   M. Drndic, M. V. Jarosz, N. Y. Morgan, M. A. Kastner, and M. G. Bawendi, "Transport properties of annealed CdSe colloidal nanocrystal solids," Journal of Applied Physics **92**(12), 7498 (2002).
6.   R. J. Ellingson, J. L. Blackburn, P. R. Yu, G. Rumbles, O. I. Micic, and A. J. Nozik, "Excitation energy dependent efficiency of charge carrier relaxation and photoluminescence in colloidal InP quantum dots," Journal of Physical Chemistry B **106**(32), 7758-7765 (2002).
7.   D. S. Ginger and N. C. Greenham, "Photoinduced electron transfer from conjugated polymers to CdSe nanocrystals," Physical Review B **59**(16), 10622-10629 (1999).
8.   D. S. Ginger and N. C. Greenham, "Charge injection and transport in films of CdSe nanocrystals," Journal of Applied Physics **87**(3), 1361-1368 (2000).
9.   D. S. Ginger and N. C. Greenham, "Charge transport in semiconductor nanocrystals," Synthetic Metals **124**(1), 117-120 (2001).
10.   C. A. Leatherdale, C. R. Kagan, N. Y. Morgan, S. A. Empedocles, M. A. Kastner, and M. G. Bawendi, "Photoconductivity in CdSe quantum dot solids," Physical Review B **62**(4), 2669-2680 (2000).
11.   T. D. Krauss and L. E. Brus, "Charge, polarizability, and photoionization of single semiconductor nanocrystals," Physical Review Letters **83**(23), 4840-4843 (1999).
12.   M. Shim and P. Guyot-Sionnest, "N-type colloidal semiconductor nanocrystals," Nature **407**(6807), 981-983 (2000).
13.   C. J. Wang, M. Shim, and P. Guyot-Sionnest, "Electrochromic nanocrystal quantum dots," Science **291**(5512), 2390-2392 (2001).
14.   C. J. Wang, M. Shim, and P. Guyot-Sionnest, "Electrochromic semiconductor nanocrystal films," Applied Physics Letters **80**(1), 4-6 (2002).
15.   V. L. Colvin, M. C. Schlamp, and A. P. Alivisatos, "Light-Emitting-Diodes Made from Cadmium Selenide Nanocrystals and a Semiconducting Polymer," Nature **370**(6488), 354-357 (1994).

16. B. O. Dabbousi, M. G. Bawendi, O. Onitsuka, and M. F. Rubner, "Electroluminescence from Cdse Quantum-Dot Polymer Composites," Applied Physics Letters **66**(11), 1316-1318 (1995).

17. S. Coe, W. K. Woo, M. G. Bawendi, and V. Bulovic, "Electroluminescence from single monolayers of nanocrystals in molecular organic devices," Nature **420**(6917), 800-803 (2002).

18. W. U. Huynh, J. J. Dittmer, and A. P. Alivisatos, "Hybrid nanorod-polymer solar cells," Science **295**(5564), 2425-2427 (2002).

19. W. U. Huynh, J. J. Dittmer, N. Teclemariam, D. J. Milliron, A. P. Alivisatos, and K. W. J. Barnham, "Charge transport in hybrid nanorod-polymer composite photovoltaic cells," Physical Review B **67**(11), 115326 (2003).

20. A. J. Nozik, "Quantum dot solar cells," Physica E **14**(1-2), 115-120 (2002).

21. M. Bawendi and N. E. Stott, "Preparation of nanocrystallites from metal-containing salts," U.S. Patent Number 2002071952 (June 13 2002).

22. C. B. Murray, D. J. Norris, and M. G. Bawendi, "Synthesis and characterization of nearly monodisperse CdE (E = S, Se, Te) semiconductor nanocrystallites," Journal of the American Chemical Society **115**(19), 8706-8715 (1993).

23. C. B. Murray, C. R. Kagan, and M. G. Bawendi, "Self-Organization of Cdse Nanocrystallites into 3-Dimensional Quantum-Dot Superlattices," Science **270**(5240), 1335-1338 (1995).

24. C. B. Murray, C. R. Kagan, and M. G. Bawendi, "Synthesis and characterization of monodisperse nanocrystals and close-packed nanocrystal assemblies," Annual Review of Materials Science **30**, 545-610 (2000).

25. C. R. Kagan, C. B. Murray, M. Nirmal, and M. G. Bawendi, "Electronic energy transfer in CdSe quantum dot solids," Physical Review Letters **76**(9), 1517-1520 (1996).

26. C. R. Kagan, C. B. Murray, and M. G. Bawendi, "Long-range resonance transfer of electronic excitations in close-packed CdSe quantum-dot solids," Physical Review B **54**(12), 8633-8643 (1996).

27. It should be noted that these measurements require very rigorous sample preparation, as is discussed in Chapter 3.

28. R. H. Bube, *Photoconductivity of Solids* (Wiley, New York, 1960).

29. J. D. McNeill and P. F. Barbara, "NSOM investigation of carrier generation, recombination, and drift in a conjugated polymer," Journal of Physical Chemistry B **106**(18), 4632-4639 (2002).

30. J. E. B. Katari, V. L. Colvin, and A. P. Alivisatos, "X-ray Photoelectron Spectroscopy of CdSe Nanocrystals with Applications to Studies of the Nanocrystal Surface," J. Phys. Chem. **98**(15), 4109-4117 (1994).

31. K. W. Bagnall, *The Chemistry of Selenium, Tellurium and Polonium*, Topics in Inorganic and General Chemistry (Elsevier Publishing Company, Amsterdam, 1966), p. 200.

32. R. H. Bube, "Oxygen sorption phenomena on cadmium selenide crystals," Journal of Chemical Physics **27**(2), 496-500 (1957).

33. R. H. Bube, "The basic significance of oxygen chemisorption on the photoelectronic properties of CdS and CdSe," Journal of the Electrochemical Society **113**(8), 793-798 (1966).

Chapter 5

Photoconductivity of CdSe QD Films with Increased Exciton Ionization Efficiency

5.1 Introduction

Semiconductor quantum dots (QDs) are of interest because of their tunable optical and electronic properties and their applications as novel materials for biological imaging,[1-5] light emitting diodes,[6-9] photovoltaics,[10-12] photodetectors,[13, 14] and lasers.[15, 16] Colloidal nanocrystals are of particular interest because of the ease with which they can be synthesized, manipulated, and assembled into device structures. Many of the applications of colloidal QDs involve charge transport, and recent experiments have underscored the important role that charges play in the optical properties of colloidal quantum dots.[17-20] Furthermore, the motion of electrons in QD arrays is interesting because one can think of the system as an artificial solid composed of artificial atoms.[21] Because of localization of electrons on the QDs, strong correlations are expected in the motion of charge carriers. However, because dark conductances are found to be extremely small in uncharged quantum dot arrays, photoconductivity is the best way to study electronic motion in these systems.

Enhancing the photoconductivity in QD films would advance both the understanding of the physics of charges in QDs and the realization of QD applications. Until now, an increase in the photoconductivity has only been achieved by annealing QD

films at temperatures high enough to decompose the QD capping layer.[22] The dark

conductivity of QD films in an electrochemical cell has, however, been shown to increase

upon treatment with diamine cross-linking.[23, 24] In this paper, we present a set of post-

deposition chemical treatments that increase the photoconductivity in CdSe QD films by

orders of magnitude. We show that the photoconductivity in CdSe QD films can be

enhanced by treatment with amines or a strong base. While the untreated samples show a

photocurrent that is highly voltage dependent at all voltages, such behavior is observed

only at low voltages for the samples treated with amines or sodium hydroxide; at higher

voltages, the photocurrent becomes linear with voltage. For samples exhibiting the

greatest enhancement following treatment, the photocurrent also exhibits saturation at

very high voltage. We present a model that is able to explain all three regimes of voltage

dependence in the treated samples by assuming: (1) an ionization efficiency that is highly

voltage dependent and that saturates at unity at the voltage for which the current-voltage

(i-V) curve becomes linear, and (2) non-injecting contacts. As well as predicting the

trends observed in the voltage dependence of the photocurrent, our model also predicts

that the product of the mobility and lifetime for electrons cannot be more than ~ 10 times

greater than the product for holes. We show that the main parameters leading to the

increase in photoconductivity are (1) the degree of surface passivation and (2) the spacing

between QDs. Whether or not the molecules used to treat the films are conjugated or

able to cross-link the QDs do not appear to be significant factors.

126

5.2 Experimental Details

5.2.1 Sample preparation

CdSe QDs with a radius of 20 Å are synthesized using a method based on a cadmium salt precursor.[25]   A cadmium precursor solution consisting of cadmium hydroxide (98%), tri-*n*-octylphosphine (TOP, 90%), and cis-9-octadecenoic acid (99%) is degassed under vacuum for one hour. After cooling to room temperature, the selenium precursor, tri-*n*-octylphosphine selenide (TOPSe, 1.5 M solution), is added and the precursors are injected into a 335 ºC coordinating solvent solution containing TOP, oleylamine, and dioctyl ether. Upon cooling, butanol is added to the growth solution.

An aliquot of the growth solution is removed and processed following previously established procedures for making close-packed films.[26-32] These procedures narrow the size distribution and remove excess organics that would inhibit formation of an optically clear and close-packed film. After an initial precipitation with methanol, the precipitate is dissolved in hexane and placed in the freezer for 10 minutes to encourage precipitation of salts. The sample is then centrifuged and butanol is added to the supernatant. This solution is passed through a 0.2 μm filter and a second precipitation is carried out with methanol. The resulting precipitate is dissolved in hexane and butanol, passed through a 0.1 μm filter, and a final precipitation with methanol is performed. The final precipitate is dissolved in hexane and dried under vacuum. The powder of QDs is dissolved in a 9:1 mixture of hexane:octane, filtered through a 0.02 μm filter, and dried under vacuum once again. The QD powder is then brought into an inert atmosphere glovebox, where it is redissolved in 9:1 hexane:octane. Films are deposited by drop-casting this solution onto lithographically patterned silicon substrates.

The silicon devices are fabricated by thermally growing 330 nm of oxide on degenerately doped silicon substrates and patterning 200 x 800 x 0.1 μm^3 gold bar electrodes using a standard lift off procedure.[33] The spacing between electrodes is 1μm. The devices are mounted on chip carriers, and electrical contacts from the electrodes to the chip carrier are made prior to film deposition.

5.2.2 Conductivity measurements

All photoconductivity measurements are carried out under vacuum in a Janis VPF-100 cryostat. The 514 nm line of an Ar^+ laser is used to excite the samples. The laser beam with an intensity of ~ 14 mW/cm^2 (unless otherwise stated) is focused onto a pair of gold electrodes. Current measurements are made with a Keithley 6517 electrometer, which also supplies the source-drain voltage. For the photocurrent versus voltage curves, the voltage is stepped in 2 V increments from 0 V to 20 V, and in 10 V increments from 20 V to 100 V. The data points are recorded after a delay of 10 seconds. Unless otherwise stated, the data are taken with the sample at 77 K.

5.2.3 Treatment of films

After measuring the photoconductivity of a QD film, the sample is returned to the glovebox where it is immersed in a 0.1 M solution of the selected reagent: butylamine, aniline, 1,6-diaminohexane, 1,4-phenylenediamine, tri-*n*-butylphosphine, or sodium hydroxide. The solvent for each solution is anhydrous acetonitrile, except for sodium hydroxide which is dissolved in anhydrous methanol due to its limited solubility in acetonitrile. The sample is soaked for 10 minutes, rinsed with 1 mL of solvent, and dried

in an oven at 70 ºC for 1 hour to remove excess solvent.[24] Two types of butylamine-treated samples are presented: one dried in the oven and the other dried in the glovebox overnight. For all samples other than the one dried overnight, reference and treated devices were measured on the same day.

5.2.4 Atomic Force Microscopy

Sample thicknesses are measured using atomic force microscopy (AFM), with a Digital Instruments Nanoscope IIIa in D3000 tapping mode. AFM samples are prepared in the same manner as the samples used for electrical measurements, except that they are deposited in air onto clean glass slides. The sample is scratched down to the glass to remove the QD film from a small region of the sample. A 30-50 μm x 30-50 μm region, half over the glass slide and half over the film, is scanned by the AFM, allowing a calculation of the average height of the film relative to the glass slide. Heights are measured in three separate regions on each sample. After chemical treatment, the average height of the film is measured in the same regions. As the size of the CdSe core does not change, the decrease in the thickness of the films is due to a decrease in QD spacing after treatment with 1,4-phenylenediamine, 1,6-diaminohexane, aniline, or tri-n-butylphosphine. The analysis is less straightforward after treatment with butylamine and sodium hydroxide, because some of the film is redissolved. Thus, for the butylamine treated sample the height of the film is compared before and after drying in the oven, when no QDs can be lost. The change in QD spacing before and after drying in the oven also gives the minimum possible spacing before drying in the oven. This information, combined with the assumption that an integer number of monolayers is lost (assumed

because the film begins as only 20 monolayers, and the film roughness is smaller than the thickness of a monolayer), allows for a calculation for the QD spacing for the butylamine samples, before and after drying in the oven.

5.2.5 Transmission Electron Microscopy

The spacing between close-packed QDs in the reference samples is found using transmission electron microscopy (TEM). Samples are prepared by drop casting a solution of QDs onto a carbon TEM grid. The solution is ~200 times more dilute than the solution used to make films in order to form a monolayer of QDs. The sample is imaged on a JEOL 200CX electron microscope under 100,000 times magnification.   After averaging the QD spacing for over ninety QDs, the interdot spacing in the pre-treated films was determined to be 1.1 nm ± 0.3 nm, which is consistent with previous studies.[32]

5.2.6 Fluorescence microscopy

Fluorescence microscopy is used to study fluorescence quenching as a function of applied voltage in the electrically active portion of the QD film. The device structure is the same as that used for the photoconductivity measurements. A home-built epifluorescence, wide field microscope is used to image inside a cold finger cryostat with a 0.7 mm thick window. The objective is a 60x 0.7 NA DIC Nikon objective with a working distance of ~2 mm, with the correction collar set to 0.75 mm. The excitation source is an Ar^+ laser operating at 514 nm and ~ 300 W/cm^2. Collection of the fluorescence is passed through a 514 nm notch filter and a dielectric band pass filter to eliminate excitation light from the collected path. This collected light was then imaged

on a 1024 x 1024 pixel CCD detector (Princeton Instruments Micromax, Roper

Scientific).

5.3 Results

5.3.1 Photocurrent at 77 K before and after various treatments

Figures 5.1, 5.2, 5.3, and 5.5 are photo-induced current versus voltage (*i-V*)

curves for films of CdSe QDs measured at 77 K. Each *i-V* curve is scaled to display the

untreated (reference) and treated films on the same plot. The photocurrent of the

reference sample is designated as i_r, and the photocurrent after treatment is designated as

i_t. The lines connecting the data points serve only as a visual aid. The dark current from

0 to 100 V is below the noise (< 0.1 pA) for all reference and treated samples. In each

figure the current for the reference is highly nonlinear in voltage over the entire range.

The currents at 50 and 100 V are typically on the order of 1 pA and 10-25 pA,

respectively. These results agree well with those found in previous studies of

photoconductivity in CdSe QD films.[22, 26, 30, 34]

The *i-V* curve shown in Figure 5.1(a) is for a sample treated with butylamine, an

unconjugated molecule with a single amine group; this sample was dried overnight at

room temperature. Upon treatment the photoconductivity increases 82 fold at 100 V and

310 fold at 50 V. In addition, the shape of the *i-V* curve after treatment becomes linear

above ~ 60 V. Analysis of AFM data suggests that the QD spacing after this treatment in

~ 7 Å.

When a sample is treated with butylamine and dried in the oven at 70 ºC, as

opposed to drying at room temperature overnight, there is a much larger increase in the
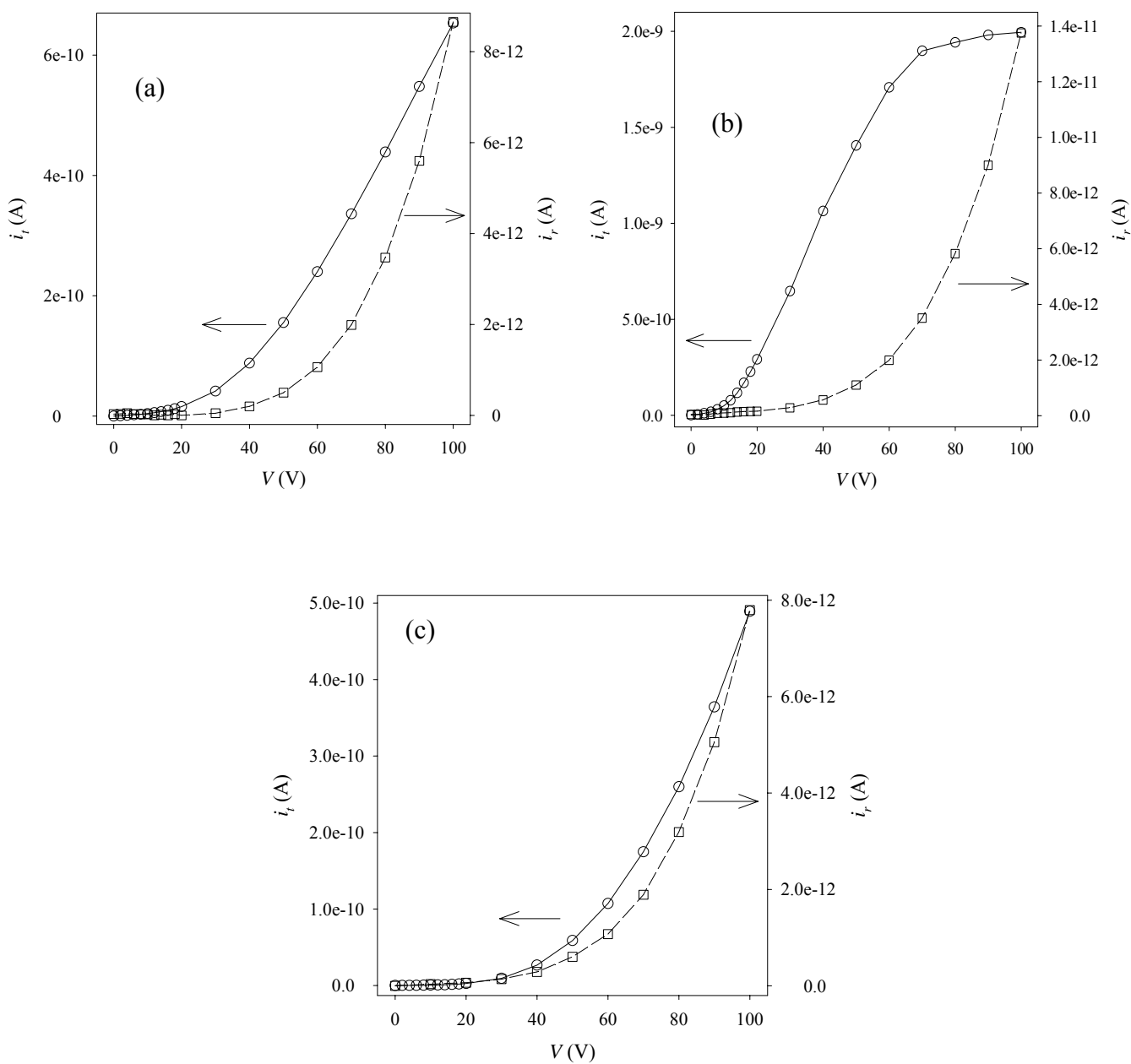
Figure 5.1: Photocurrent at 77K before (open squares, dashed line) and after (open circles, solid line) treatment with (a) butylamine (dried at room temperature overnight), (b) butylamine (dried at 70oC for 1 hour), (c) tri-n-butylphosphine.

photoconductivity. Figure 5.1(b) shows a 145 fold increase in photocurrent at 100 V and a 1280 fold increase at 50 V. As in Figure 5.1(a), the *i-V* curve in Figure 5.1(b) also shows a transition to a linear regime; however, this transition occurs at ~14 V. Furthermore, saturation of the photocurrent is evident in Figure 5.1(b), above ~ 70 V. Analysis of AFM data shows that QDs in butylamine treated films are brought 5 Å closer together (to ~2 Å) when dried at an elevated temperature.

Figure 5.1(c) shows the result of treatment with a shorter analog of TOP, tri-*n*-butylphosphine (TBP). AFM data suggests that the QD spacing after treatment with TBP is ~6-7 Å, which is very close to the ~7 Å spacing of the butylamine-treated sample in Figure 5.1(a). However, the TBP-treated sample shows only a 98 fold increase in photocurrent at 50 V, compared to a 310 fold increase at 50 V for the sample treated with butylamine and dried overnight. The difference between the photocurrent increases of these two samples is smaller at 100 V (98 fold for the room temperature-dried butylamine-treated sample and 83 fold for the TBP-treated sample). The shape of the *i-V* curve for the TBP-treated sample is also far less linear than that of the sample treated with butylamine and dried overnight.

Figure 5.2(a) is data for a sample treated with 1,6-diaminohexane, an unconjugated diamine. At 100 V, the conductivity of the treated sample has increased 33 fold over that of the reference and at 50 V it has increased 225 fold. The shape of the 1,6-diaminohexane treated *i-V* curve is similar to those of the butylamine-amine treated samples in that there is a clear linear region. For the former, the linear region begins at ~ 30 V. There is also evidence of saturation beginning above ~ 80 V, which indicates that the photocurrent is approaching saturation. The magnitude of the photocurrent at 100 V
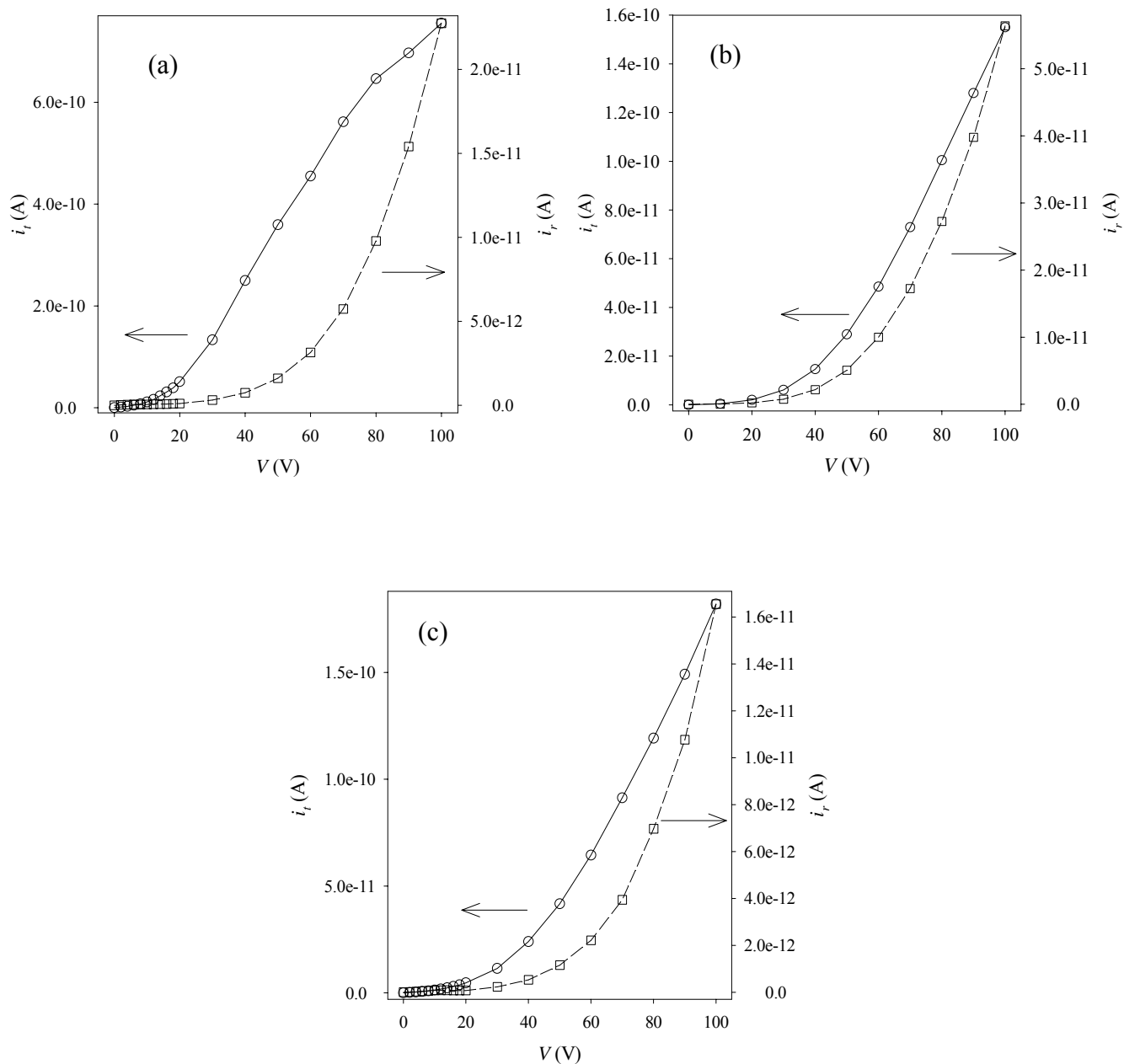
Figure 5.2: Photocurrent at 77K before (open squares, dashed line) and after (open circles, solid line) treatment with (a) 1,6-diaminohexane, (b) aniline, and (c) 1.4-phenylenediamine.

is on the order of hundreds of picoamps, similar to that of the sample treated with butylamine and dried overnight. AFM data suggests that after treatment with 1,6-diaminohexane the QD spacing is ~3-5 Å.

Figure 5.2(b) displays the results for treatment with aniline, a conjugated molecule with one amine group. The photocurrent increases 3 fold at 100 V upon treatment and 6 fold at 50 V. The initial photocurrent is somewhat higher than for the other samples. Nonetheless, the shape of the reference curve is nonlinear over the entire voltage range, whereas the treatment induces a linear regime above ~ 60 V. The magnitude of the photocurrent at 100 V is hundreds of picoamps, similar to Figures 5.1(a) and 5.2(a). AFM data suggests that the spacing between QDs after treatment with aniline is ~ 5 Å.

Treatment with 1,4-phenylenediamine, a conjugated diamine, also shows an increase in photoconductivity. However, the magnitude of the photocurrent at 100 V is less than for treatment with aniline, 1,6-diaminohexane, or butylamine. Figure 5.2(c) shows an 11 fold increase in photocurrent at 100 V, a 36 fold increase at 50 V, and the onset of a linear response at 60 V. AFM data suggests that the spacing between QDs after this treatment in ~5 Å, the same as for the aniline-treated sample.

The reason amines increase the photocurrent may be attributed to their basic and passivating nature as discussed below. Therefore, treatment with a very small and strong base, also known to increase photoluminescence quantum yield,[35] should increase photoconductivity as well. Figure 5.3 shows the result of treatment with sodium hydroxide. The photocurrent increases by a factor of 440 at 100 V and by a factor of 5100 at 50 V. The shape of the i-V curve resembles that of the sample treated with
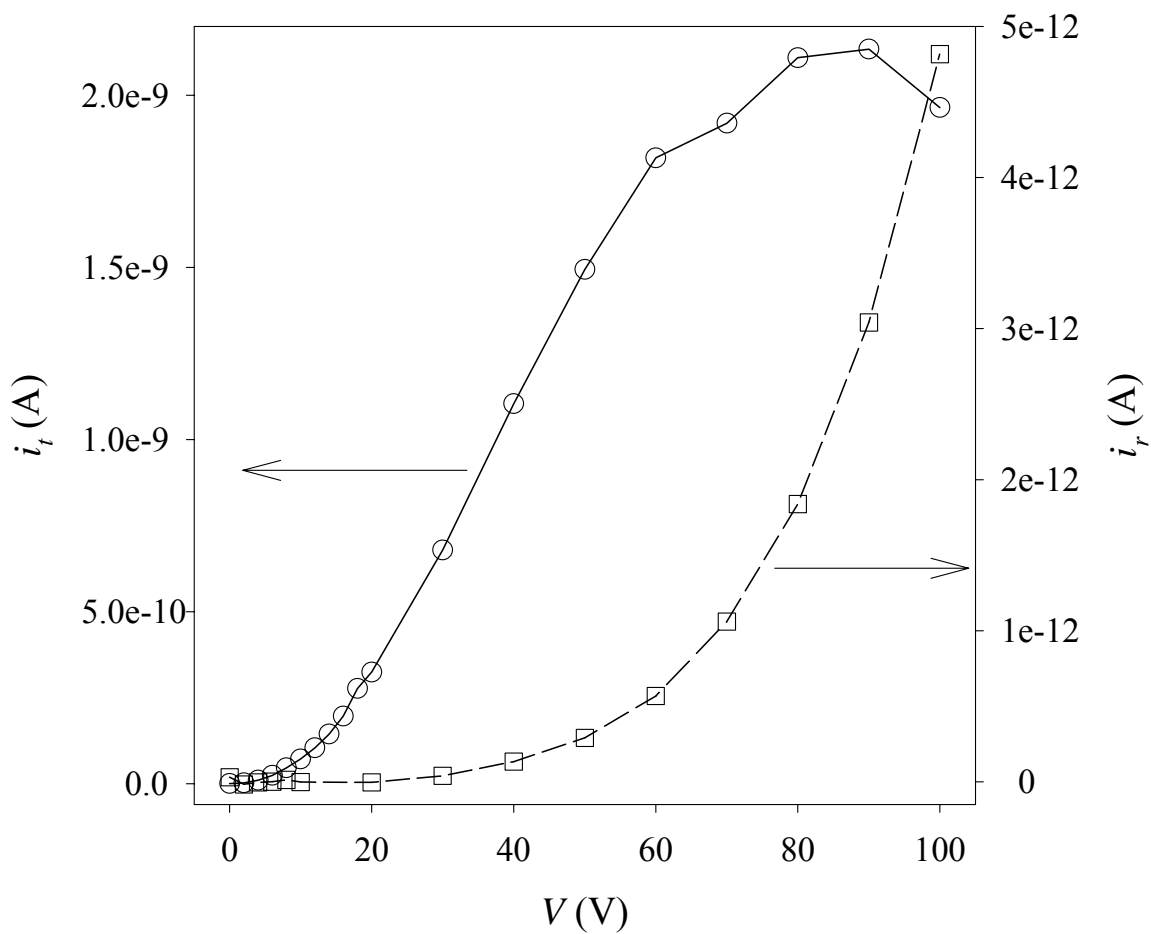
Figure 5.3: Photocurrent at 77K before (open squares, dashed line) and after (open circles, solid line) treatment with sodium hydroxide.
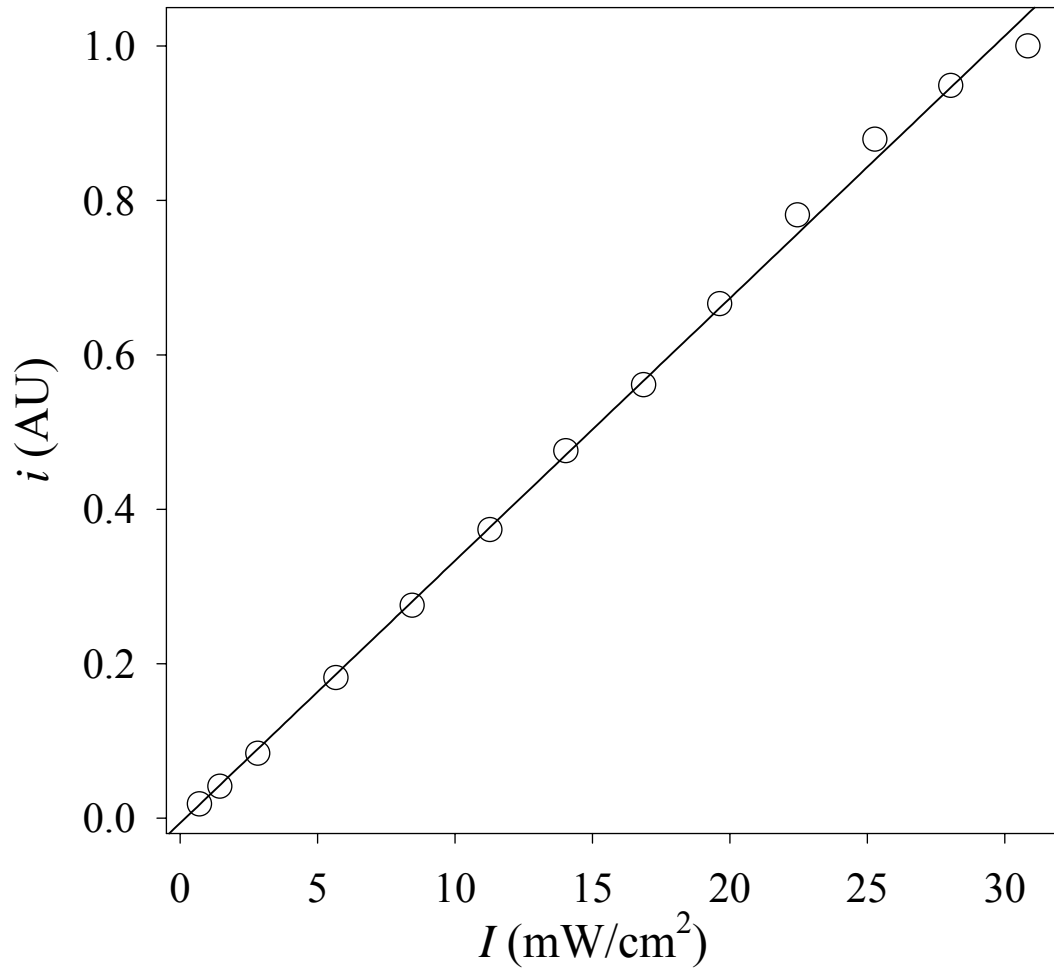
Figure 5.4: Intensity dependence of the photocurrent for a sample treated with sodium hydroxide at 100V, after the photocurrent has saturated with voltage. Open circles represent data and the solid line represents a linear fit.
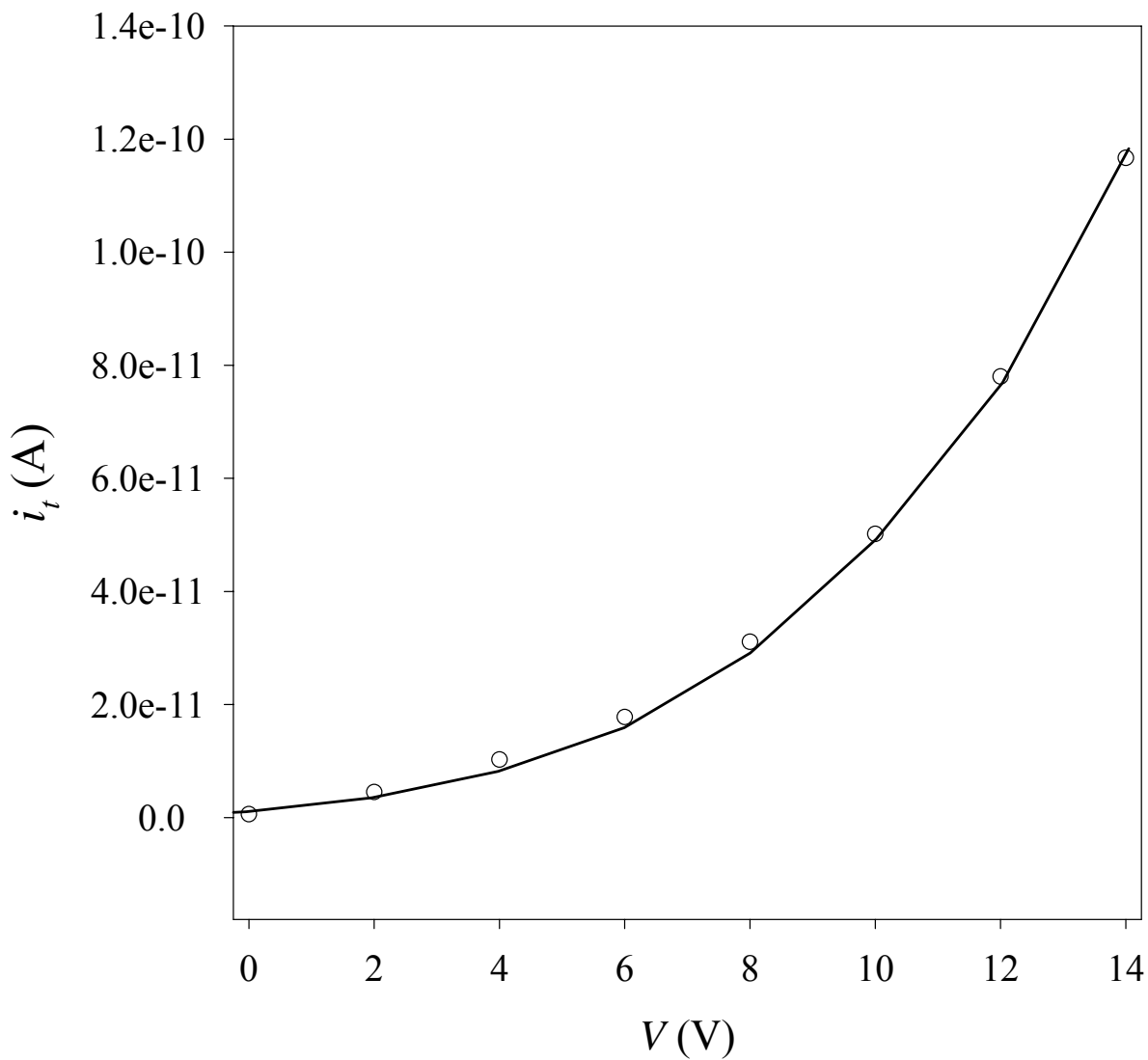
Figure 5.5: Photocurrent data (open circles) for a sample treated with butylamine and dried at $70^{o}C$ for one hour, plotted with reference data (solid line). The current and voltage values for the reference data are scaled to illustrate that the shape of the butylamine treated *i-V* curve, at low voltages, is the same as the shape of the reference at all voltages.

butylamine (oven-dried) in that it has a linear region followed by a saturation. The linear region starts at ~18 V, and the current is on the order of nanoamps. Figure 5.4 shows the photocurrent intensity dependence for a sample treated with sodium hydroxide at a voltage corresponding to photocurrent saturation.

The open circles in Figure 5.5 represent the low voltage portion of the *i-V* curve for the butylamine-treated sample which is dried at 70 °C; the full *i-V* curve for the same sample is shown in Figure 5.1(c). The solid line in Figure 5.5 represents the photocurrent of the untreated sample, scaled in voltage and current to demonstrate that the shape of the *i-V* curve for the treated sample in the low voltage regime is the same as the shape of the reference *i-V* curve at all voltages. The nonlinear portion of the *i-V* curve at low voltages is not significantly altered by an of the treatments.

5.3.2 Fluorescence quenching

Figure 5.6(a) shows the correlation between the photoconductivity and photoluminescence of a sample treated with 1,6-diaminohexane. The *i-V* curve for the sample (solid line, open circles) is plotted in conjunction with fluorescence quenching data (solid squares). ΔI_F represents the change in fluorescence intensity when the electric field is applied. Because of a high level of background fluorescence, it is not possible to determine a quantitative value for the percent fluorescence quenching. The white region of Figure 5.6(a) represents the voltage range over which the *i-V* curve exhibits highly voltage dependent behavior, and the white-gray boundary is approximately the range at which the *i-V* curve becomes linear. The degree of fluorescence quenching increases quickly when the voltage becomes high enough for the *i-V* curve to become linear and
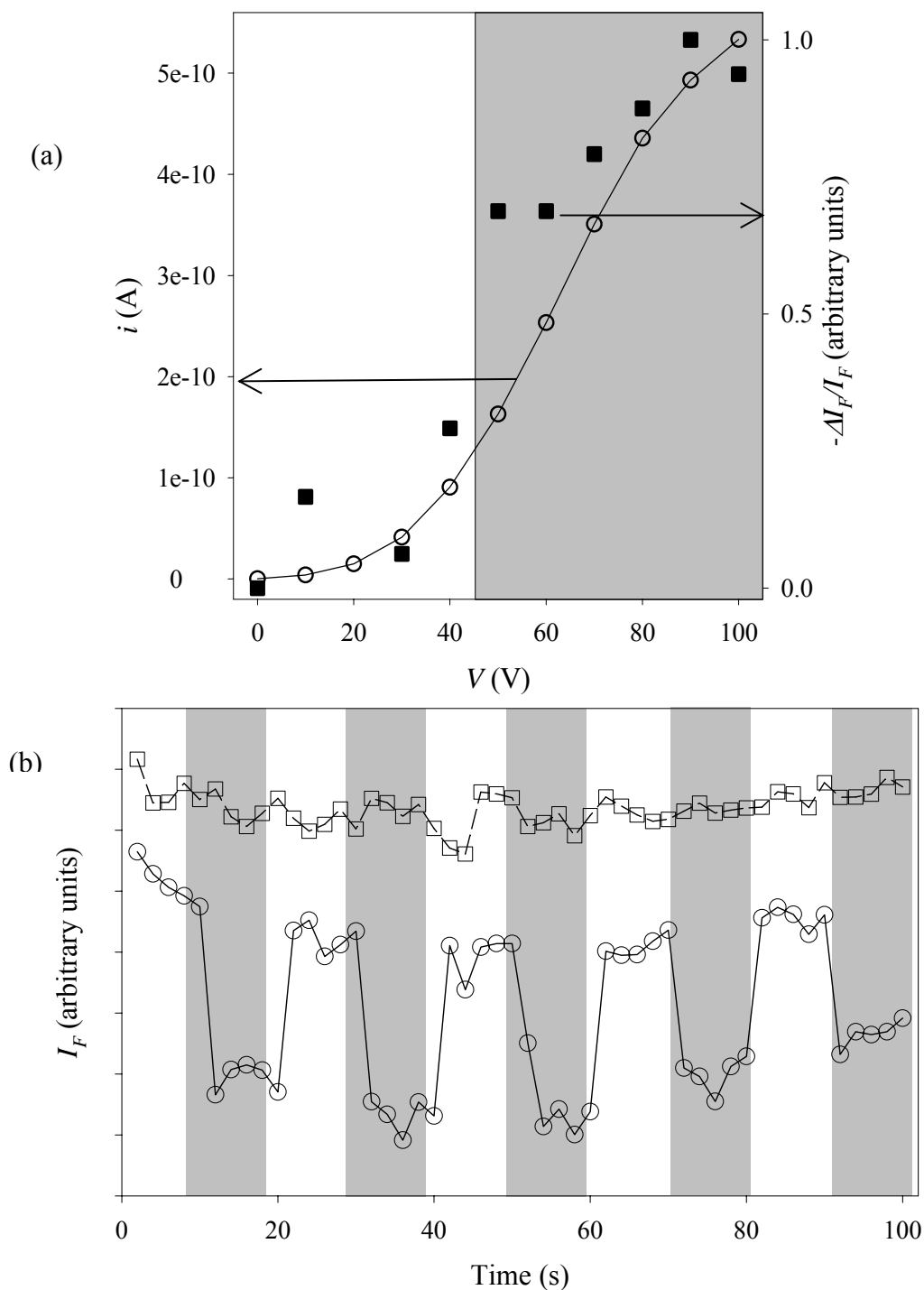
Figure 5.6: (a) Fluorescence quenching data (filled squares) for a sample treated with 1,6-diaminohexane compared to the i-V curve (open circles, solid line) for the same sample. The shaded region contains voltages at which the i-V curve is linear and a saturated exciton ionization efficiency is predicted. (b) Time trace of the fluorescence intensity for the same sample as in (a) where the white region corresponds to 0V and the shaded region corresponds to +20V (open squares, dashed line) or +100V (open circles, solid line). The curves corresponding to +20V and +100V are offset for clarity. A quantitative number for the percent fluorescence quenching in (a) and (b) was not obtainable due to high background fluorescence.

then saturates. Figure 5.6(b) demonstrates that while no significant fluorescence quenching is observed when +20V is applied, a distinctive and reversible fluorescence quenching is observed when +100V is applied.

5.3.3 Temperature dependence

Figure 5.7(a) shows the *i-V* curves for a reference sample at 77 K and 300 K; the photocurrent at 100 V is more than 30 times smaller at 300 K than at 77 K, consistent with previous observations.[26] Figure 5.7(b) shows the *i-V* curves for a sample treated with butylamine and oven-dried, taken at 77 K and 300 K; the photocurrent at 100 V is only about 5 times smaller at 300 K than at 77 K. The photocurrent at 300 K still reaches a linear regime, although not until a higher voltage. Furthermore, while the treated *i-V* curve at 77K saturates at 90 V, at 300 K saturated photocurrent is not observed in the range of voltages that are measured.

5.4 Discussion

5.4.1 A comparison of the different treatments

A comparison of the *i-V* curves in Figures 5.1(a) – 5.1(c) suggests that two phenomena increase photoconductivity and affect *i-V* curve shapes: QD spacing, and the functionality of the reagent used for treatment. The amine functionality of butylamine is expected to passivate recombination centers at the QD surface. This idea is supported by the observation that amines are known to increase the photoluminescence quantum yield of QDs.[25,36-39] The increase in photoconductivity for the TBP-treated sample is probably predominantly caused by the decrease in QD spacing, whereas the increase for the
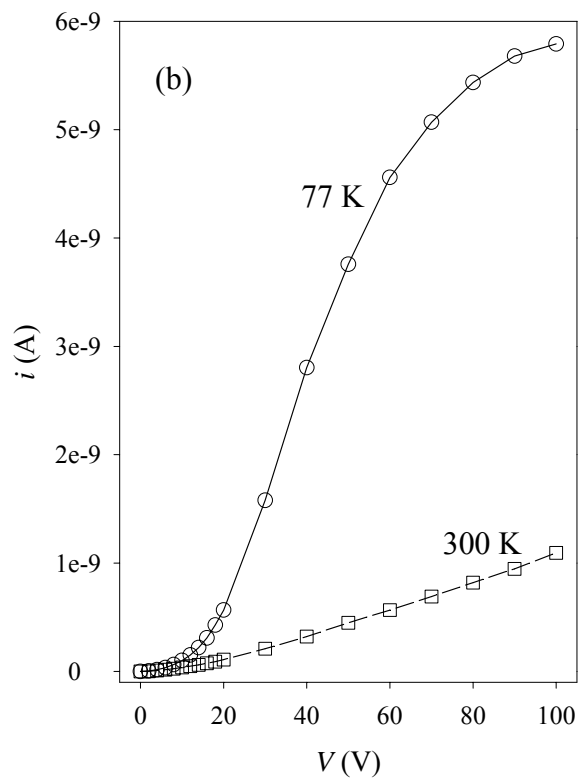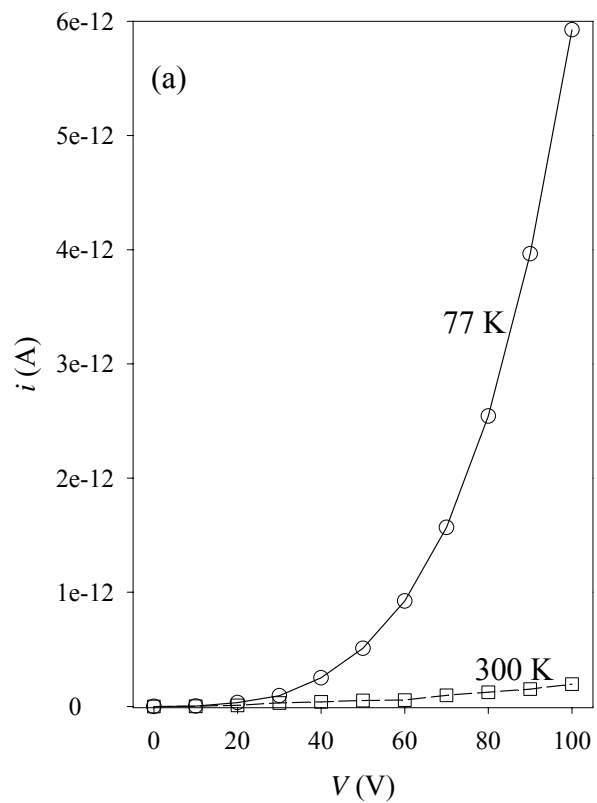
Figure 5.7: (a) Photocurrent before treatment at 77K (open circles, solid line) and 300K (open squares, dashed line). (b) Photocurrent after treatment with butyl amine (oven-dried) at 77K (open circles, solid line) and 300K (open squares, dashed line).

butylamine-treated sample dried overnight probably results from both a decrease in QD spacing and an increase in surface passivation.

It has been suggested that the use of cross-linking molecules can improve the conductivity of QD films.[23, 24] While the photoconductivity does improve with 1,6-diaminohexane, shown in Figure 5.2(a), it increases with butylamine as well. Furthermore, the QDs are 2 - 4 Å closer together after the 1,6-diaminohexane treatment compared to the butylamine treatment, so it does not appear that cross-linking has a significant impact, compared with surface passivation and QD spacing.

From the shape of the i-V curve and the magnitude of the photocurrent in Figure 5.2(b), after treatment with aniline, it appears that conjugation also does not affect the photoconductivity as much as passivation and QD spacing. In fact, aniline may have less of a passivating effect than 1,6-diaminohexane or butylamine because its bulkier phenyl group may inhibit surface binding. In addition, if conjugation or cross-linking were responsible for the increase in photoconductivity, treatment with 1,4-phenylenediamine should have displayed the greatest improvement. The fact that the photoconductivity does not increase dramatically, as seen in Figure 5.2(c), strengthens the argument that surface passivation and QD spacing, rather than conjugation or cross-linking, are responsible for the larger photocurrents and the changes in the i-V curve shapes.

The similarities between the results obtained after treatment with sodium hydroxide and after treatment with butylamine (oven-dried) suggest a similar mechanism by which the photocurrent is improved. The major difference between treatment with sodium hydroxide or butylamine (oven-dried) and treatment with the other four amines is the degree to which the QD spacing is decreased.

5.4.2 Physical origins of photocurrent saturation: blocking contacts

Previous studies[26] have established that photoconduction in CdSe QD films is limited by field-induced ionization of photo-generated excitons; the majority carrier is assumed to be the electron. The exciton ionization process requires an electron to tunnel to a neighboring QD, and thus is highly dependent on voltage. A model for this voltage dependence has been previously proposed.[26] The shapes of the reference *i-V* curves seen in Figures 5.1-5.3, 5.5, and 5.7 correspond well to those previously reported, where the highly voltage dependent *i-V* curve is attributed to the voltage dependence of exciton ionization.

The most obvious change in the voltage dependence of the *i-V* curves upon treatment with reagents is seen in Figures 5.1(b) and 5.3, the sample treated with butylamine and dried at 70 °C, and the sample treated with sodium hydroxide, respectively. For these, the photocurrent saturates to a constant value at high voltages. In traditional photoconductors, such a saturation of photocurrent with voltage is seen when both the minority and majority carriers are mobile but it is not possible to inject either carrier from the electrodes.[40, 41] The contacts in this situation are referred to as blocking,[42] and photocurrent is maintained by carriers being extracted at the electrodes. The photocurrent under these circumstances is referred to as primary photocurrent [40, 43] because it comes only from carriers generated within the sample.

It is not surprising that the contacts are blocking. From previous dark conductivity studies one knows that it is difficult to inject electrons into the conduction band and nearly impossible to inject holes into the valence band of a CdSe QD from a gold electrode.[22, 33, 44] This can be understood from the positions of the conduction and

valence states of CdSe QDs with respect to the work function of gold: for 4 nm diameter CdSe QDs, the conduction state is ~ 0.5 eV above and the valence state is ~ 1.6 eV below the work function of gold.[9, 44, 45]

Complete saturation of the photocurrent occurs at voltages that are high enough that the following requirements are met: (1) carriers are extracted rapidly enough that there is no recombination of either carrier within the film, and (2) the generation rate does not depend on the field. Thus, the electron and hole lifetimes are transit-time limited, rather than being recombination-time limited. When the photocurrent saturates, the photoconductive gain, G, becomes equal to unity. This can be seen from the following equation for photoconductive gain, which is valid for primary photoconductors:[40, 43]

$$G = \frac{l_p + l_n}{L},$$ (5.1)

where L is the distance between the electrodes, and l_p and l_n are the distances traveled by the hole and electron, respectively, before recombination, trapping, or arrival at an electrode. Since L is the maximum value for $l_p + l_n$, the maximum value for the photoconductive gain, G, is 1.[40]

The photocurrent, i, is related to G as follows:[40]

$$i = eGF,$$ (5.2)

where e is the charge of an electron and F is the number of free carriers (ionized excitons) created per second by photoexcitation anywhere in the sample. Thus we interpret the saturation of the photocurrent as a saturation of G at $G = 1$.

In the saturation regime of the i-V curve we can determine the value of F for $G = 1$, F_{sat}. Whether or not this value is reasonable given the photoexcitation intensity and QD film absorption serves as a check on the applicability of the model. To

experimentally determine the photon absorption, a thin film of CdSe QDs is deposited on a glass slide and treated with butylamine; the thickness after treatment is determined by AFM to be 45 nm, and the optical density is determined to be 0.027 at 514 nm. This corresponds to a 100 nm thick film having an optical density of 0.06 at 514 nm. Based on the data in Figure 5.1(b) or Figure 5.3, F_{sat} is calculated to be $\sim 1.3 \times 10^{10}$ electrons per second. Using Equation (5.2) with $G = 1$ and given the excitation intensity, the active area between the electrodes, and assuming one carrier per absorbed photon, the above value of F_{sat} leads to an absorption, A, of ~ 0.13. This corresponds to an optical density of ~ 0.06, consistent with the direct measurement of absorption.

In addition to explaining the saturation of the photocurrent with voltage, Equation (5.2) also predicts that the photocurrent in the saturation regime should be linear with intensity, since F_{sat} depends linearly on intensity (see also Equation 5.3 below). The expected linear dependence is seen in Figure 5.4.

5.4.3 Physical origins of the linear *i-V* region: unity ionization efficiency

There is a significant difference between the photoconductivity of the amine- and base-treated CdSe QD films at low voltages and at high voltages. As is seen in Figure 5.5 (the *i-V* curve for a sample treated with butylamine and dried at 70 °C), at low voltages the photocurrent has the same strong dependence on voltage that is present at all voltages for the reference sample. This voltage dependence has been previously ascribed to the highly voltage dependent nature of exciton ionization efficiency.[26] However, to observe saturation of the photoconductivity at high voltages, F must be voltage independent. The rate of carrier generation in the entire sample is

146

$$F = I \cdot A \cdot S \,, \tag{5.3}$$

where I is the intensity in units of photons per second, A is the absorption in units of excitons per photon, and S is the ionization efficiency in units of separated electrons per exciton ($0 \leq S \leq 1$). Since F is constant and S is monotonically increasing with field, we must have $S = 1$ in the saturation regime.

In fact, the existence of a linear regime in the i-V curves of all of the amine- and base-treated samples is also consistent with $S = 1$. In steady state the photocurrent can be written as

$$i = (\tau_n \mu_n + \tau_p \mu_p) e \frac{V}{L^2} \cdot F \,, \tag{5.4}$$

where τ_n and τ_p are the lifetimes of the electron and hole, respectively, μ_n and μ_p are the electron and hole mobilities, respectively, and V is the applied voltage. This equation predicts a linear voltage dependence if F (and therefore S) is field independent. In the low-voltage regime (and at all voltages for the reference samples), where S (and therefore F) has a strong field dependence, the photocurrent becomes similarly strongly dependent on voltage.

The above model predicts that at voltages where the i-V curve becomes linear, a drop in fluorescence intensity should be observed from the QDs between the electrodes because excitons ionize rather than recombining in the QDs. Furthermore, the amount of fluorescence quenching should saturate to a constant value at these voltages. This is not inconsistent with the data of Figure 5.6.

5.4.4 Physical model reproducing observed voltage dependence at all voltages

In fact, Equation (5.4) is an oversimplification. While it can predict the general trends of the observed i-V characteristics (highly voltage dependent, then linear, then saturated), it cannot explain why the linear parts of the i-V curves do not extrapolate to zero applied field at zero photocurrent. We believe that this discrepancy is a direct consequence of having a field dependent ionization efficiency at low voltages and of having blocking contacts. Were S constant, the i-V curves would simply be linear at low voltages and would saturate at high voltages when $G = 1$.

Blocking contacts lead to the accumulation of charge near each electrode. In the case of CdSe QDs, where it is believed that $\mu_n \tau_n > \mu_p \tau_p$, positive charge would build up near the cathode, as the electrons are swept out of the region adjacent to the cathode and the less mobile holes are left behind. In the reverse case, with $\mu_n \tau_n < \mu_p \tau_p$, negative charge will build up near the anode. Either case leads to a disproportionate amount of the applied voltage being dropped across the region where significant charge is accumulated. Goodman and Rose[41] use a simplified model for this problem for the case $\mu_n \tau_n < \mu_p \tau_p$. They assume that a photoconductor in a sandwich geometry is divided into three regions: near the anode (region 1), near the cathode (region 3), and in the center of the photoconductor (region 2). The widths of the regions near the anode and cathode are given by the mean drift length of the minority carrier (since it must be able to pass through each of the regions without recombining). Since $\mu_n \tau_n < \mu_p \tau_p$, negative charge builds up in region 1, and therefore a disproportionate amount of the applied voltage drops across this region. It is assumed that recombination does not occur in either region 1 or region 3, and that in region 2 recombination and generation are balanced. This

model is applicable for voltages below V_0, at which the current density saturates to value J_0. The current density and voltage variables, J and V, respectively, are converted to the dimensionless variables $j = J/J_0$, and $v = V/V_0$. The Goodman and Rose model predicts[41]

$$ j = \frac{(1+b)\{-b + [b^2 + 4(1-b)(1+b^2)v/(1+b)^2]^{1/2}\}}{2(1-b)} , \qquad (5.5) $$

where $b \equiv \dfrac{\mu_n \tau_n}{\mu_p \tau_p}$.

Equation (5.5) still holds true for the case in which $\mu_n \tau_n > \mu_p \tau_p$, except that the b in Equation (5.5) must be replaced with $\beta = 1/b$.

We modify the Goodman and Rose model to allow for field-dependent generation rates (i.e., ionization efficiencies) by allowing each of the three regions to have different generation rates, defined as g_1, g_2, and g_3. Furthermore, it is assumed that at saturation the generation rates in each region saturate to the same value, g_{sat}. This allows for a modification of Equation (5.5) as follows:

$$ j = \frac{\varepsilon_{1s}(1+b)\left\{-b\varepsilon_{12} + \left[b^2\varepsilon_{12}{}^2 + 4v(1+b^2)\left(1 - b\varepsilon_{12} + b^2\varepsilon_{13}{}^2 - b^2\varepsilon_{12}\varepsilon_{13}\right)/(1+b)^2\right]^{1/2}\right\}}{2\left(1 - b\varepsilon_{12} + b^2\varepsilon_{13}{}^2 - b^2\varepsilon_{12}\varepsilon_{13}\right)} , \quad (5.6) $$

where b is still defined as in Equation (5.6), and $\varepsilon_{1s} = \dfrac{g_1}{g_{sat}}$, $\varepsilon_{12} = \dfrac{g_1}{g_2}$, and $\varepsilon_{13} = \dfrac{g_1}{g_3}$. If $\varepsilon_{1s} = \varepsilon_{12} = \varepsilon_{13} = 1$, Equation (5.6) reduces to Equation (5.5).

It is assumed that the generation rate in each region follows the same field-dependence. Since we use our model only as a qualitative tool to understand the effect of field-dependent generation rates, a simple dependence that rises to a maximum is chosen:

$$ g(E) = g_{sat}(1 - \exp(-E/E_s)), \qquad (5.7) $$

where E_s defines how strongly the generation rate depends on field. Introducing field-dependent generation rates results in a problem that cannot be solved analytically, since the g_i depends on the field E_i in region i, and E_i depends on g_i. Instead, we solve the problem iteratively, using Equation (5.5) to determine starting values for E_1, E_2, and E_3, which in turn determines the starting values for g_1, g_2, and g_3. These are then used for the calculation of j at the subsequent voltage step.

The solid line in Figure 5.8 is the result of the iterative solution to Equation (5.6), given a value for b of 0.6 and $E_s = 0.7$ V_0/L. Because Equation (5.6) is not valid for $V > V_0$, we use a horizontal line to represent the photocurrent after saturation. The open circles in Figure 5.8 represent photocurrent data for a sample treated with butylamine and dried at 70 °C, with the current and voltage scaled for comparison. The j-V curve represented by the solid line in Figure 5.8 qualitatively reproduces the i-V curves of the amine- and base-treated samples: at low voltages, the photocurrent is highly voltage dependent, because of the voltage dependence of the generation rate; at voltages corresponding to $E > E_s$, the photocurrent becomes linear in voltage; and finally, at very high voltages the photocurrent saturates. In addition, the simulation shows that the non-zero voltage intercept of the linear region of the i-V curves is the result of having blocking electrodes that produce a build-up of positive charge near the cathode, and a field-dependent exciton ionization efficiency.

It also seems clear from the simulation that the $\mu\tau$ products for holes and electrons in films of CdSe QDs may not be as different from each other as has been previously proposed.[44] For values of b less than ~ 0.1, the simulated j-V curve displays $j \propto V^{1/2}$ behavior at voltages that are far lower than what is observed for Figure 5.1(b) and
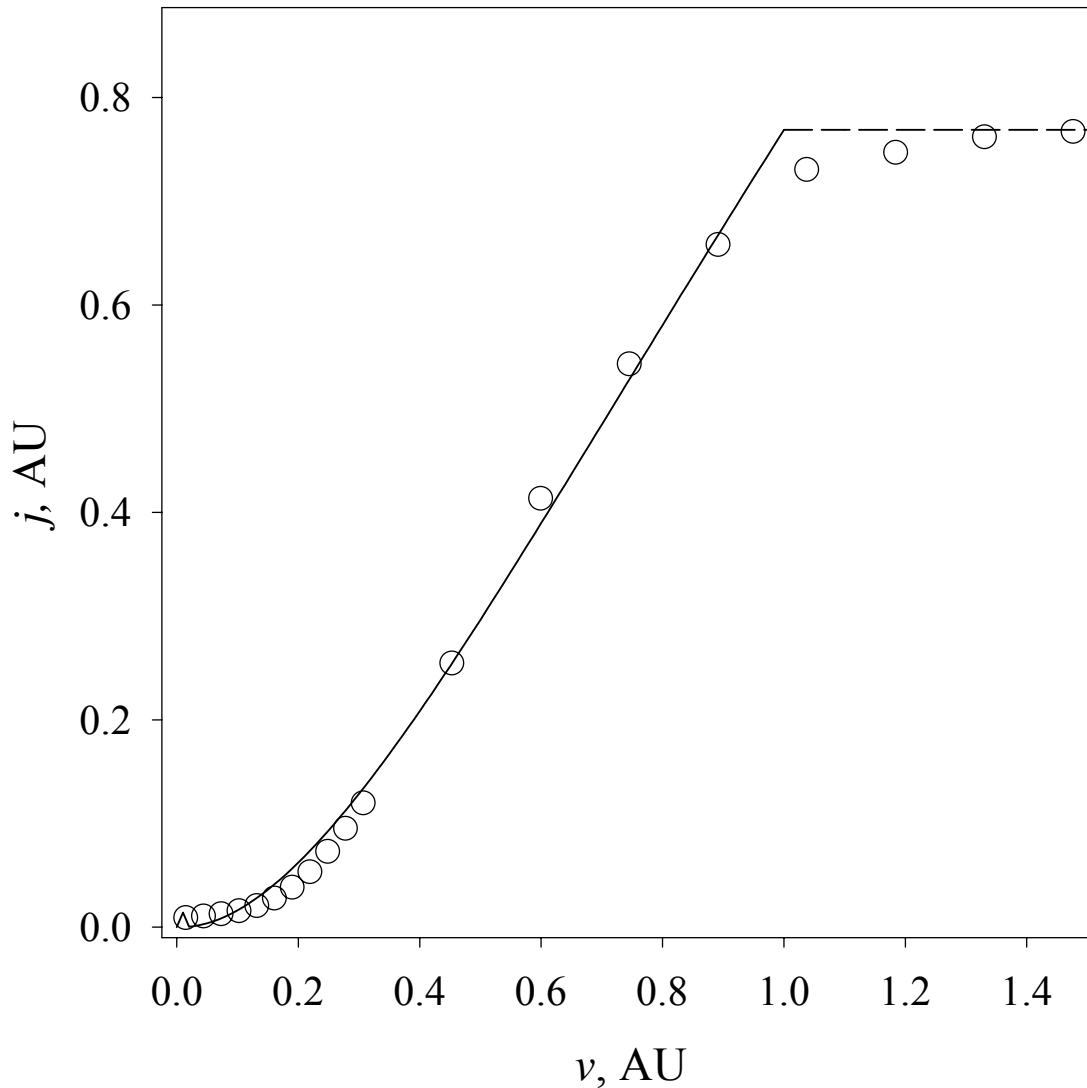
Figure 5.8: Simulation of the current-voltage characteristics (solid line) for a photoconductor in a sandwich structure with two mobile carriers, noninjecting electrodes, and a field-dependent generation rate. For this simulation, the field characterizing the generation rate saturation is set to 0.7 times the field characterizing the current saturation. The ratio of $\mu\tau$ for the two carriers is set to 0.6. The simulation breaks down at saturation, at which point the current is given by the horizontal dashed line. For comparison, photocurrent data (open circles) for a sample treated with butylamine and dried at 70 $^{\circ}$C are also presented. The current and voltage are scaled so that both are equal to one when the photocurrent saturates. The data is meant to be qualitatively compared to the simulation, since the simulation is not a result of a fit to the data.

Figure 5.3. This suggests that $\mu_n \tau_n$ probably does not exceed 10 times $\mu_p \tau_p$ in these films. It is not possible to determine whether this is also true for the other treated samples, since they do not exhibit saturation, and thus there is no reference voltage for a comparison to Figure 5.8.

However, even for the samples that do exhibit a clear saturation, one should be cautious when drawing quantitative conclusions from the simulation based on the Goodman and Rose model because there are a several limitations. First, the field dependence for the generation rate in Equation (5.7) is chosen for convenience, and is almost certainly much simpler than the actual field dependence. Second, the physics of the Goodman and Rose model is based on a photoconductor in a sandwich geometry, whereas the measurements presented here are for a planar geometry with a gate electrode. Third, the Goodman and Rose model simplifies the problem by defining three distinct regions within the photoconductor, when in reality the boundaries between the regions are not so abrupt. Nevertheless, the simulation provides important context for understanding the physics in our measurements.

5.4.5 Application of physical model to understanding treatment differences

The simulation also helps to explain the differences in the shapes of the *i-V* curves for the different types of samples measured. As E_s decreases, the simulated *j-V* curve represented by the solid line in Figure 5.8 shows that the transition to a linear regime also occurs at lower voltages. Comparing with experiment, this implies that unity ionization efficiency is achieved at lower voltages, for example for the sample treated with

butylamine followed by drying at 70 $^{\circ}$C than for the sample treated with butylamine and dried overnight.

The changes in the photocurrent behavior for the amine- and base-treated samples, compared to the reference samples, can now clearly be attributed to a substantial increase in the exciton ionization efficiency. The latter results from a competition between field ionization and recombination, radiative or nonradiative, within the QD. Thus, the ionization efficiency depends on both the exciton lifetime (with no applied voltage) and the distance between neighboring QDs, which influences the ionization rate.

The effect of distance is seen by comparing Figure 5.1(a), the sample treated with butylamine and dried overnight, and Figure 5.1(b), the sample treated with butylamine and dried at 70 $^{\circ}$C. The chemical treatment in each case is the same, so the main difference is that the QDs are ~7 Å apart for the sample in Figure 5.1(a), and only ~2 Å apart for the sample in Figure 5.1(b). Bringing the QDs closer together increases the rate of electron tunneling between QDs and therefore increases the ionization efficiency.

The effect of exciton lifetime (with no applied field) can be seen by comparing Figure 5.1(a), the sample treated with butylamine and dried overnight, and Figure 5.1(c), the sample treated with tri-*n*-butylphosphine (TBP). In each case, the QD spacing is approximately the same, so the main difference is the functionality of the reagent used for treatment. Amines (and a basic environment in general) are known to increase quantum yield[25, 35-39] by decreasing the rate of non-radiative exciton recombination through surface passivation. Since decreasing the rate of non-radiative exciton recombination makes the rate of ionization more competitive, it also increases the ionization efficiency.

Comparing the *i-V* curves in Figures 5.1(a) and 5.2(a-c) confirms the above assertions. AFM analysis suggests that the QD spacing after treatment with butylamine (dried overnight; Figure 5.1(a)), aniline (Figure 5.2(b)), and 1,4-phenylenediamine (Figure 5.2(c)) are all ~ 5- 7 Å. The fact that all of these treatments result in similar improvements in photoconductivity and similar changes in the shapes of the *i-V* curves confirm that these effects are predominantly the result of the passivating nature of the amine functionality. Whether or not the amines used for treatment are conjugated or are diamines capable of cross-linking does not appear to have a strong effect. As expected, treatment with 1,6-diaminohexane results in a similar *i-V* curve that reaches a linear regime at slightly lower voltage than the other amine treatments, since the QD spacing is reduced to ~ 3- 5 Å.

Previous studies[26] have shown that the photoconductivity in CdSe QD films decreases with increasing temperature. This has been attributed to the increase in the non-radiative exciton recombination rate at higher temperatures, which leads to a decrease in exciton ionization efficiency for a given voltage. Figure 5.7(a) shows that the photocurrent for a reference sample at 100V is more than 30 times smaller at 300 K than it is at 77 K, consistent with previous observations. Figure 5.7(b) shows that the photocurrent at 100 V for a sample treated with butylamine and dried at 70 °C is only about 5 times smaller at 300 K than it is at 77 K. The weaker dependence of the photocurrent on temperature as well as the relative shapes of the *i-V* curves at 77 K and 300 K for the treated sample are consistent with the above model. Because of the increase in the non-radiative exciton recombination rate at 300 K, the *i-V* curve of the treated sample enters the linear regime, indicative of unity ionization efficiency, at a

higher voltage at 300 K than at 77 K. Furthermore, while the treated *i-V* curve at 77 K

saturates at 100 V, saturation is not observed at 300 K. This is because the photocurrent

at 300 K is not as high as at 77 K, and according to Equation (5.2) saturation should

occur at a given current rather than a given voltage, independent of temperature.

5.5 Conclusions

Photoconductivity of CdSe QD films can be increased by post-deposition

treatment with butylamine, aniline, 1,6-diaminohexane, 1,4-phenylenediamine, tri-*n*-

butylphosphine, and sodium hydroxide. The *i-V* characteristics of the films after

treatment confirm that the mechanism for improvement is an increase in the exciton

ionization efficiency, which is achieved by increased QD surface passivation (due to the

basic nature of amines and sodium hydroxide) and decreased QD spacing. For treatment

with all of the amines and with sodium hydroxide, unity exciton ionization efficiency is

attained. Furthermore, after treatment with sodium hydroxide or butylamine (when the

sample is dried in the oven), the QD spacing is reduced enough for the photoconductivity

to saturate at high voltage. This saturation is consistent with a model in which the

electron lifetime becomes transit-time limited because there are two mobile carriers that

are not replenished at the electrodes. We have presented a model that qualitatively

reproduces the *i-V* characteristics of the amine- and base-treated samples by assuming

blocking contacts and field-dependent generation rates (i.e., ionization efficiencies) that

saturate at a voltage below the voltage necessary for photocurrent saturation.

These results and conclusions have important consequences for the potential use

of CdSe QDs for opto-electronic applications such as photodetectors or solar cells. In

addition to providing a method for achieving significant photocurrent at 77K and room temperature for the first time, our results imply that photocurrent cannot be increased further unless electron and hole injection from the electrodes is facilitated. Potential methods to aid in carrier injection include: using a lower work function metal for the electrodes (for instance calcium or aluminum); converting from a lateral to a vertical structure so that another semiconductor could be introduced between the QDs and the electrodes in order to produce a gradient for electron and hole injection; and choosing another type of semiconductor QD with conduction and valence levels that align more favorably with the work function of gold.

5.6 References

1. M. Dahan, S. Levi, C. Luccardini, P. Rostaing, B. Riveau, and A. Triller, "Diffusion dynamics of glycine receptors revealed by single-quantum dot tracking," Science **302**(5644), 442-445 (2003).

2. D. R. Larson, W. R. Zipfel, R. M. Williams, S. W. Clark, M. P. Bruchez, F. W. Wise, and W. W. Webb, "Water-soluble quantum dots for multiphoton fluorescence imaging in vivo," Science **300**(5624), 1434-1437 (2003).

3. J. K. Jaiswal, H. Mattoussi, J. M. Mauro, and S. M. Simon, "Long-term multiple color imaging of live cells using quantum dot bioconjugates," Nature Biotechnology **21**(1), 47-51 (2003).

4. B. Dubertret, P. Skourides, D. J. Norris, V. Noireaux, A. H. Brivanlou, and A. Libchaber, "In vivo imaging of quantum dots encapsulated in phospholipid micelles," Science **298**(5599), 1759-1762 (2002).

5. S. Kim, Y. T. Lim, E. G. Soltesz, A. M. De Grand, J. Lee, A. Nakayama, J. A. Parker, T. Mihaljevic, R. G. Laurence, D. M. Dor, L. H. Cohn, M. G. Bawendi, and J. V. Frangioni, "Near-infrared fluorescent type II quantum dots for sentinel lymph node mapping," Nature Biotechnology **22**(1), 93-97 (2004).

6. S. Coe-Sullivan, W. K. Woo, J. S. Steckel, M. Bawendi, and V. Bulovic, "Tuning the performance of hybrid organic/inorganic quantum dot light-emitting devices," Organic Electronics **4**(2-3), 123-130 (2003).

7. S. Coe, W. K. Woo, M. G. Bawendi, and V. Bulovic, "Electroluminescence from single monolayers of nanocrystals in molecular organic devices," Nature **420**(6917), 800-803 (2002).

8. V. L. Colvin, M. C. Schlamp, and A. P. Alivisatos, "Light-Emitting-Diodes Made from Cadmium Selenide Nanocrystals and a Semiconducting Polymer," Nature **370**(6488), 354-357 (1994).

9. B. O. Dabbousi, M. G. Bawendi, O. Onitsuka, and M. F. Rubner, "Electroluminescence from Cdse Quantum-Dot Polymer Composites," Applied Physics Letters **66**(11), 1316-1318 (1995).

10. W. U. Huynh, J. J. Dittmer, N. Teclemariam, D. J. Milliron, A. P. Alivisatos, and K. W. J. Barnham, "Charge transport in hybrid nanorod-polymer composite photovoltaic cells," Physical Review B **67**(11), art. no. 115326 (2003).

11. W. U. Huynh, J. J. Dittmer, and A. P. Alivisatos, "Hybrid nanorod-polymer solar cells," Science **295**(5564), 2425-2427 (2002).

12. A. J. Nozik, "Quantum dot solar cells," Physica E **14**(1-2), 115-120 (2002).

13. P. Bhattacharya, A. D. Stiff-Roberts, S. Krishna, and S. Kennerly, "Quantum dot infrared detectors and sources," International Journal of High Speed Electronics and Systems **12**(4), 969-994 (2002).

14. L. W. Ji, Y. K. Su, S. J. Chang, S. H. Liu, C. K. Wang, S. T. Tsai, T. H. Fang, L. W. Wu, and Q. K. Xue, "InGaN quantum dot photodetectors," Solid-State Electronics **47**(10), 1753-1756 (2003).

15. H.-J. Eisler, V. C. Sundar, M. G. Bawendi, M. Walsh, H. I. Smith, and V. Klimov, "Color-selective semiconductor nanocrystal laser," Applied Physics Letters **80**(24), 4614-4616 (2002).

16.   V. C. Sundar, H.-J. Eisler, and M. G. Bawendi, "Room-temperature, tunable gain media from novel II-VI nanocrystal-titania composite matrices," Advanced Materials **14**(10), 739-743 (2002).

17.   M. Nirmal, B. O. Dabbousi, M. G. Bawendi, J. J. Macklin, J. K. Trautman, T. D. Harris, and L. E. Brus, "Fluorescence intermittency in single cadmium selenide nanocrystals," Nature **383**, 802-804 (1996).

18.   W. K. Woo, K. T. Shimizu, M. V. Jarosz, R. G. Neuhauser, C. A. Leatherdale, M. A. Rubner, and M. G. Bawendi, "Reversible Charging of CdSe Nanocrystals in a Simple Solid State Device," Advanced Materials **14**(15), 1068-1071 (2002).

19.   M. Shim, C. J. Wang, and P. Guyot-Sionnest, "Charge-tunable optical properties in colloidal semiconductor nanocrystals," Journal of Physical Chemistry B **105**(12), 2369-2373 (2001).

20.   C. J. Wang, M. Shim, and P. Guyot-Sionnest, "Electrochromic nanocrystal quantum dots," Science **291**(5512), 2390-2392 (2001).

21.   M. A. Kastner, "Artificial Atoms," Physics Today **46**(24), 24-31 (1993).

22.   M. Drndic, M. V. Jarosz, N. Y. Morgan, M. A. Kastner, and M. G. Bawendi, "Transport properties of annealed CdSe colloidal nanocrystal solids," Journal of Applied Physics **92**(12), 7498-7503 (2002).

23.   P. Guyot-Sionnest and C. Wang, "Fast voltammetric and electrochromic response of semiconductor nanocrystal thin films," Journal of Physical Chemistry B **107**(30), 7355-7359 (2003).

24.   D. Yu, C. J. Wang, and P. Guyot-Sionnest, "n-type conducting CdSe nanocrystal solids," Science **300**(5623), 1277-1280 (2003).

25.   B. K. H. Yen, N. E. Stott, K. F. Jensen, and M. G. Bawendi, "A continuous-flow microcapillary reactor for the preparation of a size series of CdSe nanocrystals," Advanced Materials **15**(21), 1858-1862 (2003).

26.   C. A. Leatherdale, C. R. Kagan, N. Y. Morgan, S. A. Empedocles, M. A. Kastner, and M. G. Bawendi, "Photoconductivity in CdSe quantum dot solids," Physical Review B **62**(4), 2669-2680 (2000).

27.   C. B. Murray, D. J. Norris, and M. G. Bawendi, "Synthesis and characterization of nearly monodisperse CdE (E = S, Se, Te) semiconductor nanocrystallites," Journal of the American Chemical Society **115**(19), 8706-8715 (1993).

28.   C. B. Murray, C. R. Kagan, and M. G. Bawendi, "Self-Organization of Cdse Nanocrystallites into 3-Dimensional Quantum-Dot Superlattices," Science **270**(5240), 1335-1338 (1995).

29.   C. B. Murray, C. R. Kagan, and M. G. Bawendi, "Synthesis and characterization of monodisperse nanocrystals and close-packed nanocrystal assemblies," Annual Review of Materials Science **30**, 545-610 (2000).

30.   M. V. Jarosz, N. E. Stott, M. Drndic, N. Y. Morgan, M. A. Kastner, and M. G. Bawendi, "Observation of bimolecular carrier recombination dynamics in close-packed films of colloidal CdSe nanocrystals," Journal of Physical Chemistry B **107**(46), 12585-12588 (2003).

31.   C. R. Kagan, C. B. Murray, and M. G. Bawendi, "Long-range resonance transfer of electronic excitations in close-packed CdSe quantum-dot solids," Physical Review B **54**(12), 8633-8643 (1996).

32.   C. R. Kagan, C. B. Murray, M. Nirmal, and M. G. Bawendi, "Electronic energy transfer in CdSe quantum dot solids," Physical Review Letters **76**(9), 1517-1520 (1996).

33.   N. Y. Morgan, C. A. Leatherdale, M. Drndic, M. V. Jarosz, M. A. Kastner, and M. Bawendi, "Electronic transport in films of colloidal CdSe nanocrystals," Physical Review B **66**(7)(2002).

34.   C. Kagan, "The Electronic and Optical Properties of Close Packed Cadmium Selenide Quantum Dot Solids," (Massachusetts Institute of Technology, Cambride, 1996).

35.   L. Spanhel, M. Haase, H. Weller, and A. Henglein, "Photochemistry of Colloidal Semiconductors .20. Surface Modification and Stability of Strong Luminescing Cds Particles," Journal of the American Chemical Society **109**(19), 5649-5655 (1987).

36.   D. V. Talapin, A. L. Rogach, I. Mekis, S. Haubold, A. Kornowski, M. Haase, and H. Weller, "Synthesis and surface modification of amino-stabilized CdSe, CdTe and InP nanocrystals," Colloids and Surfaces a-Physicochemical and Engineering Aspects **202**(2-3), 145-154 (2002).

37.   W.-K. Woo, "Fabrication and Characterization of Quantum-Confined Optoelectronic Devices Based on CdSe Nanocrystals," (Ph. D. Thesis, Massachusetts Institute of Technology, Cambridge, MA, 2002).

38.   X. G. Peng, M. C. Schlamp, A. V. Kadavanich, and A. P. Alivisatos, "Epitaxial growth of highly luminescent CdSe/CdS core/shell nanocrystals with photostability and electronic accessibility," Journal of the American Chemical Society **119**(30), 7019-7029 (1997).

39.   D. V. Talapin, A. L. Rogach, A. Kornowski, M. Haase, and H. Weller, "Highly luminescent monodisperse CdSe and CdSe/ZnS nanocrystals synthesized in a hexadecylamine-trioctylphosphine oxide-trioctylphospine mixture," Nano Letters **1**(4), 207-211 (2001).

40.   R. H. Bube, *Photoconductivity of Solids* (Wiley, New York, 1960).

41.   A. M. Goodman and A. Rose, "Double extraction of uniformly generated electron-hole pairs from insulators with noninjecting contact," Journal of Applied Physics **42**(7), 2823-2830 (1971).

42.   A. Rose, *Concepts in Photoconductivity and Allied Problems*, Interscience Tracts on Physics and Astronomy (Interscience Publishers, London, 1963).

43.   F. C. Nix, "Photo-conductivity," Reviews of Modern Physics **4**, 723-766 (1932).

44.   D. S. Ginger and N. C. Greenham, "Charge injection and transport in films of CdSe nanocrystals," Journal of Applied Physics **87**(3), 1361-1368 (2000).

45.   H. Mattoussi, L. H. Radzilowski, B. O. Dabbousi, E. L. Thomas, M. G. Bawendi, and M. F. Rubner, "Electroluminescence from heterostructures of poly(phenylene vinylene) and inorganic CdSe nanocrystals," Journal of Applied Physics **83**(12), 7965-7974 (1998).

Chapter 6

Concluding Remarks

The work presented in this thesis is the result of what began as an effort to increase the photoconductivity of CdSe QD solids. This is an important goal from the stand-point of bringing the promise of QD opto-electronic devices into reality. Clearly, higher photo- and dark conductivities are a big step towards enabling the use of CdSe QDs in devices such as solar cells, light emitting diodes, photodetectors, and maybe one day electrically pumped (or at least electrically assisted) tunable QD lasers.

While these goals are important on their own, the work in this thesis is also significant for what it contributes to our understanding of the optical and electronic properties of CdSe QDs. In order to improve the conduction of CdSe QD solids, it became very important to understand more about the physics of QDs so that factors limiting their conductivity could be identified. The feedback between chemistry and physics was very strong: good chemistry was required to learn more about QD physics, and what was learned about the QD physics enabled improvements in QD and film chemistry.

Chapters 2 – 5 of this thesis represent an increasing level of understanding of and control over the opto-electronic properties of CdSe QDs. In our first efforts to increase conductivity, described in Chapter 2, we began by annealing QD films at temperatures up to 430 $^{\circ}$C. This proves to increase both dark and photoconductivity substantially, which

is attributed to enhanced interdot tunneling. However, steady state dark current is still not observed, and so it is concluded that Coulomb interactions between electrons on neighboring dots continue to play an important role in the electronic transport. Unfortunately, this method of enhancing conductivity is somewhat crude, in that it is difficult to explain exactly what kind of chemical is left between the QDs after the TOP/TOPO caps have been incinerated.

The need to better understand and control the chemistry of QDs and QD films is emphasized in Chapter 3. That work describes what needs to be done in order to enable photoconductivity studies of CdSe QDs synthesized using new methods (based on replacing dimethylcadmium with a cadmium salt, $Cd(acac)_2$). During this work, it became very clear that not all QDs are the same in the context of photoconductivity studies. It is very important to understand and control the quality of both the chemicals used to synthesize the QDs, as well as the chemistry used to make the final desired product (in this case, a film of close-packed CdSe QDs).

The methods developed in Chapter 3 made the work in Chapter 4 possible. In that chapter, we show how a high level of control over the chemistry of CdSe QDs can lead to the observation of a new regime of physics. For CdSe QDs synthesized with $Cd(acac)_2$ and prepared according to the methods of Chapter 3, the photoconductivity behavior is characterized by a low density of trapped charges. This is in contrast to previous results on films of QDs synthesized using dimethylcadmium, which exhibit photoconduction consistent with a density of trapped charges that is much higher than the density of charge carriers.

Chapter 5 continues the theme of using controlled chemistry to enable a new regime, and a further understanding, of QD physics. By using chemistry to decrease both the interdot spacing and the nonradiative exciton decay rate, we present CdSe QD films that have current-voltage characteristics that are consistent with achieving a saturated (unity) exciton separation efficiency. Because of reaching this new regime of CdSe QD photoconduction, we also are able to understand that the gold electrodes in our inverted FET structure are able to extract both holes and electrons, but they are unable to inject either of them. In addition, these results show that there is no barrier to charge extraction. This means that injection from the contacts is difficult because of energetics and not because of a large (or wide) tunnel barrier to injection. This finding has important consequences for further photoconductivity and dark conductivity studies of QD films, in particular with regards to the design of appropriate test device structures.

Appendix: Reversible QD Charging[*]

The physical and chemical properties of colloidal semiconductor nanocrystal (NC) quantum dots are being extensively explored for their potential applications in a variety of fields. The application of these NCs into novel optoelectronic, nanoelectronic, and biological applications could be significantly enhanced by understanding the physical processes that can controllably and reversibly modify their properties. One possibility to drastically change NC electrical and optical properties is by charging them.[1,2] Hence, there is a growing interest in preparing stable, charged NCs.[3,4] We report a novel, solid-state, thin-film device that allows reversible switching of NCs between charged (both positive or negative) and uncharged states at room temperature with a high degree of reproducibility and stability. Reversible fluorescence quenching and absorption bleaching of NCs are directly observed. Our basic design can be scaled both down to the sub-micron scale, and up to macroscopic scales, indicating the feasibility of using NCs as the active material in optical modulators and in tunable fluorescent or photochromic displays.

Theory dating back to early photodarkening experiments describes a charged NC as a "dark" NC.[5] Essentially, a free electron (or hole) in the NC core quenches the photoluminescence through Auger recombination — a non-radiative exciton annihilation process involving three particles: Two particles (an electron and a hole) recombine, and the recombination energy is transferred to a third particle that can be either an electron or

---

a hole. The phenomenon of fluorescence intermittency of single NCs,[6] where individual

NCs emit light intermittently, randomly turning "on" and "off" under continuous light

excitation, is explained by a similar model.[7] Specifically, a NC turns "off" when the NC

core is charged and it turns back "on" when the core is no longer charged. We fabricate a

simple solid-state device that enables us to validate this Auger model for "dark" NCs and

observe the phenomenon directly on an ensemble of NCs. Charged NCs in solution

phase have also been recently prepared using an electrochemical approach[4] with similarly

consistent results. Studies to understand the electronic properties of charged zero-

dimensional quantum-confined structures grown using molecular-beam epitaxy or

chemical-vapor deposition[8-10] have also shown that control of charge can lead to drastic

changes in properties and the development of important physical insight. These

structures are generally in the weak quantum confinement regime compared to NCs and

their surface chemistry is that of an epitaxial interface. Here, we investigate charging

effects in dense solids of colloidal NCs that exhibit strong quantum confinement

properties, with a surface chemistry that is dominated by organic ligands, and with

conductivity properties dominated by tunnel junctions between NCs created by the

organic ligand.

Our device consists of an insulating polymer layer and a thin, spin-coated NC

layer sandwiched between two electrodes [Figure A.1(a)]. We use a layer-by-layer

deposition technique to cast the polyelectrolytes poly(allylamine hydrochloride) (PAH)

and poly(acrylic acid) (PAA) sequentially onto an indium-tin oxide (ITO) electrode. This

simple technique allows the fabrication of highly uniform thin films with precisely

controlled thickness and chemical composition over a large area.[11] The resistivity of
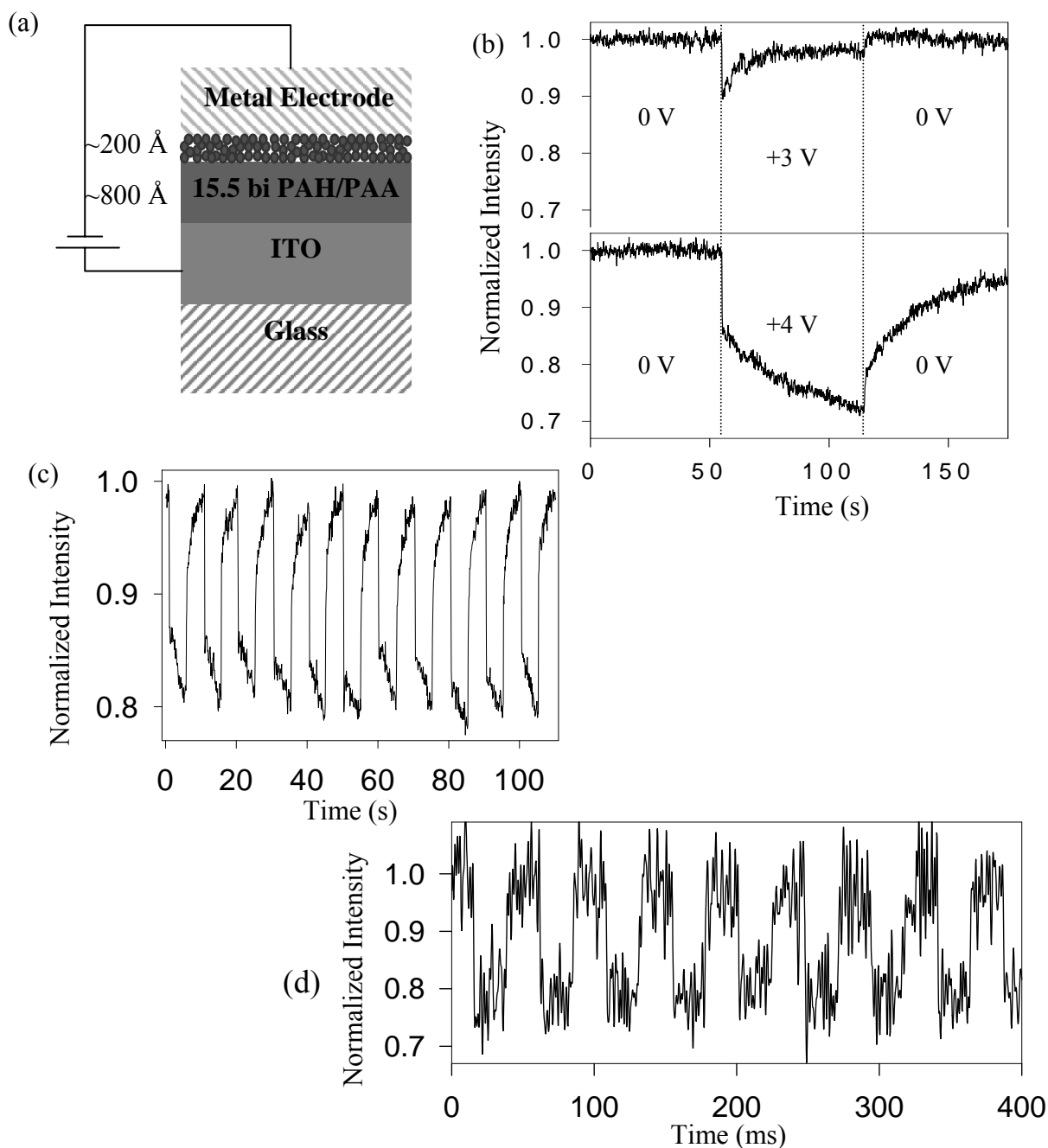
Figure A.1: Schematic diagram of the NC charging device. The insulating layer consists of 15.5 bilayers of PAH/PAA with the PAH layer on top. The ITO serves as a transparent electrode for photoluminescence measurements through an optical microscope. The excitation source consists of a CW Ar ion laser (514 nm, 50 W/cm^2) and the photoluminescence (PL) is detected by a CCD camera. Typical working pixel area is 6 mm^2 with eight pixels per device. (b): The charging time-traces for bare, 2.2 nm radius, CdSe NCs with (top) 3 x 10^5 V/cm and (bottom) 4 x 10^5 V/cm. (c): Photostability of the device is evidenced by the recovery of the photoluminescence intensity after the charge/discharge cycling of the voltage sequence. (d): Fast charging and discharging times of a CdSe NC charging device operating under the critical voltage.

these PAH/PAA thin films (10^{12} $\Omega \cdot$cm)[12] is comparable to those of inorganic films, but without the expensive, complex equipment, and highly stringent conditions generally required for the deposition of inorganic films. The PAH/PAA films are deposited from polyelectrolyte solutions with pH 4.5 to produce dense and highly interpenetrated films.[13] The PAH/PAA films are then cross-linked via heat-induced amide formation between the NH_3^+ groups of PAH and the COO^- groups of PAA in order to further enhance the film stability.[14] Three to four layers of NCs, are then spin-coated on top of the PAH/PAA film. The NCs are either "bare" CdSe NCs that consist of a core CdSe particle surrounded by an organic ligand shell, or "core-shell" CdSe(ZnS) NCs that consist of a core CdSe particle surrounded by thin (few monolayers) shell of ZnS followed by the organic ligands. The NCs are prepared using previously described methods.[15-17] Finally, an aluminum electrode is deposited.

In all of our experiments, the aluminum electrode is grounded and the ITO electrode is connected to the applied voltage. By applying a sufficient electric field, the Fermi energy level of the aluminum electrode aligns with the energy levels of the NCs and the charge carriers are injected into or extracted out of the NCs. The magnitude and direction of the applied field dictate the nature of the carriers (electrons or holes) and the charging process (injection or extraction). In this letter, we focus mainly on injection of electrons into NCs when a sufficiently large, positive voltage is applied – a NC capacitor storing electrons. We show that holes can also be injected when the applied voltage is sufficiently negative.

In Figure A.1(b), the relationship between the CdSe NC fluorescence and different applied voltages are shown. The field strengths used in the top and the bottom

experiments are 3 x 10^5 V/cm and 4 x 10^5 V/cm, respectively. While individual NCs arbitrarily turn "on" and "off", an equilibrium exists for an ensemble and the ensemble fluorescence remains constant. Immediately after applying a positive voltage, we observe a fast drop in the fluorescence within the first 100 ms for both applied voltages. This initial darkening effect is most likely caused by field-assisted photoionization of carriers out of the NCs[18] and its magnitude increases with the excitation intensity. These events not only impede the radiative recombination of the electron-hole pairs, but also leave NCs charged (dark). Depending on the magnitude of the applied field, the fluorescence then either recovers or decays further on a slower time scale. In order to inject electrons from the electrode into the NCs, the applied field (positive voltage) must raise the Fermi level of the aluminum above the lowest unoccupied energy level of the NCs. That is we expect a critical voltage below which no injection is likely. A field strength of 3 x 10^5 V/cm is not sufficient to inject electrons from the electrode into the NCs, and the fluorescence quenching stops after the initial drop due to photoionization [Figure A.1(b)]. The fluorescence recovers as charge carriers migrate to screen the external field and the excitation light discharges the NCs through Auger processes. Although the recovery process is slow in the presence of the applied voltage, the fluorescence fully recovers once the applied voltage is turned off.

When the field strength exceeds 4 x 10^5 V/cm, injection of electrons occurs and the fluorescence is further quenched after the initial fast drop [Figure A.1(b)]. As electrons migrate by a slow hopping[18] from charged NCs to uncharged ones, a slow decay in fluorescence results. After the voltage is turned off, the fluorescence shows an initial, fast recovery step and then gradually recovers completely. Clearly, there are
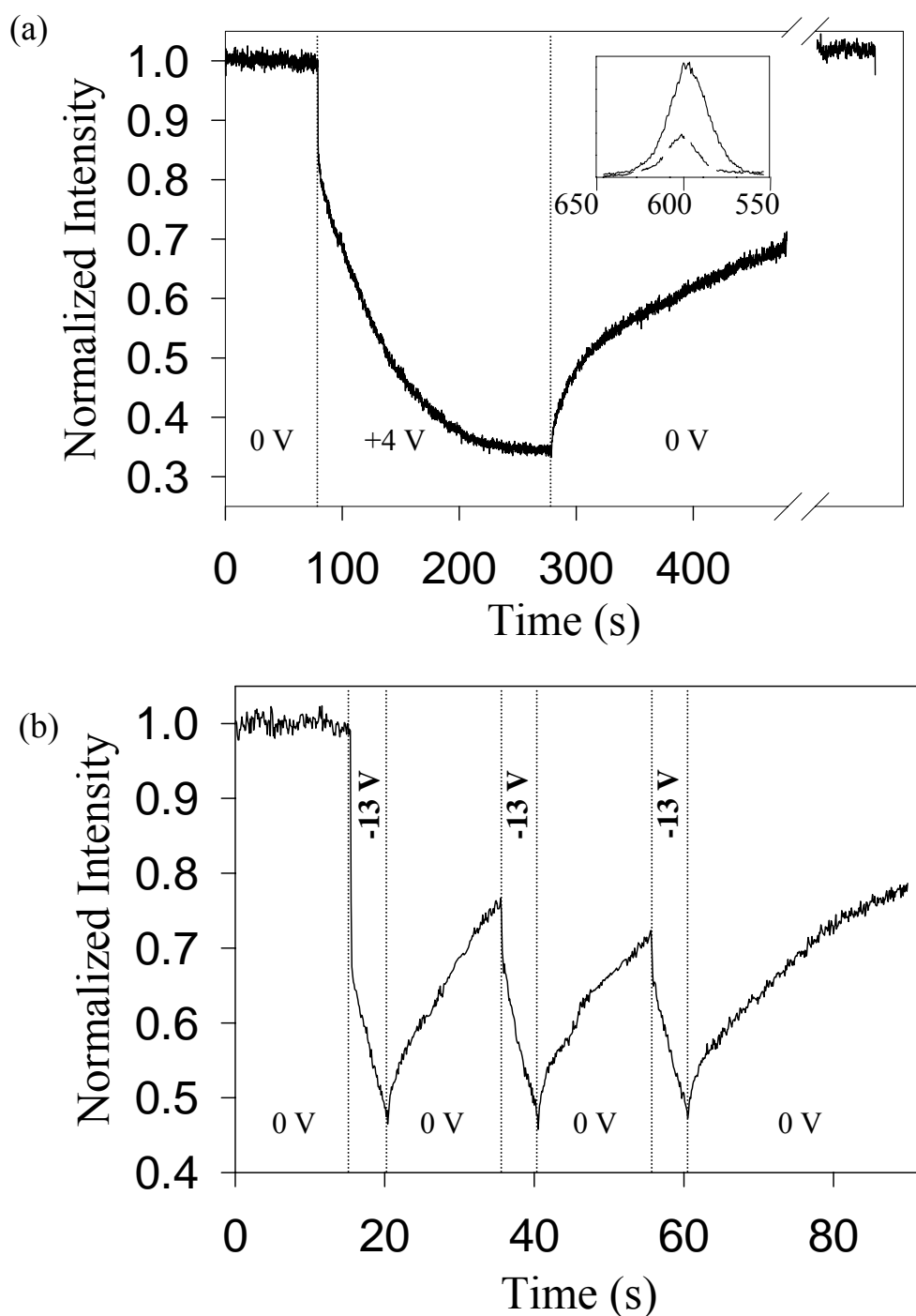
Figure A.2: By sufficient charge injection, the PL is quenched by ~70% after 200 s. The PL recovery is complete after 400s at zero field. The spectral data are shown in the inset immediately before the field is turned on (solid line) and before the field is turned off (dashed line). (b): Applying the appropriate negative voltage, hole injection also quenches the PL. Hole injection into the NC does not change the stability of the NCs or the device. The PL recovers completely after ~60 s.

differences between the charging and the discharging process. First, the magnitude of the initial recovery is considerably smaller than the magnitude of the initial fast drop induced by applying the voltage. Second, a complete discharging process (fluorescence fully recovered) usually takes more time than the charging process. One possible reason is that the surface states of the NCs are also being filled with electrons while the NCs are being charged. The number of vacant states for transporting electrons between the NCs and the electrode during the discharging process may be smaller than during the charging process. The discharging recovery time is usually on the order of seconds to a few minutes longer than the charging time when the NCs are under continuous light excitation with no applied voltage [Figure A.2(a)] (the time depends on the degree of quenching).

For potential applications of these nanocrystal capacitor structures as optical modulator or in displays, the stability and the response times of the charging structure are important issues that are addressed in Figures A.1(c) and A.1(d). As the device is cycled between zero and positive bias, the recovering fluorescence suggests that the charging/discharging process does not cause degradation to the NCs. Although the time frame in Figure A.1(c) is in the tens of seconds, the device can be operated at room temperature for tens of hours and similar stability has been demonstrated. In Figure A.1(d), a device operating below the critical voltage is shown. The fluorescence intensity responds approximately as a step function with a modulation of ~25-30% and with both charging and discharging times shorter than 200 µs. Preliminary data indicates that these times are probably faster than 10 µs.

The charging device can reversibly quench the fluorescence of the CdSe NCs up to ~65-75% [Figure A.2(a)]. The possible reasons for the saturation are (1) a number of

NCs are continuously discharged by Auger processes through excitons generated by the excitation light, and (2) as more NCs are charged, this screens the remaining uncharged NCs and effectively makes the charging process more difficult. Consequently, a dynamic equilibrium is reached and the quenching saturates.

Figure A.2(b) shows that holes can also be injected into the NCs at a sufficiently large, applied negative voltage. The separation between the highest occupied energy level of the NC and the Fermi level of aluminum is expected to be larger than the separation between the Fermi level and the lowest unoccupied energy level.[19] Thus, a larger field strength (1.3×10^6 V/cm) is necessary to initiate the hole injection process. The fluorescence in Figure A.2(b) does not fully recover between the voltage pulses as the recovery time is insufficient. Approximately one minute is required in this device for the fluorescence to recover after the end of the cycling experiment. This strongly indicates that hole-rich NCs are unchanged even after an "oxidation" process. As both electron-rich and hole-rich NCs can be readily prepared with the same device, we can also cycle the NCs between these two "oxidation" states.

The effect of a ZnS overcoat on CdSe NCs at a given applied voltage can be observed when comparing Figure A.3(a) with Figure A.2(a). As the NCs are coated by a ZnS shell of ~1 nm thickness which forms a tunnel barrier for injection of electrons and holes into the CdSe core, the probability of injecting charges into the NC is significantly reduced[17-19]. Our attempts to charge ZnS overcoated NCs and "bare" NCs using the same applied field clearly illustrate this [Figure A.3(a)]. Although slightly diminished due to the overcoating, the applied field still assists the tunneling of photoexcited carriers from the NC cores to the core/shell interfaces and causes the initial drop in the fluorescence.
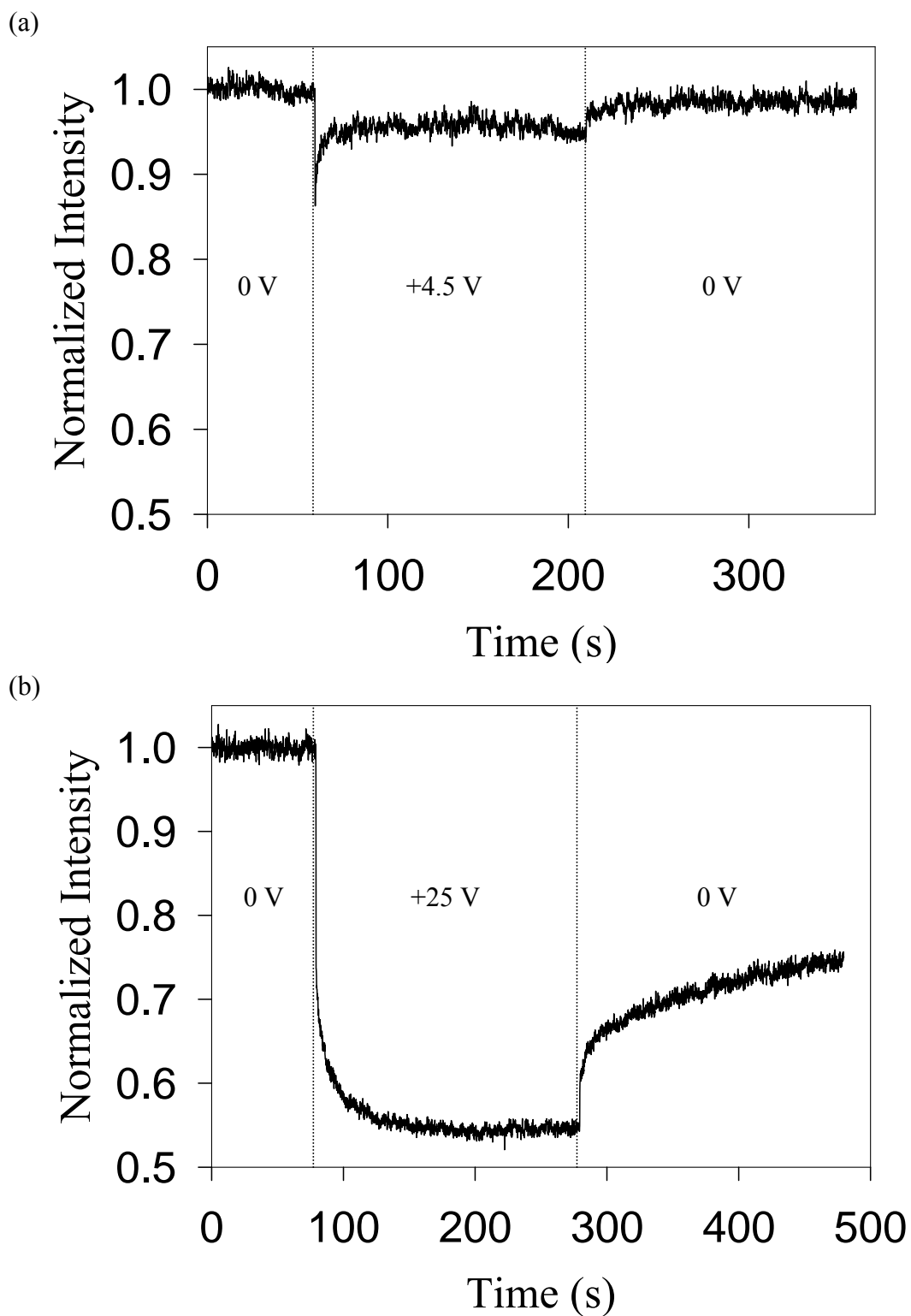
172

(a)

(b)

Figure A.3: For ZnS overcoated NCs, the threshold for charge injection is higher than for the bare samples. The previous threshold of (a) 4×10^5 V/cm is insufficient to charge the overcoated NCs; charge injection is observed at (b) 2.2×10^6 V/cm.
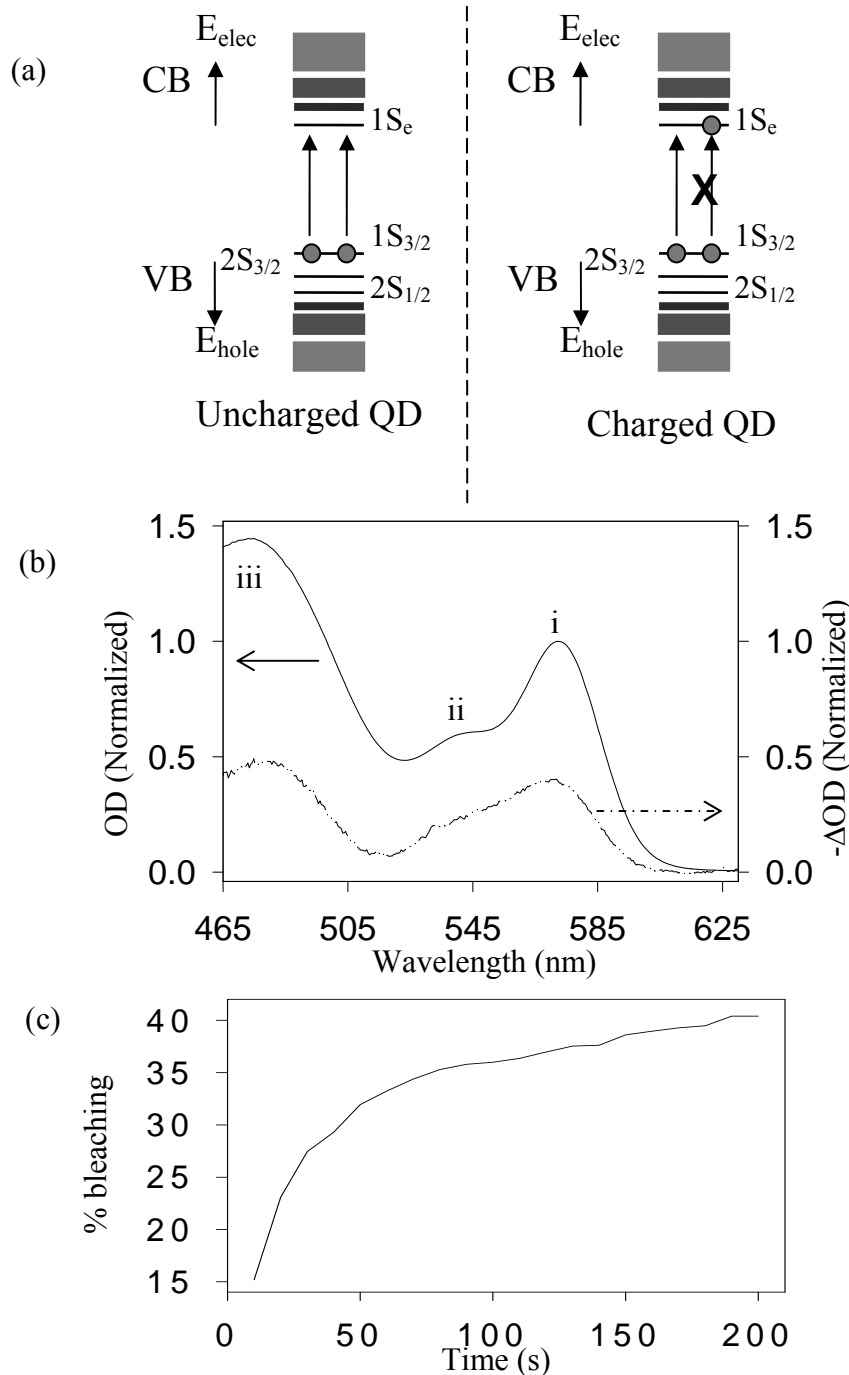
Figure A.4: Absorption bleaching in charged NCs. (a): A ~50% decrease in the transition probability for transitions to the $1S_e$ state ($1S_{3/2} \rightarrow 1S_e$, $2S_{3/2} \rightarrow 1S_e$, $2S_{1/2} \rightarrow 1S_e$, ...) is predicted for a charged NC according to the Pauli exclusion principle. (b): The upper spectrum (solid line) shows the absorption spectrum from a solution of the NCs making up the film. The lower spectrum (dashed line) is the difference spectrum for absorption $[-\Delta OD = OD(\text{neutral}) - OD(\text{charged})]$ taken from the NC charging device. Specific electronic transitions to the ground state (i) $1S_{3/2}1S_e$, (ii) $2S_{3/2}1S_e$, (iii) $2S_{1/2}1S_e$ are labeled accordingly. (c): The time dependent change in the percentage bleaching of the $1S_{3/2}1S_e$ state is shown to saturate near a maximum of 40%.

However, the subsequent injection of electrons from the aluminum into the overcoated NCs fails unless an even higher field is applied. The critical field for the injection of electrons into the overcoated NCs is about 1.2 - 1.3 x 10^6 V/cm. The fluorescence of the overcoated NCs can be reversibly quenched to only 45% even when the applied field strength is as high as 2.2 x 10^6 V/cm [Figure A.3(b)]. A relatively fast saturation is also observed. All these indicate an inefficient charging process and a dynamic competition between charge injection through the ZnS layer and photo-assisted discharging of core carriers into interface trap states.

The device also allows us to reversibly bleach the absorption of the CdSe NCs. Since the injected electrons should reside in the $1S_e$ state of the NCs, the probability of absorbing into this state from underlying hole states is reduced by half [Figure A.4(a)]. If every NC has one excess electron, all transitions involving the $1S_e$ state should be bleached by 50%. The difference absorption spectra taken between the uncharged and charged state (-ΔOD) is shown in Figure A.4(b). We can clearly see that all transitions involving the $1S_e$ state ($1S_{3/2}{\rightarrow}1S_e$, $2S_{3/2}{\rightarrow}1S_e$, $2S_{1/2}{\rightarrow}1S_e$, …), shown in the solution absorption spectrum of the same NC sample, are bleached. Figure A.4(c) shows the percentage-bleaching time trace of the $1S_{3/2}1S_e$ transition; the reversible bleaching is as much as 40%. The results also illustrate the absence of a Stark effect, as a red-shifted induced absorption peak does not exist.[20, 21]

Ideally, fluorescence and absorption (for the $1S_e$ state) of a charged NC should be 100% quenched and 50% bleached, respectively. However, the experimental results (fluorescence quenching followed by absorption bleaching measurements or vice versa on the same sample) show that the magnitude of the fluorescence quenching generally

falls short (within 20%) of the expected value compared to the bleach of the absorption. This may be attributed to our experimental conditions, where the higher excitation intensities and shorter wavelengths enhance the discharging rate during fluorescence quenching experiments, with the result that the number of charged NCs in our fluorescence quenching experiments may be slightly smaller than in the absorption bleaching studies.

In summary, we have fabricated simple, stable, solid-state devices that can reversibly charge multiple layers of NCs at room temperature. The drastic changes in the optical properties lead to the possibility of using NCs in optical modulators and in tunable fluorescent or photochromic displays. Further improvements, such as decreasing the NC layer thickness, the device size, and improving conduction through the nanocrystals by engineering the organic ligands, should shorten both charging and discharging times. Additionally these structures should also allow systematic studies of the photophysics of charged NCs.

References

1.   U. Meirav and E. B. Foxman, "Single-electron phenomena in semiconductors," Semiconductor Science and Technology **11**(3), 255-284 (1996).

2.   A. Franceshcetti and A. Zunger, "Optical transitions in charged CdSe quantum dots," Physical Review B **62**(24), 16287-16290 (2000).

3.   M. Shim and P. Guyot-Sionnest, "N-type colloidal semiconductor nanocrystals," Nature **407**(6807), 981-983 (2000).

4.   C. J. Wang, M. Shim, and P. Guyot-Sionnest, "Electrochromic nanocrystal quantum dots," Science **291**(5512), 2390-2392 (2001).

5.   D. I. Chepic, A. L. Efros, A. I. Ekimov, M. G. Vanov, V. A. Kharchenko, I. A. Kudriavtsev, and T. V. Yazeva, "Auger Ionization of Semiconductor Quantum Drops in a Glass Matrix," Journal of Luminescence **47**(3), 113-127 (1990).

6.   M. Nirmal, B. O. Dabbousi, M. G. Bawendi, J. J. Macklin, J. K. Trautman, T. D. Harris, and L. E. Brus, "Fluorescence intermittency in single cadmium selenide nanocrystals," Nature **383**(6603), 802-804 (1996).

7.   A. L. Efros and M. Rosen, "Random telegraph signal in the photoluminescence intensity of a single quantum dot," Physical Review Letters **78**(6), 1110-1113 (1997).

8.   S. Tarucha, D. G. Austing, T. Honda, R. J. vanderHage, and L. P. Kouwenhoven, "Shell filling and spin effects in a few electron quantum dot," Physical Review Letters **77**(17), 3613-3616 (1996).

9.   K. H. Schmidt, G. Medeiros-Ribeiro, and P. M. Petroff, "Photoluminescence of charged InAs self-assembled quantum dots," Physical Review B **58**(7), 3597-3600 (1998).

10.   R. J. Warburton, C. Schaflein, D. Haft, F. Bickel, A. Lorke, K. Karrai, J. M. Garcia, W. Schoenfeld, and P. M. Petroff, "Optical emission from a charge-tunable quantum ring," Nature **405**(6789), 926-929 (2000).

11.   G. Decher, "Fuzzy nanoassemblies: Toward layered polymeric multicomposites," Science **277**(5330), 1232-1237 (1997).

12.   M. F. Durstock, "Light emitting characteristics and dielectric properties of polyelectrolyte multilayer thin films," (Ph. D. Thesis, Massachusetts Institute of Technology, Cambridge, MA, 1999).

13.   S. S. Shiratori and M. F. Rubner, "pH-dependent thickness behavior of sequentially adsorbed layers of weak polyelectrolytes," Macromolecules **33**(11), 4213-4219 (2000).

14.   J. J. Harris, P. M. DeRose, and M. L. Bruening, "Synthesis of passivating, nylon-like coatings through cross-linking of ultrathin polyelectrolyte films," Journal of the American Chemical Society **121**(9), 1978-1979 (1999).

15.   C. B. Murray, D. J. Norris, and M. G. Bawendi, "Synthesis and characterization of nearly monodisperse CdE (E = S, Se, Te) semiconductor nanocrystallites," Journal of the American Chemical Society **115**(19), 8706-8715 (1993).

16.   M. A. Hines and P. Guyot-Sionnest, "Synthesis and characterization of stronly luminescing ZnS-Capped CdSe nanocrystals," Journal of Physical Chemistry **100**(2), 468-471 (1996).

17.   B. O. Dabbousi, J. RodriguezViejo, F. V. Mikulec, J. R. Heine, H. Mattoussi, R. Ober, K. F. Jensen, and M. G. Bawendi, "(CdSe)ZnS core-shell quantum dots: Synthesis and characterization of a size series of highly luminescent nanocrystallites," Journal of Physical Chemistry B **101**(46), 9463-9475 (1997).

18.   C. A. Leatherdale, C. R. Kagan, N. Y. Morgan, S. A. Empedocles, M. A. Kastner, and M. G. Bawendi, "Photoconductivity in CdSe quantum dot solids," Physical Review B **62**(4), 2669-2680 (2000).

19.   H. Mattoussi, L. H. Radzilowski, B. O. Dabbousi, E. L. Thomas, M. G. Bawendi, and M. F. Rubner, "Electroluminescence from heterostructures of poly(phenylene vinylene) and inorganic CdSe nanocrystals," Journal of Applied Physics **83**(12), 7965-7974 (1998).

20.   V. L. Colvin, K. L. Cunningham, and A. P. Alivisatos, "Electric-Field Modulation Studies of Optical-Absorption in Cdse Nanocrystals - Dipolar Character of the Excited-State," Journal of Chemical Physics **101**(8), 7122-7138 (1994).

21.   A. Sacra, D. J. Norris, C. B. Murray, and M. G. Bawendi, "Stark Spectroscopy of Cdse Nanocrystallites - the Significance of Transition Linewidths," Journal of Chemical Physics **103**(13), 5236-5245 (1995).

Curriculum Vitae
Mirna Jarosz

Education

Massachusetts Institute of Technology   Cambridge, MA
Ph.D. Candidate. Department of Chemistry, expected degree date June 2004. Thesis work: The physics and chemistry of transport in CdSe quantum dot solids. **GPA 4.7/5.0**

University of Washington   Seattle, WA
B.S. Department of Chemistry, Summa Cum Laude with Departmental Distinction, June 1999. Senior Thesis: Calculations on the origin of hyperporphyrin spectra in sequentially protonated meso-(dimethylaminophenyl) porphyrins. **GPA 3.98/4.0**

University of Washington   Seattle, WA
Transition School and Early Entrance Program, 1994-1995.

Awards

2002-04 Lester Wolf Fellow
2001-02 Corning Fellow
1999   Graduated UW Summa Cum Laude and with Departmental Distinction
1999   UW Outstanding Graduate in Chemistry
1999   Phi Beta Kappa
1998   UW Outstanding Student in Organic Chemistry (Hyp Dauben Award)
1998   UW Outstanding Student in Physical Chemistry
1998   UW Undergraduate Scholars Award
1997-99 Goldwater Scholarship
1996   Outstanding Student in General Chemistry (CRC Award)
1995-97 NASA Undergraduate Scholarship
1994-95 Participant in University of Washington's Transition School & Early Entrance Program

Research Experience

MIT, Department of Chemistry   Cambridge, MA
Advisor: Moungi Bawendi
"The physics and chemistry of transport in CdSe quantum dot solids"   1999-2004

University of Washington, Department of Chemistry   Seattle, WA
Advisor: Martin Gouterman
"Calculations on the origin of hyperporphyrin spectra in sequentially protonated meso-(dimethylaminophenyl) porphyrins"   1999-1999
"Pressure-sensitive paint for aeronautics"   1996-1999

University of Washington, Department of Pulmonary & Critical Care   Seattle, WA
NASA undergraduate research program
"Asthma responses in mice"   1995-1996

Teaching Experience

MIT, Department of Chemistry   Cambridge, MA
Thermodynamics and Kinetics. Teaching Assistant, Spring 2000.
General Chemistry. Teaching Assistant, Fall 1999.

UW, Department of Chemistry   Seattle, WA

Honors General Chemistry. Teaching Assistant, Fall 1998.
Quantum Mechanics. Assistant grader, Spring 1998.

<div align="center">Oral Presentations</div>

Vitasovic, M; Stott, NE; Kastner, MA; Bawendi, MG, *Transport properties of films of high-quality semiconductor nanocrystals*, Proceedings of the American Chemical Society, Boston, 2002.

Vitasovic, M; Drndic, M; Leatherdale, CA; Morgan, NY; Bawendi, MG; Kastner, MA, *Charge transport through thin films of CdSe nanocrystals*, Proceedings of the American Physical Society, Seattle, 2001.

Woo, W-K; Shimizu, K; **Vitasovic, M**; Bawendi, M; Rubner, M; Neuhauser, R; Leatherdale, C, *Photophysics of charged CdSe quantum dots,* Proceedings of the American Physical Society, Seattle, 2001.

<div align="center">Publications</div>

Jarosz, MV; Porter, VJ; Fisher BR; Kastner, MA; Bawendi, MG, *Photoconductivity studies of treated CdSe quantum dot films exhibiting increased exciton ionization efficiency*, (submitted 2004).

Jarosz, MV; Stott, NE; Drndic, M; Morgan, NY; Kastner, MA; Bawendi, MG, *Observation of bimolecular carrier recombination dynamics in close-packed films of colloidal CdSe nanocrystals*, J Phys Chem B, 107(46) 12585-12588 (2003).

Drndic, M; Markov, R; **Jarosz, MV**; Bawendi, MG; Kastner, MA; Markovic, N; Tinkham, M, *Imaging the charge transport in arrays of CdSe nanocrystals*, Applied Physics Letters, **83**(19), 4008-4010 (2003).

Novikov, DS; Drndic, M; Levtiov, LS; Kastner, MA; **Jarosz, MV**; Bawendi, MG, *Anomalous transport in quantum dot arrays*, (submitted 2003).

Drndic, M; **Jarosz, MV**; Morgan, NY; Kastner, MA; Bawendi, MG, *Transport properties of annealed CdSe colloidal nanocrystal solids*, J Appl Phys, 92(12), 7498-7503 (2002).

Morgan, NY; Leatherdale, CA; Drndic, M; **Jarosz, MV**; Kastner, MA; Bawendi, MG, *Electronic transport in colloidal CdSe nanocrystals*, Phys Rev B, 66(7), 075339 (2002).

Woo, WK; Shimizu, KT; **Jarosz, MV**; Neuhauser, RG; Leatherdale, CA; Rubner, MA; Bawendi, MG, *Reversible charging of CdSe nanocrystals in a simple solid-state device*, Adv Mat, 14(15), 1068-1071 (2002).

Vitasovic, M; Gouterman, M; Linschitz, H, *Calculations on the origin of hyperporphyrin spectra in sequentially protonated meso-(dimethylaminophenyl) porphyrins*, Journal of Porphyrins and Phthalocyanines, 5(3), 191-197 (2001).

Acknowledgements

This thesis would not have been possible without the extensive and generous support that I have received both personally and scientifically. From the personal side, I must first thank my husband, Daniel, for always being there for me (if only over the phone from Seattle for most of my first two years), for encouraging me when science was going great, for reminding me to be realistic when I swore nothing would ever work again, and for making the times outside of lab happier than I ever could have hoped.

Thanks as well to my parents: to my father for teaching me the difference between physics, chemistry, and biology when I was very young ("if it breaks, it's physics; if it stinks, it's chemistry; and if it wiggles, it's biology") and for enthusiastically encouraging me in my scientific endeavors; to my mother for being supportive no matter what I decided to do, and for always perceiving when I could use her help.

I also know that I am here at MIT thanks in great part to the amazing support of my undergraduate advisor at the University of Washington, Prof. Martin Gouterman. Martin always showed more faith in me than I had in myself, and went out of his way to create projects for me that encouraged my scientific interests. It was Martin that first introduced me to Moungi by setting up a visit to MIT when I happened to be in Boston on vacation during my junior year. I am also grateful for all of the support I have received from Prof. James Callis, who introduced me to Martin and who was one of the professors that taught the honors general chemistry course that first got me excited about chemistry.

Of course I am very thankful to my thesis advisor, Prof. Moungi Bawendi, for teaching me how to conduct responsible scientific research, for allowing me scientific independence while still being available whenever I got stuck, for patiently helping me to mature scientifically, and for pushing me to find the answers when I was sure it wasn't possible. I was always impressed that I could walk into your office utterly confused, but then walk out of it full of new ideas and excitement.

Much of my work has been a collaborative effort with Prof. Marc Kastner in physics. Marc was an invaluable source of help in solidifying my ideas of the physics of CdSe QD transport into a convincing and mathematically and physically sound picture. Thank you also to the post-docs (Marija and Laurie), graduate students (Nicole and Fumi), and UROP (Maria) that participated in the collaboration. Thanks especially for making all of our devices.

Because my work was such a multidisciplinary project, the extensive user facilities at MIT were an essential resource. Thank you to the staff of CMSE and MTL for all of your assistance.

And now for the long list of thanks to my colleagues in the Bawendi lab, starting with former members. Catherine – thank you for patiently teaching me the art of QD solids and photoconductivity measurements. Wing – thank you for letting me participate in the QD charging project, and for passing on to me some of your endless knowledge of QD chemistry (as well as some of your stashes of TOP and TOPO). You also taught me the importance of stowing away supplies and chemicals that you know work, because you never know when what you can buy will stop working or will be made temporarily unavailable. Vikram – thank you for always keeping me on my toes, and never letting me forget how old I am. I was always impressed with your dedication to science. Hans –